Progress in Materials Science 89 (2017) 479–521

Contents lists available at ScienceDirect

Progress in Materials Science

journal homepage: www.elsevier.com/locate/pmatsci

Electrochemomechanical degradation of high-capacity battery electrode materials

Sulin Zhang [a,*], Kejie Zhao [b], Ting Zhu [c], Ju Li [d,*]

[a] Department of Engineering Science and Mechanics, Pennsylvania State University, University Park, PA 16802, USA
[b] School of Mechanical Engineering, Purdue University, West Lafayette, IN 47907, USA
[c] Woodruff School of Mechanical Engineering, Georgia Institute of Technology, Atlanta, GA 30332, USA
[d] Department of Nuclear Science and Engineering and Department of Materials Science and Engineering, Massachusetts Institute of Technology, Cambridge, MA 02139, USA

ARTICLE INFO

Article history:
Received 11 June 2016
Received in revised form 18 April 2017
Accepted 25 April 2017
Available online 29 April 2017

Keywords:
Lithium ion and sodium ion battery
High-capacity electrodes
Electrochemomechanical degradation
In-situ transmission electron microscopy
Multiscale modeling
Electrochemistry-mechanics coupling

ABSTRACT

Enormous efforts have been undertaken to develop rechargeable batteries with new electrode materials that not only have superior energy and power densities, but also are resistant to electrochemomechanical degradation despite huge volume changes. This review surveys recent progress in the experimental and modeling studies on the electrochemomechanical phenomena in high-capacity electrode materials for lithium-ion batteries. We highlight the integration of electrochemical and mechanical characterizations, *in-situ* transmission electron microscopy, multiscale modeling, and other techniques in understanding the strong mechanics-electrochemistry coupling during charge-discharge cycling. While anode materials for lithium ion batteries (LIBs) are the primary focus of this review, high-capacity electrode materials for sodium ion batteries (NIBs) are also briefly reviewed for comparison. Following the mechanistic studies, design strategies including nanostructuring, nanoporosity, surface coating, and compositing for mitigation of the electrochemomechanical degradation and promotion of self-healing of high-capacity electrodes are discussed.

Contents

---

* Corresponding authors at: Department of Engineering Science and Mechanics, Pennsylvania State University, University Park, PA 16802, USA (S. Zhang); Department of Nuclear Science and Engineering and Department of Materials Science and Engineering, Massachusetts Institute of Technology, Cambridge, MA 02139, USA (J. Li).

E-mail addresses: suz10@psu.edu (S. Zhang), liju@mit.edu (J. Li).

http://dx.doi.org/10.1016/j.pmatsci.2017.04.014

---

1. Introduction

Rechargeable lithium-ion batteries (LIBs) have served as the primary power source for a variety of portable electronics in today's mobile society, including smart phones, laptop computers, and wearable electronics, as well as in power tools, electric vehicles and grid-scale storage [1–11]. However, the current LIB technology still cannot meet the rapidly growing demand for high energy density and long cycle life. In particular, the volumetric energy density of the current LIB cells severely limits miniaturization of electronics as well as the driving distance of electric vehicles. These have motivated relentless search for new electrode materials with higher gravimetric and volumetric specific capacities [12–17]. However, capacity and cyclability appear to be two conflicting properties since improving one often compromises the other. In particular, high-capacity electrodes are prone to chemomechanical failure upon electrochemical charge-discharge cycling, leading to

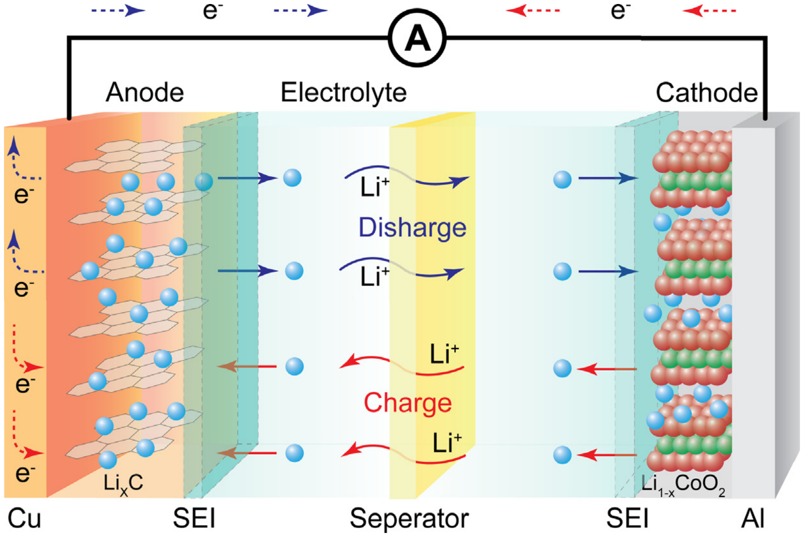

Fig. 1. Schematic of a LIB cell comprised of a negative electrode (graphite) and a positive electrode ($LiCoO_2$), separated by a liquid electrolyte. Li ions migrate from the positive (negative) electrode to the negative (positive) electrode through the electrolyte during charging (discharging); meanwhile electrons migrate through an external circuit to maintain charge neutrality. Current collectors (here are Al and Cu) are used to transport electrons to and from the electrodes.

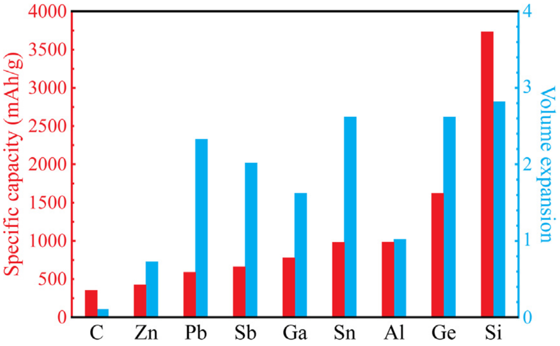

Fig. 2. Specific capacities of potential anode materials for LIBs (red) and their corresponding volumetric expansion upon lithiation (blue).

fast capacity decay of the battery cells [18–21]. Hence, a fundamental understanding of the chemomechanical degradation mechanisms of the high-capacity electrode materials is imperative to the development of effective mitigation strategies toward high-performance rechargeable batteries.

A battery is an energy storage device that converts electrical energy to chemical energy, and vice versa [11]. It functions by shuttling ions between two electrodes during charge-discharge cycles, as schematically shown in Fig. 1. An electrolyte, which conducts ions but not electrons, separates the two electrodes. When a LIB is being charged, electrons are pumped out of the cathode particles (via polaron conduction inside), through conductive agents like carbon black, current collector and the outer circuit, and injected into the anode particles. The electrochemical potential difference of Li ions (Li^+) in the two electrodes then drives Li^+ migrating from the cathode (positive electrode) to the anode (negative electrode) through the electrolyte, so bulk charge neutrality is approximately maintained inside the cathode and anode particles, which are henceforth called the cathode-active (ca) and anode-active (aa) contents. Upon discharging, the reverse occurs, and the chemical energy stored in the electrodes (chemical potential difference of polarons/ion pairs or neutral “Li atoms” in aa and ca particles) is converted into electrical energy to power the external working load. A sodium ion battery (NIB) works by the same principle as the LIB, wherein Na ions shuttle between the electrodes and free electrons flow through the outer circuit. The dramatic contrast in transport transference number (the ratio between electron conductance and Li^+ conductance) between the two interpenetrating networks, comprised of the open pore network infilled by electrolyte, along with the metal wiring of outer circuit, current collectors made of Cu and Al, and carbon black network, is a key feature of the battery device. The percolating transportation of electrons/ions outside ca/aa particles is characterized by the Ohmic resistance, R_{Ohm}, while the transport of polarons/ions (or neutral atoms) inside ca/aa particles by the Warburg impedance R_{W}. The charge-transfer resistance, R_{ct}, characterizes the difficulty of a solvated Li^+ ion in the electrolyte in breaking its solvation shell, simultaneously capturing an electron from the conductive agent, and then getting inserted into ca/aa particles as polarons/ions (or neutral atoms). Any disruption or degradation of the transport/reaction characteristics R_{Ohm}, R_{W}, or R_{ct} would cause the battery cell to degrade, in addition to the intrinsic capacity decay of ca/aa particles due to loss/gain of chemical elements and phase transformations that is more thermodynamic in origin, as reflected by the open-circuit voltage versus the state-of-charge (SOC) curve.

In commercial LIBs graphite is currently the most commonly used anode material. Lithium incorporates into graphite by an intercalation mechanism, wherein Li ions are reversibly inserted into and extracted from the interlayer space of graphite during charge-discharge cycles. The intercalation mechanism induces relatively small volume expansion, hence ensures capacity retention, stable working voltage, and long cycle life [19]. However, limited by the sites available, the intercalation mechanism provides relatively low specific capacity. For graphite, the chemical compound LiC_6 formed upon Li intercalation limits its theoretical capacity to 372 mAh g^{-1} [1,21]. Compared to graphite, a variety of anode candidates, such as Si, Sn, Ge, Al, react with Li by alloying, a process that involves extensive bond breaking/forming and defect evolution, change of crystal structure, or even solid-state amorphization. Since alloying is not limited by the available host sites it can render a much higher theoretical specific capacity (Fig. 2). For example, when alloyed to $Li_{22}Si_5$, Si, the leading candidate for anode materials for LIBs, gives a theoretical specific capacity of 4200 mA h g^{-1} based on aa weight before lithiation (if based on post-lithiation aa weight, it is 2012 mAh g^{-1}) [19–22], which is one order of magnitude higher than that of graphite. Conversion represents a third lithiation mechanism in which the electrode materials undergo conversion reaction to form lithium oxide. Conversion anodes generally offer high specific and volumetric capacities [23–25]. Similar to alloying, conversion also generates large volumetric strain, causing pulverization of the electrode particles and unstable SEI growth, in addition to large voltage hysteresis [26].

In 2005, Sony introduced Nexelion™ family of LIB cells that use Sn-Co nanoparticles composited in graphite anode, which increased the anode’s volumetric capacity by as much as 30% but with some loss in voltage. In recent years, Si-containing high-capacity anodes appeared more and more on the market, and this trend is currently expected to become mainstream. To assess how much cell performance enhancement could be derived from the insertion of high-capacity electrodes, it is useful to first review the baseline construction of a standard $LiCoO_2$/graphite cell. The $LiCoO_2$ cathode is typically mixed with a small amount of binder and carbon black, and slurry-coated on aluminum foil ($\leq$20 μm thickness). The thickness of the dried cathode paste is typically $\leq$100 μm in order to obtain reasonable rate performance, with ~20 vol% porosity (the crystal density of $LiCoO_2$ is 5.06 g/cm^3, but the active $LiCoO_2$ compaction density ends up ~4.1 g/cm^3). The thickness of the graphite anode is approximately the same as the $LiCoO_2$ cathode (a coincidence), with ~30 vol% porosity allowed for electrolyte infiltration (the crystal density of graphite is 2.266 g/cm^3, but the compacted density ~1.6 g/cm^3). The anode paste is slurry-coated on copper foil ($\leq$10 μm thickness). During battery cycling, volume change takes place in both the cathode and anode pastes. The graphite anode will expand in thickness by as much as ~30%. To prevent short-circuiting due to morphological instabilities, an electronically insulating separator (~7 to 25 μm thick) is placed in between the $LiCoO_2$ and graphite [27] electrodes. This separator has good thermomechanical stabilities to strictly prevent electronic conduction, but has ~30 nm diameter nanopores infiltrated by electrolyte that allows Li^+ ion conduction. Thus, back-of-the-envelope calculation indicates that an Al|$LiCoO_2$|separtor|graphite|Cu stack of ~250 μm thick would give a matching anode-cathode areal capacity of ~5 mA h/cm^2 (4.1 g/cm^3 × 140 mA h g^{-1} × 90 μm = 5.17 mA h/cm^2 on $LiCO_2$ cathode, and 1.6 g/cm^3 × 360 mA h g^{-1} × 90 μm = 5.18 mA h/cm^2 on graphite anode), after taking into account losses from separator overhang and electrical leads, the initial formation (loss of cycleable Lithium due to Coulombic inefficiency problem, to be explained later) and volume expansion, and the subsequent more gradual capacity decay with cycling. Since the average discharge voltage of the $LiCoO_2$/graphite cell is 3.8 − 0.1 = 3.7 V, this would give 3.7 V × 5 mA h/cm^2/0.025 cm = 740 W h/L cell energy density, which is essentially the present limit for standard $LiCoO_2$/graphite cells, after 25 years of heavy industrial optimization.

The battery cell-average mass density can be measured by Archimedes method, and is ~2.7 g/cm^3, considering that the cell contains a mix of electrolyte (1 M $LiPF_6$ in EC/DEC solvent has density 1.26 g/cm^3), $LiCoO_2$ (5.06 g/cm^3), graphite (2.266 g/cm^3), aluminum (2.7 g/cm^3), copper (8.96 g/cm^3), polypropylene (PP) separator (0.946 g/cm^3), etc. So the present limit to cell's gravimetric energy density is approximately 740 W h/L/2.7 g/cm^3 ~ 270 W h/kg. In order to bring LIB cell energy density up to beyond 1000 W h/L and/or 400 W h/kg, significant enhancement in the electrode materials' capacity is needed, which motivates the current review. In addition, from back-of-the-envelope calculations above, one appreciates that a cell is a *system* and it is essential to keep the system balanced. For example, the areal capacity of the anode needs to match with the areal capacity of the cathode, otherwise there will be wasted capacity on either side that takes up dead volume/mass, unless the highest state of charge is intentionally throttled to improve life or safety. Such balance needs to be maintained from the beginning of use to the last cycle (industrially, cell life is often defined by the energy release in discharge decaying to 80% of the value at the beginning of use). Further, the electrolyte should not dry out, its chemistry

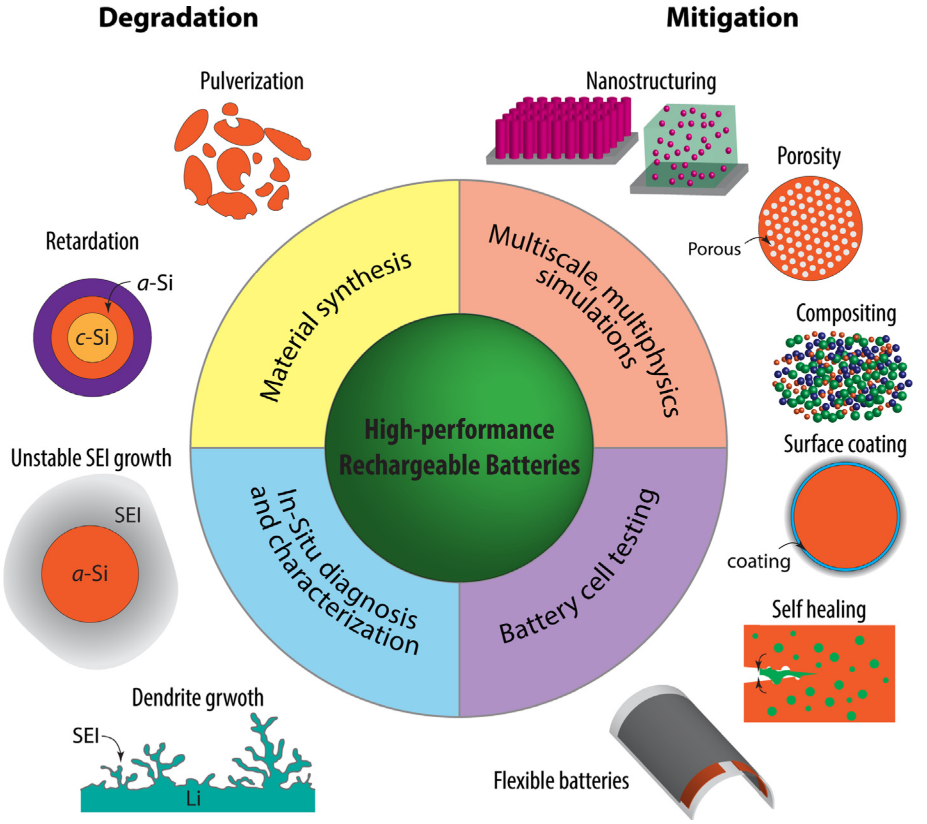

Fig. 3. Advanced characterization techniques, degradation mechanisms, and mitigating strategies of high-volume-change anode materials.

(e.g. Li^+ and anion concentration, and harmful substances like HF, H_2O and transition metal cations) should not be altered significantly, the open pores in cathode/anode pastes and separators should not close, and the electron-conduction paths should not collapse, etc., while the cathode/anode active contents sustain large volume change, stress evolution, complex surface reactions, and internal structural transformations. For example, Si-containing high-capacity anode paste can often sustain more than 100% increase in thickness with continued cycling. Such a large change, implying many moving parts in the system, poses a huge challenge to materials researchers and mechanical engineers, modelers, and inventors alike.

Inherent to the high-capacity electrodes is the huge volume changes induced by Li insertion (Fig. 2) and extraction [18,28–35], causing (a) chemomechanical degradation of the electrode materials themselves, such as loss of elements, phase change, dislocation accumulation, fatigue and fracture, and consequently the delamination of the active materials from the binders and current collectors [36]; (b) depletion of the solvent of the liquid electrolyte, or exhaustion of cycleable Li inventory in the system (anode + cathode + salt) due to increased surface area and reactivity of the surface with the electrolyte; (c) disruption of electron/ion conduction paths (carbon black/pore networks), resulting in loss of electronic/ionic percolation, and consequently limiting the cycle life of the battery cells. It has been widely observed that chemomechanical degradation of electrode materials is associated with strong electrochemistry-mechanics coupling across different length and time scales. On one hand, Li insertion and extraction induce large volume changes in the electrode materials, modulating stress generation, defect nucleation and growth, and fracture of the electrodes; on the other hand, the mechanical stress modifies the chemical potentials of Li, and accordingly regulates the kinetics of lithiation and delithiation. This chemomechanical coupling is particularly significant for high-capacity electrode materials as a large amount of Li ions are inserted into and extracted from the electrodes during charge-discharge cycles.

Several degradation mechanisms in the large-volume-change electrode materials have been observed, as illustrated in Fig. 3. First, lithiation induced large volumetric expansion tends to generate high stresses, which may cause fracture and pulverization of the electrode particles, and consequently the loss of electrical contact of the battery components and rapid capacity fading. Second, lithiation induces large compressive stress inside the active materials, which may slow down further lithiation, causing lithiation retardation and compromising rate performance. In severe cases, the compressive stress may be high enough to completely arrest lithiation, and the inner core of the active materials becomes electrochemically inaccessible, rendering a reduced effective capacity. Third, the large volume increase during charging causes breakage of the solid-electrolyte interphase (SEI) layer on the surface of the electrodes, which consequently exposes new electron-conductive surfaces to liquid electrolytes. Commonly used organic carbonates electrolyte with $LiPF_6$ salt decompose at voltages below 1.3 V or above 4.5 V versus Li^+/Li [4], meaning the electrolyte solvent/salt would reductively/oxidatively decompose near any conductive surface that can donate/accept electrons. Since a lot of the high-capacity electrode materials work at voltages beyond the said stability window of the electrolyte, irreversible reaction of the electrolyte with the exposed surfaces forms new SEIs and converts cycleable Li into inactive Li in SEIs. This process repeats over cycles and the batteries eventually die of Li exhaustion [37]. Dendrite growth represents another important degradation mechanism in LIBs [38,39]. However, this mechanism is not specific to large-volume-change electrode materials, and will not be reviewed here.

To understand the degradation processes of the high-capacity electrode materials, various novel experimental techniques have been developed to characterize microstructural evolutions during battery cycling. Theory and modeling are then used to relate them to electrochemical performance from battery cell testing, and to guide advanced material synthesis (see Fig. 3). Of particular note is the nanobattery testing platform [18] that enables powerful in-situ transmission electron microcopy (TEM) imaging of electrochemical cycling using individual nanowires or nanoparticles as the working electrodes. With this platform, a variety of high-performance anode (Si [33,34,40–44], Ge [34,45–47], Ga [49], graphene [50], multi-walled carbon nanotube [48]) and cathodes (e.g., $LiFePO_4$ [51,52]) materials have been investigated, with liquid [18] or solid electrolytes (e.g., [43]), and with microstructures [53] and surface modifications [54,55]. A wide range of novel phenomena have been discovered, spanning from ion and electron transport, electrochemical reaction, microstructural evolution, to mechanical degradation that are critical for understanding the electrochemical performance of nanostructured battery materials. This advance opens a bottom-up avenue for developing next-generation high-performance LIBs, in contrast to the top-down approach adopted by the conventional battery development. Parallel to the experimental studies, theoretical and computational models across different length scales have been developed to elucidate the underlying degradation mechanisms of the electrode materials. The integrated experimental and theoretical approach formulates a unique framework for battery characterization, diagnosis, and optimization.

This review summarizes recent progresses in the fundamental understanding of the electro-chemomechanical degradation of high-capacity electrode materials, covering both experimental and modeling aspects (Fig. 3). A series of in-situ TEM videos are included to highlight the dynamic electrochemical processes of a variety of anode materials. We begin by introducing more rational measures of capacities and coulombic efficiency, along with a brief description of the unique experimental and modeling tools developed for characterizing the high-capacity electrode materials. Novel experimental phenomena from the electrochemical lithiation and delithiation of a variety of important anode materials, along with the insights from model predictions, are then presented. Strategies for mitigating the chemomechanical degradations, including porosity, surface coating, compositing, etc. (Fig. 3), are then followed presented. Degradation of Na-ion batteries will also be briefly discussed for a comparative purpose. Finally, we draw conclusions and provide perspectives on this topic.

2. Methodologies

2.1. Practical measure of capacities

We evaluate a commercial battery cell (cylindrical, pouch, prismatic, etc.) by a large number of metrics, such as voltage characteristics, volumetric and gravimetric cell energy densities, charging and discharging rates, cycle life, low-temperature and high-temperature limits, and probably most importantly, safety characteristics, including in abuse situations. In view of the fact that a battery cell is a complex, dynamical system composed of many material components (active electrode particles, electrolyte, binder, conductive networks), a common practice in evaluating cell performance is often to first measure/compute individual materials properties. However, there are pitfalls in the literature and research practices in overemphasizing a subset of materials properties. For example, the specific gravimetric capacity/power of the active material *alone*, in unit of mA h g^{-1}(active), where g(active) is the weight of the active electrode materials only, in grams, measured from so-called half-cell tests. In a half cell, there are superabundant electrolyte, superabundant Li-containing counter-electrode material, superabundant electrocatalytic surfaces and conductive networks, etc., relative to the active material being tested. Yet in a real commercial cell or a prototype cell intended for commercial use (the so-called "full cell"), the opposite electrodes must be tightly matched in capacity. In addition, an extreme paucity of the "auxiliary" materials is often used, so the limiting component may be the "auxiliary" materials instead of the active material being tested. Consider a certain anode material that has seemingly great mA h g^{-1}(active) and cycle life in half-cell tests, but fragments constantly during cycling. The fragmentation creates new surface areas and actively consumes electrolyte (forming SEI, for instance). The anode material may prolifically catalyze the gassing decomposition of the electrolyte. Under these conditions, the cycle life of a full cell would then be severely limited by the drying out of the "auxiliary" material – the liquid electrolyte – that however is not reflected in the half-cell tests, projecting an over-optimistic impression.

To address this issue, we here define a new metric for evaluating the practical performance of high-capacity anodes. We define the mass of the anode active content to be g(aa) and mass of the cathode active content to be g(ca). In a full cell, the total mass is g(aa) + g(ca) + g(auxiliary), where g(auxiliary) sums the weights of the electrolyte, current collectors, separator, and binders/conductive agents on both sides. Since mA h(aa) = mAh(ca) in a full cell, we define

$$\mathrm{MG(aa)} \equiv \frac{\mathrm{mAh(aa)}}{\mathrm{g(aa)} + \mathrm{g(auxiliary)}/2} \tag{1}$$

as the performance metric to optimize, rather than optimizing

$$\mathrm{mAhg(aa)} \equiv \frac{\mathrm{mAh(aa)}}{\mathrm{g(aa)}}, \tag{2}$$

which is the usual practice. Similarly, one shall use

$$\mathrm{MG(ca)} \equiv \frac{\mathrm{mAh(ca)}}{\mathrm{g(ca)} + \mathrm{g(auxiliary)}/2}, \tag{3}$$

instead of

$$\mathrm{mAhg(ca)} \equiv \frac{\mathrm{mAh(ca)}}{\mathrm{g(ca)}} \tag{4}$$

for cathode active content. The full-cell gravimetric performance is

$$\mathrm{MGf} \equiv \frac{1}{\frac{1}{\mathrm{MG(aa)}} + \frac{1}{\mathrm{MG(ca)}}}. \tag{5}$$

For example, the full-cell gravimetric energy density is expected to be

$$[\text{Average Voltage(ca)} - \text{Average Voltage(aa)}] \times \mathrm{MGf}. \tag{6}$$

Acknowledging "auxiliary" weight is crucial for avoiding pathologies in both the evaluation and future development of high-capacity electrode materials. For example, excessive fragmentation of cathode may not show up as an issue in half-cell tests if cathode ultra-nanoparticles are adsorbed on superabundant amount of graphene substrates, as they would never lose electrical contact. But such might be impossible in commercial cells. If mAhg(ca) is used as the performance metric, then one would be tempted to use as low amount of cathode and as much graphene as possible, to maximize the numerator in (4). But if the MG(ca) number needs to be published – even if a crude one - one may find that the previous strategy leads to a ridiculously small value due to the huge denominator, and therefore is nearly meaningless for full cells.

Unfortunately, too many mAhg(aa) (for Si, Sn, Ge, etc.) and mAhg(ca) (for Sulfur, etc.) data have been published, and most papers did not present enough information for precise estimation of MG. This review must therefore still use mAhg metric for most of its presentations. To compensate for this deficiency, an open-source web script calculator is provided for mAhg → MG conversion at http://alum.mit.edu/www/liju99/bc. For future results, the user can measure and fill in the more precise values for porosities, binder and carbon black weights used, etc. For given amount of anode, we will by default assume $LiCoO_2$ to be the counter electrode in computing g(auxiliary). For cathode, by default we will assume graphite to be the counter electrode in computing g(auxiliary), with porosity and separator parameter values provided in the Introduction of this review. We expect that this open-source calculator with default estimates can provide a rudimentary standard for materials researchers (who may not be familiar with commercial cell construction) to guide assessment and development of high-capacity electrodes.

Note that most of the half-cell tests use metallic Lithium as the counter electrode, which actually continuously consumes liquid electrolyte on its own, even if the anode material itself does not. So in our web calculator, instead of using the actual experimental half-cell g(electrolyte), we use a hypothetical g(electrolyte) assuming a "perfect" counter-electrode (e.g. $LiCoO_2$) which does not consume much liquid electrolyte, in computing g(auxiliary) for (1) and (3). In other words, we try to build a "*Gedanken* full cell" based on the cathode/anode half-cell test data, to define the MG standard.

In a similar vein, it is worth mentioning that nanomaterials are not always the answer for improving full-cell energy density. Indeed, for cathodes it has long been appreciated that single crystal grains of few microns in size could be the optimum for volumetric energy density, due to the higher tap density and lower surface area. From the point of view of improving the rate performance and half-cell cycle life, nanostructuring is generally beneficial because the solid-state diffusion distance is reduced, and nanomaterials generally have better strain-tolerance ("smaller is stronger" [56]) due to the altered defect nucleation/propagation and population dynamics. However, if there is greater exposed surface area from open pores, nanoparticles can have severe drawbacks (as will be discussed later in detail, when Coulombic inefficiency is introduced) on the full-cell cycle life, as the balance with the counter electrode and electrolyte can be more easily broken, like the proverbial "bad partner". For anode nanomaterials, often the $LiCoO_2$ partner or the electrolyte first gets depleted in full-cell cycling.

Currently, most nanomaterials have low nominal density (the as-synthesized nanopowders have tap density typically < 0.5 g/cm^3). So even if the gravimetric specific capacity is impressive (for example ~1000 mA h g^{-1}), the volumetric capacity may be much less impressive. For high-capacity anode materials the competition is graphite (360 mA h g^{-1}), whose electrode density is 1.6 g/cm^3. If the anode paste has anode nanomaterials density 0.4 g/cm^3, even with 1400 mA h g^{-1} capacity it will still have worse volumetric specific capacity than graphite. This will most likely exclude this material from being used in phones, laptops, or automotive batteries.

Given above, another critique of the present battery nanomaterials literature is that these packing densities and electrode thicknesses are often not reported. In order to assess whether a reported material might be useful for commercial use, it is essential for researchers to report the tap density and compressed density (or the thickness before and after calendaring, and also after battery cycling) of the nanomaterial electrode. Similar to (1)-(6), we can define

$$\mathrm{MV(aa)} \equiv \frac{\mathrm{mAh(aa)}}{\mathrm{cm^3(aa)} + \mathrm{cm^3(auxiliary)}/2} \tag{7}$$

to track the volume of the anode-active particles and auxiliary contents, where cm^3(auxiliary) includes the volumes of the liquid electrolyte, SEI, current collectors, separator, and binders/conductive agents on both sides, as well as possible void/gas bubble spaces that could be present from the beginning or generated during cycling. Similarly, we can define

$$\mathrm{MV(ca)} \equiv \frac{\mathrm{mAh(ca)}}{\mathrm{cm^3(ca)} + \mathrm{cm^3(auxiliary)}/2} \tag{8}$$

for the cathode. The full-cell volumetric performance is then

$$\mathrm{MVf} \equiv \frac{1}{\frac{1}{\mathrm{MV(aa)}} + \frac{1}{\mathrm{MV(ca)}}}, \tag{9}$$

considering the anode, electrolyte, and cathode operate in series. For example, the full-cell volumetric energy density is expected to be

$$[\mathrm{Average\ Voltage(ca)} - \mathrm{Average\ Voltage(aa)}] \times \mathrm{MVf}. \tag{10}$$

2.2. Electrochemical characterizations

Electrochemical testing techniques, including half-cell cycling, capacity-matched full-cell cycling, cyclic voltammetry (CV), electrochemical impedance spectroscopy (EIS), galvanostatic intermittent titration technique (GITT), etc., are commonly used to characterize high-capacity anode materials. It is critically important to provide physical interpretations of these testing results for mechanistic studies.

In half-cell cycling, the active material to be tested is paired against a superabundant source of cycleable Li, usually Li metal chips, with a thickness on the order of 100–400 μm. Solid lithium metal has volumetric capacity of 2060 mA h/cm^3 (3884 mA h g^{-1} × 0.53 g/cm^3). Therefore, to provide 1 mAh/cm^2 areal capacity, only ~5μm thick of fully dense Li metal is needed, in contrast to ~20 μm thick of $LiCO_2$ paste or graphite paste in battery industry. Typical active material used in half-cell tests has a loading of ~2 mg/cm^2. Take an anode with capacity ~1000 mAhg^{-1}, the areal capacity required for first-cycle lithiation (assuming the anode comes with no cycleable Lithium) is 1000 mAh g^{-1} × 2 mg/cm^2 = 2 mAh/cm^2. Thus a 10 μm thick solid lithium metal would be sufficient for the first-cycle lithiation of the anode (2 $\mathrm{mAh/cm^2}$), and a Li metal chip with thickness 400 μm would be 40× in excess.

Lithium metal is electronically conductive and typically has low polarization (the charge-transfer resistance R_{ct}) despite SEI formation on its surface. For this reason, lithium metal has been widely used as the counter-electrode as it supports quite accurate absolute voltage report of the working electrode in 2-terminal tests. However, lithium metal has a mossy growth problem when lithium is deposited back from anode (as anode is being delithiated). Based on electron microscopy and optical microscopy observations, lithium metal electrodes undergo surface morphology instability and surface area proliferation when lithium is deposited back, with at least three modes: root-grown lithium whisker, root- and tip-grown mossy lithium, and tip-grown dendrite, depending on the local conditions [57]. The morphological changes do not affect half-cell test results for anode/cathode, as long as there are plenty of electrolyte and lithium metal left in the half-cell. However, when soluble redox mediators (SRM) from the reductive decomposition of the liquid electrolyte come into play, it would affect the rigorous interpretation of the Coulombic Efficiency (CE).

As explained in Section 1, an ideal battery works based on the assumption that the electrolyte does not transport free electrons. But if a liquid electrolyte can solvate both SRM and SRM^{m+}, where SRM and SRM^{m+} are two redox charge states of a soluble molecule, the following "shuttling" may occur: SRM can be oxidized ($\mathrm{SRM} \rightarrow \mathrm{SRM}^{m+}$) when contacting the cathode; then because SRM^{m+} is soluble in the liquid electrolyte, SRM^{m+} may diffuse to the anode, where it gets reduced ($\mathrm{SRM}^{m+} \rightarrow \mathrm{SRM}$); since SRM is also soluble, SRM may diffuse back to the cathode surface and repeat the process. This way, "free electron" is effectively leaked through the liquid electrolyte from the anode to the cathode. A well-known example of $\mathrm{SRM/SRM}^{m+}$ would be $\mathrm{Fe^{2+}/Fe^{3+}}$ in aqueous medium, since both the ferrous and ferric forms of Fe cation are soluble. Note that $\mathrm{SRM/SRM}^{m+}$ do not have to be consumed in the shuttling: they can just form an equal and opposite flux in the electrolyte at steady state. Such SRM shuttling has been revealed in multiple battery contexts, and they are even designed as artificial additives to achieve certain voltage-shunting characteristics [58,59].

We have previously mentioned that the working voltages of many anode materials (Si, Sn, Ge, Al, and Li, etc.) fall below the electrochemical stability window of the liquid electrolyte, suggesting that the electrolyte molecules can decompose when contacting any exposed (meaning without SEI) electron-conductive surface on the anode side by accepting electrons from it. However, the decomposition reactions are complex, and not all decompositions result in *solid* SEI formation. Some soluble species may be generated and could play the role of $\mathrm{SRM/SRM}^{m+}$, even only temporarily. When Lithium metal is used as the working or counter electrode, with the continuous proliferation of surface areas and fresh electrolyte decomposition, $\mathrm{SRM/SRM}^{m+}$ may be continuously produced and released into the liquid electrolyte. Note also that the high volume expansion of anode/cathode can break the hermeticity (liquid-tightness) of SEI, and create transient opportunities for existing $\mathrm{SRM/SRM}^{m+}$ to contact electron-conducting surfaces and transfer electrons.

Indeed, all electrode materials with tendency for morphological instabilities and too-low or too-high working voltage (below 1 V or above 4.5 V vs Li metal) may present this problem. With volume change, stress relaxation, and exposure of fresh conductive surface, $\mathrm{SRM/SRM}^{m+}$ may be continuously released/turned over into the liquid electrolyte, along with the buildup of solid SEI passivation. In addition, a lot of the electrode materials were synthesized hydrothermally, and even after high-temperature treatment they may still contain protons in the material. These protons and other elements may also be released into the electrolyte during morphological changes and can cause parasitic reactions that consume free electrons in unexpected ways.

Typical battery cell is cycled galvanostatically within fixed voltage range $[U_{\min}, U_{\max}]$, with a voltage upswing $U_{\min} \rightarrow U_{\max}$ half cycle and a voltage downswing $U_{\max} \rightarrow U_{\min}$ half cycle. Inside the idealized electrolyte used in an idealized battery, only $\mathrm{Li^+}$ would be transported and stowed in a non-blocking manner. However, salt anions like $\mathrm{PF_6^-}$ or $\mathrm{TFSI^-}$ in the electrolyte may diffuse even faster than $\mathrm{Li^+}$ in liquid electrolyte due to smaller solvation shells. But in an idealized battery these anions are neither emitted from nor accepted into the electrodes (blocking), which can only host $\mathrm{Li^+}$/polarons. Ignoring capacitive contributions from all other ions (proportional to the electrochemical surface area; also, capacitive contributions are highly reversible between voltage upswing and downswing) in such idealized battery cell, the number of electrons (Q) that is passed through the outer circuit must be rigorously equal to the number of $\mathrm{Li^+}$ ions transmitted through the liquid electrolyte. The idea of "Coulomb titration" is that we can infer what happens to the $\mathrm{Li^+}$ ions by collecting electron flow statistics. Take graphite as the anode and $\mathrm{LiCoO_2}$ as the cathode, in the first half-cycle charging from $U_{\min} \rightarrow U_{\max}$, Q_{charge} electrons are metered to flow through the outer circuit. This would imply, based on the reasoning above, that Q_{charge} $\mathrm{Li^+}$ ions are transferred from cathode to anode through the liquid electrolyte. In the discharging half-cycle $U_{\max} \rightarrow U_{\min}$, $Q_{\mathrm{discharge}}$ electrons are metered to flow back through the outer circuit. This would imply, based on the reasoning above, that $Q_{\mathrm{discharge}}$ $\mathrm{Li^+}$ ions returned from the anode to the cathode through the liquid electrolyte. What does it mean if $Q_{\mathrm{charge}} \neq Q_{\mathrm{discharge}}$? The "Lithium titration hypothesis" above would imply that there is a *net transfer* of $\mathrm{Li^+}$ from cathode to anode (if $Q_{\mathrm{discharge}}/Q_{\mathrm{charge}} < 1$) or from anode to cathode (if $Q_{\mathrm{discharge}}/Q_{\mathrm{charge}} > 1$) *within a full cycle*. Such would be a Coulombic Efficiency (CE) problem, similar to trade imbalance between two countries. If we define the Coulombic Efficiency of the *n*th full-cycle as:

$$\mathrm{CE}_n \equiv Q_{\text{2nd half cycle}}(n)/Q_{\text{1st half cycle}}(n), \tag{11}$$

where 1st half cycle is the charging process and 2nd half cycle is the discharging process for the $\mathrm{LiCoO_2}$/graphite case here, and define the Coulombic Inefficiency (CI) as its complement:

$$\mathrm{CI}_n \equiv 1 - \mathrm{CE}_n. \tag{12}$$

Then persistent positive signs of CI_n would imply persistent transfer of Li^+ (and accompanying electron) from the cathode to anode side. Vice versa, persistent negative signs of CI_n would normally imply a net transfer of Li atoms from anode to cathode over full cycles (this would only make sense if the anode side has cycleable Li atom to begin with, like solid Li metal anode with certain excess).

The Coulombic Inefficiency is often interpreted to characterize SEI formation and loss of cycleable Lithium, an irreversible damage accumulation phenomenon like fatigue that gradually drives a system out of balance. The reasoning is as follows: suppose the Lithium titration hypothesis – that is, there is one-to-one correspondence between electron flow in outer circuit and cycleable Li^+ flow through the electrolyte – holds, then the reason that smaller number of cycleable Li returns from one side is likely that they get trapped on the other side, namely they have turned non-cycleable. For the sake of discussions, take, for example, superabundant lithium metal as the anode and some form of Sn nanostructures as the cathode. This cell actually discharges first, so in the 1st half cycle Sn gets lithiated by discharging, and in the 2nd half cycle SnLi_x gets delithiated by charging. The following sequence of electron flow numbers are measured for $n = 1, 2, 3, \ldots$ cycles:

$$Q_{\mathrm{discharge}}(1), Q_{\mathrm{charge}}(1), Q_{\mathrm{discharge}}(2), Q_{\mathrm{charge}}(2), \ldots, Q_{\mathrm{discharge}}(n), Q_{\mathrm{charge}}(n), \ldots. \tag{13}$$

Even though SEIs form on both the anode and the cathode, because of the superabundant Lithium (like "40× in excess") the anode should have no problem delivering Lithium out or accepting Lithium for foreseeable number of cycles, whenever the local voltage demands it. However, the cathode might have problem in accepting Lithium, due to disruption of conductive networks, etc., which changes R_{Ohm}, R_{W}, R_{ct}, or even because of phase transformation of the cathode. These chemomechanical degradations of cathode then likely lead to:

$$Q_{\mathrm{discharge}}(1) > Q_{\mathrm{discharge}}(2) > \cdots > Q_{\mathrm{discharge}}(n), \tag{14}$$

a trend that can be defined as "cathode's capacity decay" (as this is not anode's problem). Most papers publish such capacity decay as their main result. Occasionally, one may even see:

$$Q_{\mathrm{discharge}}(1) < Q_{\mathrm{discharge}}(2) < Q_{\mathrm{discharge}}(3) \ldots \tag{15}$$

a process known as "electrode activation" due to opening of new conductive networks, nucleation of more accommodating phases, etc. The CEs are also presented as

$$CE_1 \equiv Q_{\mathrm{charge}}(1)/Q_{\mathrm{discharge}}(1),\ CE_2 \equiv Q_{\mathrm{charge}}(2)/Q_{\mathrm{discharge}}(2), \ldots,\ CE_n \equiv Q_{\mathrm{charge}}(n)/Q_{\mathrm{discharge}}(n) \tag{16}$$

We note that (16) has half the length as the full sequence of numbers in (13). Indeed $\{\mathrm{CE}_n\}$ might bring complementary information to (14), cathode's capacity decay trend, since (14) and (16) contain exactly the same information as the full sequence in (13). What new information then does $\{\mathrm{CE}_n\}$ include? Considering an extreme case:

$$Q_{\mathrm{discharge}}(1) = Q_{\mathrm{discharge}}(2) = \cdots = Q_{\mathrm{discharge}}(n), \tag{17}$$

an ideal situation that cathode does not degrade, i.e., an *immortal* electrode. Suppose

$$\mathrm{CE}_1 = 70\%,\ \mathrm{CE}_2 = 90\%,\ \mathrm{CE}_3 = 95\%, \ldots,\ \mathrm{CE}_{n \geqslant 50} \equiv 99.5\%, \ldots \tag{18}$$

or equivalently,

$$\mathrm{CI}_1 = 30\%,\ \mathrm{CI}_2 = 10\%,\ \mathrm{CI}_3 = 5\%, \ldots,\ \mathrm{CI}_{n \geqslant 50} \equiv 0.5\%, \ldots \tag{19}$$

Given (18), most battery industry people would reject the cathode material for the following two reasons: (a) the stabilized CE ($\mathrm{CE}_{\mathrm{stabilized}} = \mathrm{CE}_{n \geq 50}$) of 99.5% is too low. Battery industry lore says that one needs $\mathrm{CE}_{\mathrm{stabilized}} = 99.9\%$ ($\mathrm{CI}_{\mathrm{stabilized}} = 0.1\%$) in order for a full cell to cycle 200 times; (b) the transient CE (e.g. initial cycle CE) of 70% is too low, or the transient CI of 30% is too high. Unless an efficient way of pre-lithiation can be devised, there is no hope of pairing this Sn-containing nanostructure with $\mathrm{LiCoO_2}$ or other standard cathodes.

The argument for (a) is: assuming the Lithium titration hypothesis holds, then $\mathrm{CI}_{\mathrm{stabilized}} = 0.5\%$ means in each full cycle, 0.5% of the cathode capacity worth of cycleable Lithium is lost in forming SEI on cathode. They were transported "live" out of anode, but a smaller fraction returned from cathode, for the same voltage interval. In other words, there is net 0.5% the cathode capacity worth of cycleable Lithium transported from anode to cathode. The cathode side net-gains 0.5% Lithium, but since $Q_{\mathrm{discharge}}(n)$ stay unchanged, this means the gain is not in cycleable Lithium, but in "dead" Lithium on the cathode side. The anode side net-loses Lithium. This is not a problem in half-cell test, but will be a severe problem in commercial full cell, when, for example, $\mathrm{LiCoO_2}$ is paired against the Sn nanostructures. In that case, we would like to have equal capacity in the 1st cycle, since $\mathrm{LiCoO_2}$ is very heavy and expensive (on a molar basis, Co is 5× more expensive than Li). Unlike in half-cell tests where there is superabundant Lithium, in such full cell the cycleable Lithium is severely rationed, because for the each cycleable Lithium atom (which is already expensive) we need to bring an even more expensive and heavy Co atom on the $\mathrm{LiCoO_2}$ side. Now imagine what will happen if we lose 0.5% Lithium from $\mathrm{LiCoO_2}$ to SEI of the Sn nanostructure every cycle. This would mean with every full cycle, 0.5% of the Co atoms on $\mathrm{LiCoO_2}$ no longer can be matched with Li when U_{min} is reached: they stay "widowed" at charge state Co^{4+}. It is easy to show then:

$$(0.995)^{200} = 0.367, \tag{20}$$

which means at the 200th cycle only 36.7% of the Co atoms on the $LiCoO_2$ side can undergo $Co^{4+} \rightarrow Co^{3+}$ transformation as smaller and smaller number of cycleable Lithium come in. Note that in this scenario, both the Sn nanostructure and $LiCoO_2$ can stay structurally perfectly healthy: there does not have to be any change in R_{Ohm}, R_W, R_{ct} or the active particles themselves. It is just that significant amount of the cycleable Lithium inventory that $LiCoO_2$ brought with is now trapped irreversibly in the SEI debris, which may have already fallen off of the Sn anode surface due to spallation. To test whether this is true, one can disassemble the full cell, take out the $LiCoO_2$ electrode, and pair it against Li metal, and see whether the half-cell capacity of the $LiCoO_2$ electrode fully recovers. If it does, we can bring back this re-lithiated $LiCoO_2$ against the Sn electrode, and we should recover our original $n = 1$ capacity again.

The above is just a hypothetical scenario. Nonetheless people use this guideline in industry. Since

$$(0.999)^{200} = 0.818, \tag{21}$$

and 80% capacity retention is the definition of cell life. Eq. (21) justifies the battery industry lore that one would need $CE_{stabilized} = 99.9\%$ ($CI_{stabilized} = 0.1\%$) in order to enable a Li-matched full cell to cycle 200 times.

The above estimations show that, generally, graphing CE_n on a linear scale (especially from 0 to 1) is not a good way to present the data since huge difference in full-cell life performance can be expected between CE 99.5% and 99.9%, or even between CE 99.9% and 99.99%. A $CE_{stabilized}$ of 99% from half-cell test is often not an acceptable number: it suggests the electrode being tested could be wasting away 1% of the cycleable Lithium per cycle, so the "live" lithium inventory of a Li-matched full-cell could be more than halved in 70 cycles, and the full cell is expected to die out of lithium exhaustion (or by closely related mechanism of electrolyte dryout), even if the cathode and anode stay structurally healthy themselves. One really needs to know whether $CE_{stabilized}$ is 99.9% or 99.99%. But this is hard to tell graphically from a linear-scale plot of the $\{CE_n\}$ data. Unfortunately, this paradigm of graphing $\{CE_n\}$ on the right on [0,1] linear axis alongside plotting "capacity decay" (14) on the left axis with n, has really proliferated in the literature. Many researchers also insinuated, wrongly, that $CE_{stabilized} > 99\%$ means good performance. We here strongly recommend plotting $|CI_n|$ instead, and also on a logarithmic scale, as illustrated below.

Having noted the critical importance of the Coulombic Efficiency or, rather, Inefficiency, for influencing full-cell cycling performance of the testing electrodes, we want to qualify that the connection between $\{CE_n\}$ and SEI/irreversible lithium exhaustion is not always true. Even though there is often positive correlation between the two mechanistically, the correlation coefficient could vary anywhere from close to 1 to close to 0. This is because the arguments made above for ideal electrolytes, though helpful qualitatively, are not rigorous for real electrolytes and cells.

Firstly, the Lithium titration hypothesis does not hold rigorously, as shown in the previous SRM/SRM^{m+} discussions. There could be other soluble, redox-capable species in the liquid electrolyte besides Li^+, which may exist permanently or temporarily, especially when the solid electrode contents on either side undergo morphological disruptions and expose fresh conductive surfaces that can react with the liquid, release these species, and provide/accept electrons. In the molten-salt battery literature, there exist full-cell battery demonstrations that can cycle for thousands of cycles with $CE_{stabilized} = 99\%$, violating predictions like (20) [60]. This is understood as being caused by the small but finite solubility of neutral metal atoms (as well as metal cations) in the molten-salt, forming soluble SRM/SRM^{m+} couples. This particular battery chemistry involves no SEI and very little irreversible side reactions. In addition, in the Li-Sulfur [61] and Li-oxygen battery literature, it has been shown that with SRM/SRM^{m+} the cell can be charged indefinitely, to $2\times$, $10\times$, even $100\times$ the discharge capacity [62], meaning the CE can be tuned to as low as one wants (like 4%). Yet a lithium-matched battery full cell has been demonstrated to cycle for hundreds of cycles, which is clearly impossible with predictors like (20). Finally, rechargeable batteries can self-discharge: that is, over a long timescale like months, a fully charged battery can lose energy even though there is no exterior electron flow. So over this long timescale, these batteries can manifest Coulombic efficiency $\ll 1$, but with little permanent damage. The gist of these examples is while that the "trade imbalance" in the electrons metered through the outer circuit reflects *side reactions*, not all side reactions are *irreversible*. Some of these side reactions are indeed irreversible, such as the formation of solid SEI that ties up cycleable lithium and dries out the electrolyte, the kind of reactions we want to avoid. But there could also be reversible side reactions that do not cause permanent damage to the cell and can use up some of the "lost electrons", complicating the interpretation of $\{CE_n\}$.

Philosophically, we should ask whether it is reasonable to expect to infer *all* information regarding both electrodes, based on *only* the exteriorly metered Coulombic titration data. The answer seems to be No. The data sequence contained in Eq. (13) gives us hints about the mechanisms, but an assured physical interpretation would require many other *in operando* or post-mortem characterizations, for example direct measurement of individual electrode weight gain using Electrochemical Quartz Crystal Microbalance (EQCM), gas release using Differential Electrochemical Mass Spectrometry (DEMS), etc., and a variety of imaging and diffraction techniques, on both electrodes. This motivates the remaining sections of this chapter.

Even though (14) and (16) were presented as complementary information, there can also be causal relation between "capacity decay" in (14) and CE sequence in (16), as the extra volume from SEI growth and shedding can certainly disrupt R_{Ohm}, R_W, and R_{ct}. These physical mechanisms can be individually characterized by EIS, where the linear-response (small ΔU) characteristics of an electrode is probed as a function of the frequency ω, at any given state of charge (SOC) of the electrode. The $\omega \rightarrow 0$ asymptote (Warburg rise $\mathrm{Re}Z = R + \sigma_{Warburg}\omega^{-1/2}$) is more similar to battery operation, which requires accommodation of Li^+/polaron in the active particles, and thus provides information regarding transport within the anode or cathode particles [63]. The $\omega \rightarrow \infty$ response on the other hand requires rapid motion of Li^+ in electrolyte and electrons in conductive

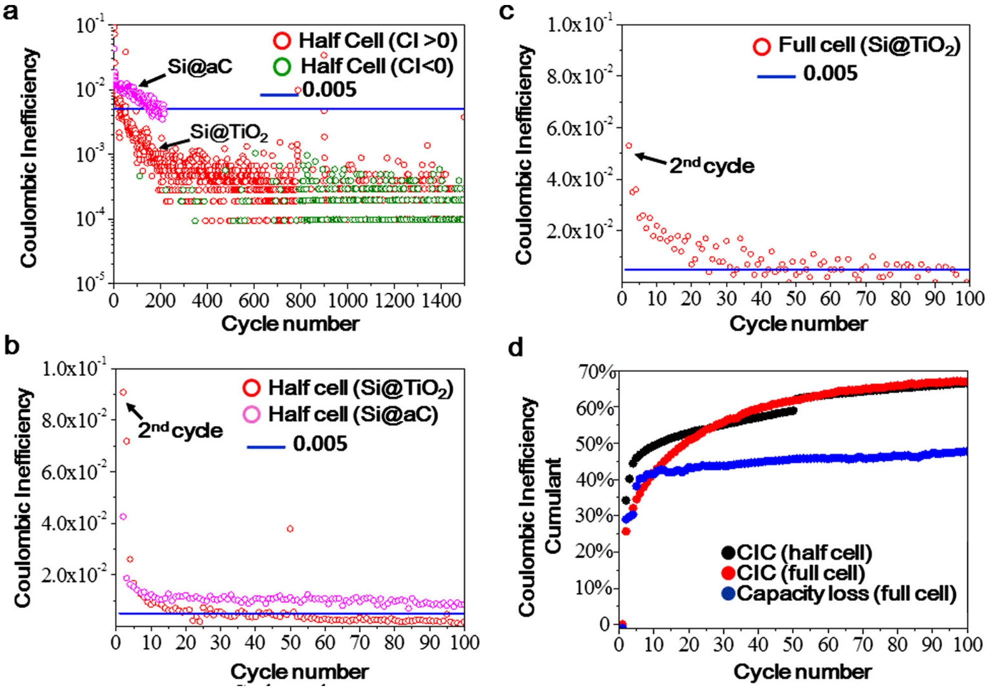

Fig. 4. A recommended scheme of graphing and analyzing Coulombic Inefficiency $\{CI_n\}$ data. In (a), one graphs $|CI_n|$ on a semi-log plot versus cycle number n. Red circles mean $CI_n > 0$, green circle means $CI_n < 0$, for a high-capacity Si-containing anode material Si@TiO$_2$ that has self-healing ability. The blue solid line denotes CE = 99.5%. The Si@TiO$_2$ anode beats the blue line in ~20 cycles, whereas a reference material, Si@aC (Si yolk in amorphous carbon shell), takes about 200 cycles. The CE readout precision of the electrochemical testing station is 10^{-4}, in other words CE = 0.9999 or CE = 1.0001 are the limiting readouts. The Si@TiO$_2$ anode first hits the machine precision of the electrochemical testing station in ~300 cycles, and a relentless logarithmic downward trend can be seen in the cloud of points, suggesting self-healing of Si@TiO$_2$ in earnest in the first few hundred cycles. For $n > 800$ there is about equal number of red and green circles around machine precision, indicating the Coulombic Efficiency has become >99.99%. This indicates self-healing has achieved a high degree of perfection. Not all materials can reach such perfection by repairing. Some materials have $\{CI_n\}$ that may rise again after a few hundred cycles. In (b) and (c), we look at the transient CI_n of the first tens of cycles, for both the half cell and full cell (matched against LiCoO$_2$). In (d), the Coulombic Inefficiency Cumulant $\{CIC_n\}$ is computed, and compared with the actual capacity decay of the LiCoO$_2$/Si@TiO$_2$ full cell. It is seen that the CIC_n(half cell), CIC_n(full cell) and capacity decay (full cell) largely correlate with each other, but both CIC_n(half cell) and CIC_n(full cell) give more pessimistic predictions than the actual full-cell performance. Taken from [65].

networks, therefore the $\omega \to \infty$ intercept of EIS provides information regarding long-range percolative transport R_{Ohm}, which may certainly be disrupted by the growth and shedding of SEI debris. The half-circle in between (or multiple half-circles) of EIS spectrum characterizes the interfacial redox reactions R_{ct} which are local, some of which reflects surface adsorption of reaction intermediates and electrocatalysis kinetics [64], that may also be changed by SEI buildup. This means after battery cycling, and upon charging/discharging to certain SOC, EIS could give us more detailed information regarding possible physical mechanisms of degradation.

CV can also be performed on either the anode or the cathode, or the electrolyte individually. It probes the large-ΔU nonlinear response of these components. For example, if there are SRM/SRM^{m+} generated in the electrolyte during half-cell or full-cell cycling, we could disassemble the cell and wash out the electrolyte, and perform CV on the isolated liquid electrolyte. We should be able to see the SRM ↔ SRM^{m+} redox peaks, just like we can see the Fe^{2+} ↔ Fe^{3+} redox peaks in aqueous medium. Seeing these soluble redox mediators in action does not require hosting electrodes, so Pt electrode should work. Also, if the electrode surface has some electro-catalytic/passivation effect on electrolyte side reactions, we should be able to see shifts in the reduction or oxidation peaks in their CVs compared to using Pt electrode. These experimental tools complement the half-cell or full-cell cycling data in determining the battery degradation mechanisms.

Fig. 4 shows the $\{CI_n\}$ data of a high-capacity self-healing LIB anode, Si@TiO$_2$ yolk-shell powders, which will be further reviewed in Section 5.5. The Coulombic Efficiency, or rather the Coulombic Inefficiency data, is presented in the recommended format of a semi-logarithmic plot versus the cycle number n. Several levels of performance can be noted: 99.5% (blue line), 99.9% (10^{-3}), and 99.99% (10^{-4}). The particular electrochemical testing station outputs four effective digits for the Coulombic efficiency, so the highest-precision machine readout for a cycle is CE = 0.9999 ($CI = 10^{-4}$) or CE = 1.0001 ($CI = -10^{-4}$). Even though the Si@TiO$_2$ yolk-shell powder has excellent gravimetric energy density and cyclability (thousands of cycles), due to the low tap density (0.4 g/cm^3), its volumetric specific capacity is still less than commercial graphite. In order to improve the volumetric specific capacity of this anode, we subsequently mechanically crushed the Si@TiO$_2$ yolk-shell powder, which that changes its density from the initial 0.4 g/cm^3 to 1.4 g/cm^3 after high-pressure calendaring, before injecting electrolyte into the cell and carrying out electrochemical tests. So initially, a lot of the TiO$_2$ shells (artificial SEI) are cracked, and the liquid electrolyte will flood some active Si yolks. This causes significant loss in the initial Coulombic efficiencies, in half-cell test against superabundant lithium (Fig. 4b), or in full-cell tests with 3mAh/cm^2 commercial $LiCoO_2$ cathode (Fig. 4c). Note that the initial lithiation capacity of the crushed Si@TiO_2 was selected to be $Q_{re}(n=1)=3$mA h/cm^2 too, so it was designed to be perfectly balanced with the 3 mA h/cm^2 commercial $LiCoO_2$ cathode in the first half cycle. But with such a large initial CI loss, the full cell is expected to become significantly imbalanced in the first tens of cycles. To adopt a uniform notation, the sequence of electron flows we measured for both half-cell and full-cell tests are defined to be:

$$Q_{re}(1), Q_{ox}(1), Q_{re}(2), Q_{ox}(2), \ldots, Q_{re}(n), Q_{ox}(n), \ldots. \tag{22}$$

where “re” means “reduction” or lithiation of the Si@TiO_2, and “ox” means “oxidation” or delithiation, between fixed voltage thresholds $U_{min}=0.01$ V, $U_{max}=1.0$ V. For full-cell cycling that is initially perfectly lithium-matched, we define the actual capacity fade ratio as

$$F_n \equiv \frac{1}{Q_{re}(1)}[Q_{re}(1) - Q_{ox}(n)]. \tag{23}$$

This tracks the actual performance of the full cell (including the 2nd half of the first cycle), which is what a commercial producer would care about. F_n is plotted in Fig. 4d as the blue dot, which is indeed rapidly rising in the first tens of cycles, due to trapping of cycleable lithium in SEIs.

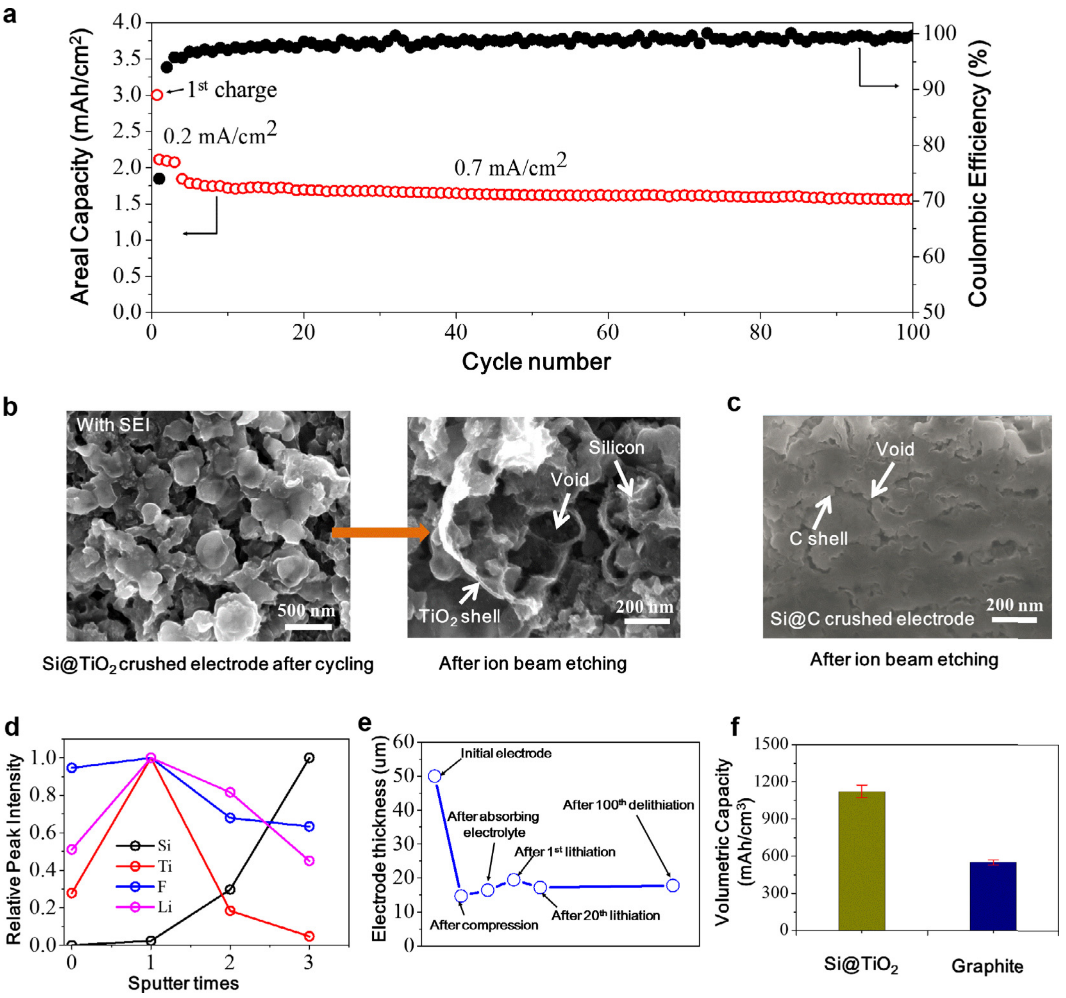

Fig. 5. Crushed Si@TiO_2 electrode vs Si@aC electrode. (a) Full-cell performance of crushed Si@TiO_2 cluster anode (2.1 mg/cm^2) paired with commercial 3 mA h/cm^2 $LiCoO_2$ cathode. (b) SEM image of Si@TiO_2 crushed electrode (30 MPa) after 100 cycles (full cell). Left part is with SEI and right part is after ion beam etching. (c) SEM image of Si@aC crushed electrode (30 MPa) after 50 cycles. (d) Relative peak intensity (Si, Ti, F, and Li) of Si@TiO_2 cluster electrode after 1500 cycles discharging and charging measured by X-ray photoelectron spectroscopy (XPS) during 3 ion sputtering times. Time 0 means before sputter. (e) Electrode thickness variation. (f) Volumetric specific capacity of Si@TiO_2 vs. commercial graphite. Taken from [65].

However, with repeated electrochemical cycling, something happens to the $\{\mathrm{CI}_n\}$ data of crushed Si@TiO$_2$, in contrast to similarly crushed Si@aC, which is a yolk-shell powder with amorphous carbon (aC) shell. We may define

$$\mathrm{CE}_{\mathrm{stablized}} \equiv \lim_{n\to\infty} \frac{1}{2M+1} \sum_{n'=n-M}^{n+M} \mathrm{CE}_{n'}, \quad \mathrm{CI}_{\mathrm{stablized}} \equiv \lim_{n\to\infty} \frac{1}{2M+1} \sum_{n'=n-M}^{n+M} \mathrm{CI}_{n'} \tag{24}$$

where $2M + 1$ is a running-window average. From Fig. 4a we see that it is possible that $\mathrm{CE}_{\mathrm{stablized}}$ of crushed Si@TiO$_2$ could become better than 99.99%. In contrast, Si@aC never reached CE = 99.9% before the full cell died.

This is interpreted as the following: with repeated volume expansion/shrinkage of the Si yolks, there is a pumping action that ejected the electrolyte out. Simultaneously, there is a self-repair action where the cracks on TiO$_2$ shell were gradually glued with naturally formed SEI since cycling begins, to make the crushed system more and more hermetic. The eventual degree of perfection of this self-repair and hermiticity against liquid electrolyte invasion should be amazing, as reflected in $\{\mathrm{CI}_n\}$. On the semi-log plot of Fig. 4a where red circles mean $\mathrm{CI}_n > 0$ and green circle means $\mathrm{CI}_n < 0$, we see that the crushed Si@TiO$_2$ beats the blue line of CE = 99.5% in ~20 cycles. In contrast, Si@aC takes about 200 cycles to get to 99.5%. Later, we see that the crushed Si@TiO$_2$ hits the machine precision of the electrochemical testing station in ~300 cycles, in a relentless logarithmic downward trend shown in Fig. 4a. This means, qualitatively, that the self-healing of Si@TiO$_2$ happened in earnest in the first few hundred cycles. After $n > 800$, there is about equal number of red and green circles around machine precision, meaning the Coulombic Efficiency of crushed Si@TiO$_2$ has become "better than 99.99%". This means self-healing/self-sealing can ultimately achieve an astonishing degree of perfection. Not all nanostructured materials can reach such perfection, as we have seen that some high-capacity anode materials have $\{\mathrm{CI}_n\}$ rising again after a few hundred cycles, and have never touched 99.99%. Corroborating the $\{\mathrm{CI}_n\}$ data, when we opened up the Si@aC anode after 100 cycles, we see the originally empty spaces between yolks and shells are completely filled with SEI debris (Fig. 5d), similar to the situation with unprotected Al anode where SEI keeps falling off [66]. Bad-CE anodes tend to be completely clogged by SEI debris after some cycling. This suggests that the aC shell, especially after pressing, cannot provide hermiticity against liquid electrolyte invasion: the self-healing action is too weak. We speculate this is because of the weaker bonding between aC and the SEI to be formed later, and the fact that the aC shells have a lot more cracks to begin with due to intrinsic fragility. In contrast, when we cut open the Si@TiO$_2$ anode with ion beam after 100 cycles, we see there is still much space between the Si yolk, and the shells surrounding it (Fig. 5c). Liquid electrolyte must be fully stopped at the outside eventually, and no longer touches Si directly. The analogy we draw is building a hut out of pieces of sheet metals (TiO$_2$) and mud (SEI), with which one can eventually keep out the rain.

To check quantitatively how the actual capacity decay F_n defined in (22) correlates with the past Coulombic Inefficiencies, we can define a "Coulombic Inefficiency Cumulant (CIC)", as

$$\begin{aligned}\mathrm{CIC}_n &\equiv \tfrac{1}{Q_{\mathrm{re}}(1)}[Q_{\mathrm{re}}(1) - Q_{\mathrm{ox}}(1) + Q_{\mathrm{re}}(2) - Q_{\mathrm{ox}}(2) + \cdots + Q_{\mathrm{re}}(n) - Q_{\mathrm{ox}}(n)] \\ &= \mathrm{CI}_1 + \tfrac{Q_{\mathrm{re}}(2)}{Q_{\mathrm{re}}(1)}\mathrm{CI}_2 + \cdots + \tfrac{Q_{\mathrm{re}}(n)}{Q_{\mathrm{re}}(1)}\mathrm{CI}_n\end{aligned}. \tag{25}$$

CIC_n aims at tracking how much cycleable Lithium is lost to SEI formation, *if* the Lithium titration hypothesis holds rigorously. Both CIC_n and F_n are computable based on experimental data (21), and plotted against n in Fig. 4d. We see that if

$$Q_{\mathrm{re}}(n'+1) = Q_{\mathrm{ox}}(n') \tag{26}$$

holds rigorously for all n', then there would be

$$\mathrm{CIC}_n = \mathrm{F}_n \tag{27}$$

exactly. However we find that Eq. (26) does not hold exactly in reality. Instead, the left-hand side of (27) is on average larger than the right-hand side of (27). This is difficult to reconcile with the Lithium titration hypothesis, because if true it would mean the LiCoO$_2$ side keeps outputting more Lithium than receiving for the same full-cell voltage range. This then causes the actual F_n to be "more optimistic" than CIC_n quantitatively. In the initial few cycles, CIC_n tracks F_n quite well, for our Si@TiO$_2$/LiCoO$_2$ full-cell battery, but then CIC_n starts to deviate significantly from F_n in the later cycles. At the end of the 100th cycle, CIC_n of the half cell and CIC_n of the full cell both predict ~65% capacity decay. But the actual full-cell capacity decay is only 45%. Hence, the CIC_n prediction is overly pessimistic by about 50%. In other battery contexts, we have found CIC_n prediction can be overly pessimistic by few hundred percent or more. This means CIC_n provides qualitative, but not quantitative prediction of cell death by lithium exhaustion, and predictions like (20) can be overly pessimistic.

The thickness of a high-capacity electrode can show significant variations at different stages of preparation and use. Present cell designers put stringent requirements on how much the thickness can change, which can become a safety issue since the current collectors and separators may have to move in order to adjust to the thickness change of one electrode. The normal requirement from industry is that the anode thickness cannot expand more than 50% (e.g. 50 μm anode after calendering can become no more than 75 μm after 1000 cycles). In the example above, before calendering, the thickness of Si@TiO$_2$ powders laid on the Cu foil was 50 μm, which decreased to 14.7 μm after hard pressing, when some TiO$_2$ shells are broken/cracked. After a night of immersion in liquid electrolyte, the thickness swelled to 16 μm (Fig. 4f). Surprisingly, after assembling a full cell versus 3 mA h/cm^2 commercial LiCoO$_2$, it still showed decent performance, exhibiting stable cycling at industrially meaningful areal capacity and current density, under severe lithium rationing. For a relatively high areal loading

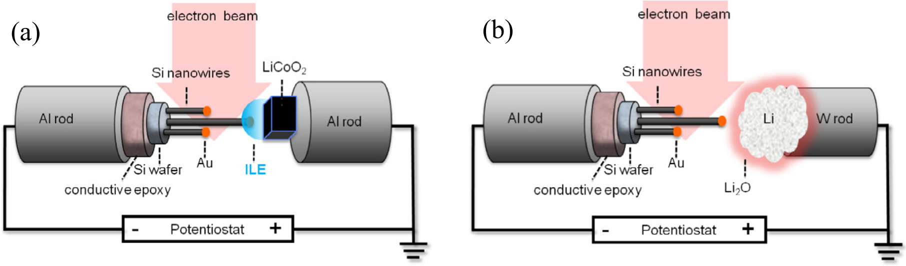

Fig. 6. Schematics of the open-cell configuration of the nanobattery platform for *in-situ* TEM characterization. Lithiation initiates by applying a negative potential on the working electrode with respect to the counter electrode. (a) A liquid cell consisting of single SiNWs as the anode, ionic liquid electrolyte (ILE), and $LiCoO_2$ as the cathode. (b) A solid cell consisting of single NWs or NPs as the working electrode, bulk Li metal as the counter electrode, and the natively grown Li_2O as the solid electrolyte.

of Si@TiO_2 active content (2.1 mg/cm^2), with first discharge capacity $Q_{re}(1) = 3$ mA h/cm^2, the lithium-matched full cell still outputs 1.6 mA h/cm^2 after 100 cycles, at a current density of 0.7 mA/cm^2. The thickness of the electrode increased by 22% (16 → 19.5 μm) after the first lithiation. After $n = 20$ (past lithiation half cycle), when the CE became as high as 99.5%, the electrode thickness was still about 17.2 μm. From 20th (lithiation stage) to 100th cycle (delithiation stage), the electrode thickness increased by only 0.6 μm (3.4%), which means there was almost no electrode volume change in the later cycles, meeting the design criterion on electrode thickness change. Based on the areal capacity (1.6 mA h/cm^2) and electrode thickness (17.8 μm) at $n = 100$, the volumetric capacity of the crushed-and-cycled Si@TiO_2 electrode is about 1100 mA h/cm^3, two times the volumetric capacity of commercial graphite.

The main drawback of this self-healing high-capacity material (both gravimetric and volumetric) is that despite the final degree of perfection, it takes too long (few hundred cycles) and too much cycleable lithium (~50%) to get there. But the analysis above points to measures, such as pre-lithiation using sacrificial lithium sources and structural improvements of the nanomaterials, may overcome the hurdle. Furthermore, the presented analysis methods (MG/MV metric, semi-logarithmic plot of $\{CI_n\}$, CIC_n vs F_n comparison) provide tools for mining the electrochemical data as thoroughly as possible. While the half-cell cycling data, lithium-rationed full-cell cycling data, CV, EIS, GITT etc. cannot tell us everything about what happens inside the electrodes, when complemented by detailed microstructural characterizations to be introduced next, it is possible to fully reveal the mysteries about the inner workings of a battery cell, and come up with mitigation strategies to improve the expected full-cell performance.

2.3. In-situ SEM/TEM studies

Performance characterization and diagnosis of rechargeable batteries have often relied on cell-level tests, assisted by the post-mortem TEM/SEM characterization of lithiated/delithiated products. The real-time information of phase transformation and microstructural evolution, particularly the dynamics of the buried interfaces in electrodes during charge-discharge cycles, are more challenging to acquire but helpful for mechanistic understanding (see sections above). To enable in-situ diagnosis of battery degradation at the nanoscale, several experimental techniques have been developed. Among these techniques, in-situ TEM provides high spatial resolution for unique characterization of microstructure changes in electrodes during the electrochemical processes, critical for degradation analysis.

Huang et al. developed the first nanoscale battery suited for in-situ TEM testing and characterization of electrode materials in contact with liquid electrolyte [18]. This nanobattery platform adopts an open-cell configuration, in contrast to the sealed-cell configuration, by using vacuum-compatible electrolytes, which are either ionic liquids with a negligible vapor pressure (Fig. 6a) or Li-containing solid-state electrolytes (Fig. 6b). The liquid cell (Fig. 6a) consists of single nanowires (NWs) of a few microns length as the working electrode and ionic liquid (ILD) as the electrolyte [18]. The solid cell (Fig. 6b) consists of individual nanowires as the working electrode and Li_2O as the solid electrolyte (e.g., [34,43,47]). Since the solid electrolyte is a very thin layer (a few nm), the solid cell enables electrochemical cycling of single nanoparticles (NPs). For both cases, the working electrodes can be either anode or cathode, depending on the chosen counter electrodes. The open-cell configuration allows real-time and atomic-scale resolution microstructure investigation. Analytical TEM techniques such as electron energy loss spectroscopy (EELS), electron diffraction patterns (EDPs), and energy dispersive X-ray spectroscopy (EDS) can be concurrently performed for electronic, crystalline structure, and chemical composition analysis.

Electron beam (e-beam) heating, irradiation and other damages have become concerns for the in-situ TEM analysis. Comparisons between the in-situ and ex-situ electrochemical processes can be used to assess the e-beam effect. Experimental calibration has concluded that under the standard conditions the e-beam effect on lithiation and delithiation is negligible. In practice, several measures, such as using low energy e-beam or turning the beam on only when taking images (with lower and lower frame rates) during the in-situ experiments, can be taken to perform a "convergence test" on the e-beam effect.

2.4. Measurement of mechanical properties

During electrochemical cycling, the electrode materials undergo a series of phase transformations, accompanied with strain and stress generation due to Li insertion and extraction. The mechanical properties and the level of the mechanical stress generated in the lithiated products depend on the charge state and Li concentration. Several experimental techniques have been adopted to characterize the mechanical properties at different states of charge, including in-situ tensile test of single nanowires [67,68], nanoindentation [69–71], wafer-curvature measurements of thin-film stress [72–75], and Raman microscopy [76]. Results from the mechanical measurements provide inputs for chemomechanical modeling.

In-situ tensile testing has been used to measure the mechanical properties of lithiated SiNWs [67,68]. The electrochemical lithiation and mechanical characterization were carried out in an immediate sequence within TEM or SEM, thereby eliminating any possible side reactions that may cause the microstructure or phase changes. Kushima et al. developed a dual probe, *in-situ* lithiation and tensile testing method for SiNWs [67]. Similar *in-situ* testing method was developed by Boles et al. [68]. From the load-displacement curves, the Young's modulus, fracture strength, permanent plastic deformation, and creep parameters can be derived. While such in-situ testing is powerful and accurate, it is costly and difficult to operate, making systematic characterization unrealistic.

Nanoindentation is a powerful technique to measure the elasto-plastic properties of lithiated electrode materials and SEI, including the Young's modulus, hardness, stress exponents in creep, and fracture toughness. Nanoindentation experiments are commonly conducted at ex-situ conditions under which the electrode material is first lithiated to a certain state of charge, then transferred into an oil-filled liquid cell to measure the mechanical properties within a nanoindentation holder [69,70,77,78]. Experimental data of nanoindentation for electrodes are informative in literature, yet there still exists a range of uncertainties in the accuracy of the obtained parameters. One technical challenge is a lack of reliable tools to characterize the behavior of electrodes under realistic and complex chemical conditions. The operation of battery electrodes is extremely sensitive to the environment, and a trace of oxygen or moisture could cause a number of undesired side reactions. It remains a challenge to perform nanoindentation measurements under precise control of the electrochemical reactions and free of undesired side reactions. In addition, *ex-situ* measurements miss the intimate coupling between electrochemical reactions and mechanics. In the real scenario of the electro-chemo-mechanical behaviors of electrodes, electrochemistry and mechanics proceed concurrently and influence each other [73,79,80]. For example, for a material under chemical reactions, the host atomic bonds are frequently broken and the valence state dynamically changes. The "material state" is different from the post-reacted structure even with the same composition. As such, the mechanical properties measured *ex-situ* under mechanical loading could be significantly different from that under *in-situ* concurrent electrochemical and mechanical loading.

The wafer-curvature method is an effective technique for measuring the stress evolution in a thin film electrode during *in-situ* lithiation and delithiation cycling. Li insertion and extraction result in a biaxial stress state in the thin-film electrode deposited on an elastic substrate. The thin film exerts forces on the substrate, causing it to elastically bend. The bending curvature of the substrate can be monitored with a multi-beam optical sensor. The average stress in the film can be deduced from the substrate curvature using the Stoney's equation. This curvature method has been utilized to measure the stress evolution in $LiCoO_2$ and $LiMn_2O_4$ cathode [81,82] and more recently in amorphous Si (*a*-Si) thin-film anodes [83,84]. Pharr et al. have extended this approach to estimate the fracture toughness of lithiated Si and Ge [74,85,86]. Recently, Wang et al. have integrated the thin-film bending and nanoindentation tests to measure the fracture toughness of lithiated Si at different Li concentrations [75]. Reciprocal to the testing paradigm above where one imposes a potential and measure the mechanical responses, one could also impose cyclic mechanical bending displacement and measure the resulting electromotive potential/current, as an alternative diagnostic tool of electrode fatigue. This effect has also been exploited as an electrochemical way to harvest mechanical energy [87].

2.5. Multiscale and multiphysics modeling

Similar to the failure processes in other materials, chemomechanical degradation of electrode materials features phenomena occurring at different length and time scales, encompassing chemical reactions at the reaction front and fracture at a crack tip; the dynamics of point and line defects; the long-range interaction and organization of microstructures (such as dislocations and nanopores) at the mesoscale, the morphological evolution and fracture on the level of constituent material building blocks, and the interactions of the materials building blocks with binders and conductive agents (carbon black) at the electrode paste level. The multiscale and multiphysics nature of electrode failure presents a grant challenge to the theoretical and computational modeling.

Models at different length scales have been developed to characterize the degradation of battery materials. At the electronic structure level, *ab initio* simulations have been performed to extract the binding energy and the rate parameters (diffusivity, reaction rate, etc.) of Li in the host materials [88–98]. At the atomic scale, molecular dynamics (MD) with reliable force fields have been carried out to simulate phase transformations, phase-dependent material properties, microstructural evolutions, defect nucleation and motion [99–101]. At the continuum level, multiple field equations coupling chemical reaction, Li diffusion, deformation and stress generation can be solved to predict overall material deformation morphology and chemomechanical failure [53,54,73,79,80,102–118]. To achieve atomic-scale fidelity and at the same time obtain electrode-level morphology, it necessitates coupling these models across different length scales to understand the degradation mechanisms (e.g., [119]).

At the continuum level, Li transport and lithiation-induced stress are described by field variables, i.e., Li concentration $c(\mathbf{x};t)$ and the Cauchy stress $\sigma(\mathbf{x};t)$, respectively; both varying as functions of position $\mathbf{x}$ and time t. Li transport in the host materials involves simultaneous Li diffusion and chemical reaction. The chemical reaction rate k is a function of the local Li concentration and mechanical stress state. On the other hand, Li concentration can be described by the classical conservation law, as

$$\partial c/\partial t + \nabla \cdot \mathbf{j} = 0 \quad \text{in} \quad \mathrm{V}, \tag{28}$$

where V is the volume occupied by the electrode and $\mathbf{j}$ is the flux: $\mathbf{j} = c(-\mathbf{M}\cdot\nabla\mu + \mathbf{v}_{\text{convection}})$, consisting of Onsager diffusion contribution driven by the gradient of the diffusional potential of Li μ, in addition to the convective contribution due to motion of the lattice. Here $\mathbf{M}$ is the mobility tensor of Li, which is generally a function of Li concentration. Similar to the chemical reaction rate, the diffusional potential of Li has contributions from the chemical, mechanical, and electrical components, i.e., $\mu = \mu(c;\sigma;\phi)$, where ϕ is the applied overpotential. Both the hydrostatic stress gradient and the change in the local material moduli contribute to the diffusional drive force [120,121]. Whether the electrochemical lithiation process is limited by chemical reaction or diffusion is material specific and local stress-state dependent.

While mechanical stress mediates chemical reaction and Li diffusion, chemical insertion of Li generates strain and stress. In the finite-strain framework, the total stretch rate tensor $\mathbf{d}$ is composed of three additive parts, $\mathbf{d} = \mathbf{d}^c + \mathbf{d}^e + \mathbf{d}^p$, where $\mathbf{d}^c$, $\mathbf{d}^e$, and $\mathbf{d}^p$ are the chemical, elastic, and plastic stretch rates, respectively [80,102,115,122–126]. The chemical strain rate $\mathbf{d}^c$ due to Li insertion is proportional to the time increment of Li concentration $\mathbf{d}^c = \boldsymbol{\beta}\dot{c}$, where $\boldsymbol{\beta}$ is the lithiation-induced dilational strain tensor. In general, $\boldsymbol{\beta}$ can be anisotropic and adopts different values in the three dilational directions [102,127]. The elastic and plastic stretch rates and the elastic spin are related to the stress rates, formulating the constitutive relations for the elastic and plastic components, respectively. In particular, the pristine, unlithiated domain is modeled as an elastic material [80,102,115,122–126], while the lithiated phase is modeled as an isotropic, perfect elasto-plastic material or rate-dependent plastic material [70,73,115,123,128–131]. The elastic constants are generally phase-dependent. The plastic stretch rate, $\mathbf{d}^p$, obeys the associated J_2-flow rule. Since the mechanical process takes place in a much shorter time scale than Li transport, it is often assumed that mechanical equilibrium is met instantaneously during the electrochemical process:

$$\nabla \cdot \boldsymbol{\sigma} = 0 \quad \text{in} \quad \mathrm{V}. \tag{29}$$

Solving the two coupled governing equations with appropriate boundary conditions gives rise to both time-varying Li concentration profile and stress distribution in the electrode materials.

While Eqs. (28) and (29) are formally applicable everywhere, practically the fields can contain discontinuities at phase boundaries across which different constitutive laws apply for different phase domains. So quite often, one needs to convert and solve (28) as a moving-boundary Stefan problem, and (29) converted to a traction continuity condition across the boundary. In these problems, one also needs to specify the boundary migration speed as a function of the thermodynamic driving force, and therefore the bulk transport or plasticity may or may not be the rate-limiting factor. In other words, the kinetics may be interface reaction-controlled (short-range), transport-controlled (long-range), or could be under mixed control, as in standard phase transformation theory.

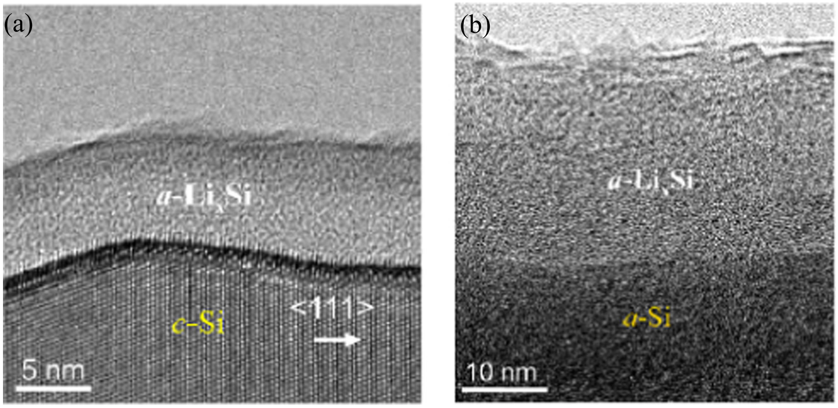

Fig. 7. Different lithiation mechanisms in c-Si and a-Si. (a) Two-phase lithiation in c-Si. Lithiation of c-Si proceeds by the movement of an atomically sharp interface that separates the lithiated amorphous phase and the unlithiated crystalline core [41,43]. (b) Two-step lithiation in a-Si [44,134], wherein a-Si is first lithiated to a-Li$_{2.5}$Si by the two-phase mechanism in the first step, and to a-Li$_{3.75}$Si by the single-phase mechanism in the second step.

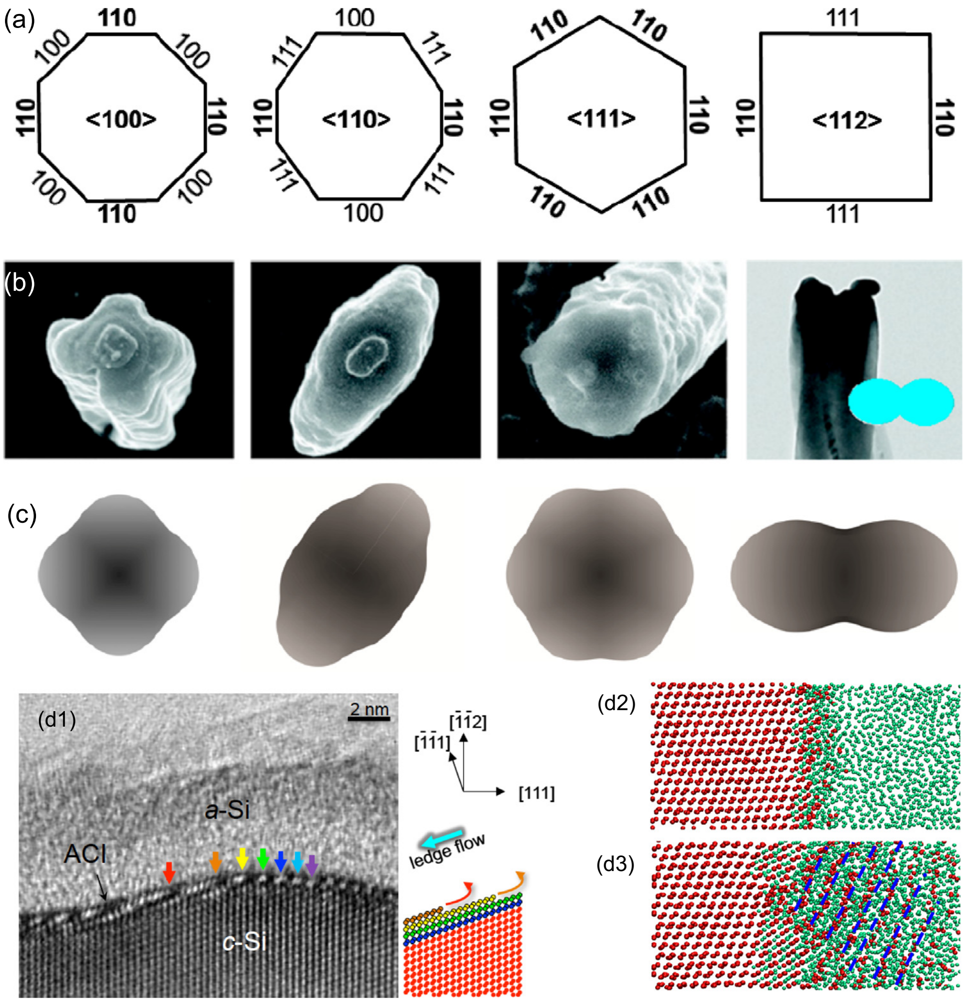

Fig. 8. Lithiation induced anisotropic swelling in c-Si. (a) Four c-SiNWs with different crystallographic orientations. Indices in the center represent the axial orientation, while those on the sides the orientations of the facets. (b) SEM (the first three columns) [29] and TEM (the last column) [43] images of fully lithiated crystalline c-Si structures, displaying anisotropic cross-sectional morphologies. (c) Anisotropic cross-sectional morphologies of lithiated c-SiNWs corresponding to the orientations shown in (a), predicted by the front-tracking finite element modeling [102]. (d1) Ledge-flow mechanism for the lithiation of c-Si reveals the atomic origin of the anisotropic swelling [41]. High resolution TEM image sequences showing the lithiation process by Li insertion into the spacing of the two neighboring {1 1 1} planes, leading to lateral ledge flow (marked by the color arrows) in the ACI and peeling off of the {1 1 1} planes (see the schematics on the side). (d2 and d3) MD simulations with ReaxFF showing the layer-by-layer dissociation in lithiation of Si (horizontal direction is [1 1 2]). The blue lines in (d3) show the peeling-off [1 1 1] planes.

3. Electrochemical lithiation and delithiation

3.1. Lithiation of Si

3.1.1. Two-phase lithiation of c-Si versus two-step lithiation of a-Si

Electrochemical lithiation of c-Si is temperature dependent, featuring temperature-dependent Coulometric titration curves and phase diagrams. When c-Si is lithiated at a high temperature (415 °C), four equilibrium phases, $Li_{12}Si_7$, Li_7Si_3, $Li_{13}Si_4$, and $Li_{22}Si_5$, sequentially form, resulting in a stepped galvanostatic voltage profile [132,133]. The most Li-rich phase $Li_{22}Si_5$ corresponds to the highest theoretical capacity (4200 mA h g^{-1}). At room temperature, however, formation of equilibrium intermetallic phases is kinetically hindered. Instead, c-Si is often lithiated through a two-phase mechanism via solid-state amorphization [41,43], wherein lithiation converts c-Si to an a-Li_xSi phase ($x \sim 3.75$) (see video v1). The two phases, the c-Si phase and the a-$Li_{3.75}Si$ phase, are separated by an atomically sharp reaction front [41,43,72], i.e., the amorphous-crystalline interphase (ACI) of ~1 nm in width, as shown in Fig. 7a. The lithiation reaction front thus coincides with a phase boundary, across which an abrupt change of Li concentration occurs, and lithiation proceeds by phase boundary migration. The two-phase lithiation mechanism is originated from the necessarily high Li concentration to break up the strong Si—Si bonds at the reaction front. The lithiated *a*-Li_xSi phase may suddenly crystallize to *c*-$Li_{15}Si_4$. However, in most experiments *a*-$Li_{15}Si_4$ stays as the terminal phase, possibly due to the suppression of crystallization by the applied cutoff voltage during lithiation. The terminal phase $Li_{15}Si_4$ at room temperature, either amorphous or crystalline, corresponds to a theoretical capacity of 3579 mA h g^{-1}. During delithiation, the *a*-$Li_{15}Si_4$ phase is converted to *a*-Si.

In contrast to the two-phase lithiation of *c*-Si, lithiation of *a*-Si involves a two-step process [44,134] (see video v2). In the first step, lithiation proceeds by the movement of a sharp phase boundary between *a*-Si and an *a*-Li_xSi ($x \sim 2.5$), i.e., a two-phase lithiation (Fig. 7b). The second step then occurs without a visible interface (i.e., single-phase lithiation), resulting in the terminal product *a*-$Li_{3.75}Si$. After fully lithiation of *a*-Si, delithiation and subsequent lithiation cycles proceed by a single-phase mechanism, indicating the essential difference in microstructures of the delithiated *a*-Si and its pristine form prior to the first lithiation.

3.1.2. Anisotropic swelling of c-Si

When lithiated to the terminal phases $Li_{15}Si_4$ or $Li_{22}Si_5$, Si undergoes ~280% and ~300% volumetric increases, respectively. The huge volumetric expansion may result in pulverization of the electrodes, delamination from the current collector, and cracking of the fragile SEI layer, causing irreversible capacity loss and low cycle life of the LIBs. Several independent studies have shown that lithiation induced swelling of *c*-Si structures is highly anisotropic, with predominant expansion along the $\langle 1\,1\,0 \rangle$ direction, in contrast to the isotropic swelling of *a*-Si upon lithiation. Liu et al. first observed through *in-situ* TEM imaging lithiation-induced anisotropic expansion of a $\langle 1\,1\,2 \rangle$ *c*-SiNW with two $\{1\,1\,0\}$ and two $\{1\,1\,1\}$ side facets [43] (Fig. 8a and b, the 4th column, and video v3). The measured expansion was 170% along the $\langle 1\,1\,0 \rangle$ direction, but less than 20% along the $\langle 1\,1\,1 \rangle$ direction. Assuming 280% total volume expansion at room temperature, the axial expansion was ~17%. The cross section of the fully lithiated *c*-SiNW exhibited a dumb-bell shape. Lee et al. lithiated Si nanopillars of different axial and sidewall orientations [29], as shown in Fig. 8a and b (the first three columns). From the pristine to the fully lithiated states, the cross-sections of the $\langle 1\,0\,0 \rangle$, $\langle 1\,1\,0 \rangle$, and $\langle 1\,1\,1 \rangle$ nanopillars swelled, respectively, into the cross, ellipse, and hexagonal shapes, showing the anisotropic expansion. Goldman et al. [28] fabricated micro-sized arrays of *c*-Si beams on substrates, with exposed $\{1\,1\,1\}$ top surface and two $\{1\,1\,0\}$ sidewalls. Lithiation-induced expansion predominantly occurred along the two sidewalls, but negligibly on the top surface.

Crystallographic orientation-dependent expansion also occurs in lithiated *c*-SiNPs [34]. Through in-situ TEM imaging, Liang et al. observed that the ACI in a partially lithiated *c*-SiNP exhibited a hexagonal shape [34] (see video v4). As lithiation

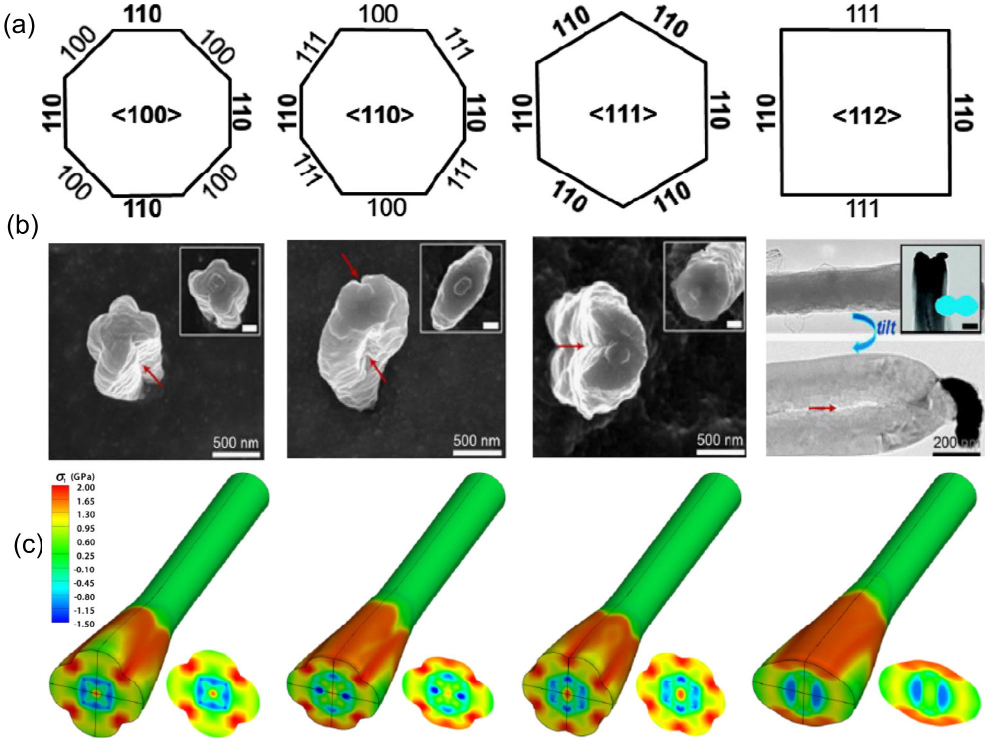

Fig. 9. (a) Lithiation-induced fracture of four c-SiNWs four *c*-SiNWs with different crystallographic orientations. Indices in the center represent the axial orientation, while those on the sides the orientations of the facets. (b) SEM (the first three columns) [32,34] and TEM (the last column) [43] images showing the crack nucleation sites (marked by red arrows) in the lithiated *c*-SiNWs of four different orientations (a). (c) The experimentally observed crack nucleation sites coincide with the stress concentration locations (red spots) predicted by the front-tracking finite element modeling [115].

occurred fastest along the ⟨1 1 0⟩ directions the {1 1 0} facets were the only surviving surfaces. This follows that the ACI is likely constituted of six connected {1 1 0} facets. Owing to the pushing-out effect of newly generated volume at the ACI, the lithiated outer surface also evolved from a circular shape into a hexagonal shape.

In-situ HRTEM study revealed that the anisotropic swelling of lithiated *c*-Si originated from lateral motion of the close-packed {1 1 1} atomic planes during lithiation (see Fig. 8d1 and video v1) [41]. First of all, the large open space between two neighboring {1 1 1} atomic planes constitutes the preferred Li insertion sites. Li insertion enlarges the spacing between the {1 1 1} layers and consequently peels off the {1 1 1} planes. The exposed atomic steps, i.e., the ledges, flow along the (1 1 1) planes, and the Si atoms are gradually dissolved into the amorphous phase, featuring a ledge-mediated solid-state amorphization. MD simulations with the reactive force field reproduce the lithiation mechanism (Fig. 8d2–d3). The ledge flow rate (i.e., the amorphization and lithiation rate) depends on the density of the inclined {1 1 1} facets on the ACI, giving rise to the atomic origin of orientation dependent interfacial mobility and reaction rate. The {1 1 0} ACI consists of high-density inclined {1 1 1} facets, corresponding to the high lithiation rate along the ⟨1 1 0⟩ crystalline directions. In contrast, the low density of the inclined {1 1 1} facets along a {1 1 1} ACI gives rise to a very low lithiation rate along the ⟨1 1 1⟩ directions. *In-situ* HRTEM has showed that the ACI migrates at least one order of magnitude faster along the ⟨1 1 0⟩ directions (several nanometers per minute) than other directions [41]. First-principles simulations have demonstrated that different crystallographic planes of *c*-Si react at different electrochemical potentials, providing additional atomistic mechanism for crystallographic orientation dependent reaction kinetics [135,136].

Front-tracking finite element models have been established to correlate the orientation-dependent reaction rate and the anisotropic swelling of the lithiated *c*-Si. By assigning different reaction rates along different crystallographic orientation at the reaction front, these models aim at reproducing the anisotropic swelling morphologies of lithiated *c*-Si structures. Zhao et al. [117] assumed that lithiation occurs only along the ⟨1 1 0⟩ directions but is negligibly slow in all the other directions, which effectively decouples the Li transport and the stress. The simulated morphologies of the fully lithiated *c*-SiNWs by the model of Zhao et al. agree reasonably well with the experimental data. Yang et al. [80,102,115] assigned different reaction rates analogous to the wet etching rates of *c*-Si, and solved the equations coupling Li diffusion and large elasto-plasticity. To produce a sharp interface, a singular function was used to prescribe the Li concentration dependent interfacial mobility at the reaction front. The cross-sectional morphologies of the fully lithiated state predicted by this model agree strikingly well with the experimental observations (Fig. 8c, in comparison to Fig. 8b, and video 5).

3.1.3. Stress generation and fracture

The orientation-dependent lithiation kinetics in *c*-Si causes not only anisotropic swelling, but also fracture along particular angular sites [32,34,43]. During lithiation, newly created excess volume due to Li insertion generates high compressive stress at the ACI, pushing the lithiated phase behind the moving interface outward [33,34,43,102,115,126]. As a result, large hoop tension is generated at the outer surface of the lithiated shell, presenting the origin of surface fracture of lithiated *c*-Si. More specifically, large incompatible strains are generated at the intersections of adjacent fast moving {1 1 0} facets, leading to stress concentration and consequently fracture nucleation and propagation at dedicated angular sites. In contrast, lithiation of *a*-Si generates uniform tension at the outer surface without stress concentration, suggesting its tough behavior. Fig. 9b shows the experimentally resolved surface cracks in four lithiated *c*-SiNWs [32,43], with the corresponding crystallography shown in Fig. 9a, same as in Fig. 8a. Front-tracking finite element simulations have demonstrated the correlations between anisotropic swelling and crack nucleation sites [102,115] (Fig. 9c). The simulations have also showed that the sharpness of the interface plays a critical role in the stress generation.

Similar anisotropic surface fracture was observed in lithiated *c*-SiNPs. More importantly, in-situ TEM studies showed that the fracture of *c*-SiNPs is size dependent [31,32,34] (see video 4). Large *c*-SiNPs tend to be more fragile than smaller ones under the same lithiation conditions. There exists a critical size of ~150 nm in diameter beyond which surface fracture occurs and below which lithiated *c*-SiNPs remains intact. This size effect arises from size-dependent driving force (i.e., the energy release rate of fracture) [31]. The larger the *c*-SiNPs, the higher the energy release rate. Lee et al. studied the interrelated effects of the size and the lithiation rate on the fracture of ⟨1 1 1⟩ nanopillars [32]. For small (140 nm in diameter) and large (360 and 390 nm in diameter) nanopillars, the size effect was dominant and the fracture ratio was nearly independent of the lithiation rate. Only a few percent of 140 nm nanopillars fractured, and more than 88% of 360 nm and 290 nm nanopillars fractured at all lithiation rates. For intermediately sized nanopillars (240 nm in diameter), the effect of the lithiation rate was significant. The fracture ratios were 13.4, 13.9, and 22.4% when voltage sweep rates were 1, 10 mV/s, and infinity, respectively. Based on 3D simulations, An et al. suggested that the large anisotropic swelling induced fracture can be partially suppressed by cross-sectional shape design of the *c*-SiNWs [118]. However, controlling the cross-sectional shape at the nanometer scale poses challenges in synthesis.

3.2. Lithiation of other group IV elements

3.2.1. Lithiation of c-Ge

Ge has the same crystal structure as Si, i.e. diamond cubic with two interpenetrating face-centered cubic primitive lattices. The capacity of Ge is 1384 mA h g^{-1} when lithiated to the $Li_{15}Ge_4$ phase [137,138]. Though Ge is more expensive than Si, it has a much higher electrical conductivity [139] and Li diffusivity [14,140] than Si, making Ge an excellent candidate for high-power applications.

Lithiation of *c*-Ge at room temperature undergoes a two-step phase transformation: *c*-Ge → *a*-Li_xGe → *c*-$Li_{15}Ge_4$. The crystalline Ge is first converted to the amorphous phase of *a*-Li_xGe ($0 < x < 3.75$) through solid-state amorphization [13,141], followed by crystallization to *c*-$Li_{15}Ge_4$. Possibly due to the fast phase transition and interfacial mobility, a phase boundary that separates Li-rich and Li-poor phases has not been experimentally detected. However, it is commonly accepted that lithiation of *c*-Ge proceeds through a two-phase lithiation mechanism, similar to the lithiation of *c*-Si. Differently, lithiation of *c*-Ge occurs isotropically, in contrast to the orientation dependent anisotropic lithiation of *c*-Si. Density functional theory (DFT) calculations of the interfacial energies of Li on the crystalline facets of Si and Ge have shown that the interaction energy is orientation dependent for Si, but not for Ge [136], providing an explanation for the different lithiation kinetics of *c*-Si and *c*-Ge.

Lithiation induces ~250% volume increase in *c*-Ge [34], consistent with the theoretical volume increase 268% at *c*-$Li_{3.75}Ge$. During delithiation, the *c*-$Li_{15}Ge_4$ is converted to *a*-Ge, similar to the delithiation of lithiated Si. Liang et al. showed that upon lithiation-delithiation cycles, *c*-GeNPs of a wide size range (from 100 nm to nearly 1 μm) remained very tough and survived multiple cycles without fracture [34] (see video v6). Similar to *a*-Si, this tough behavior is likely attributed to the isotropic lithiation, which generates nearly uniform hoop stress at the lithiated shell without highly localized stress.

3.2.2. Lithiation of c-Sn

Tin (Sn) represents another promising candidate as anode, with a theoretical capacity of 994 mA h g^{-1} [142,143], tripling that of graphite. Sn is nontoxic, inexpensive and naturally abundant. Crystalline Sn exists in two phases: α-Sn and *β*-Sn. The *β*-Sn phase exhibits a tetragonal lattice structure, which is metallic, highly ductile and electrically conductive. In contrast, α-Sn exhibits a cubic structure, which is a semiconductor with low conductivity, brittle, and only stable at low temperatures (<13.2°C). Because of its high electrical conductivity and ductility, *β*-Sn is the preferred phase for electrode materials.

In-situ TEM characterization by Wang et al. revealed that lithiation of *c*-*β*-Sn involves a two-step mechanism: *c*-Sn → *a*-Li_xSn → *c*-$Li_{22}Sn_5$ [144]. In the first step, lithiation proceeds by the motion of a sharp two-phase boundary that separates the partially lithiated amorphous phase *a*-Li_xSn and the unlithiated *c*-Sn phase. The phase boundary mobility is insensitive to the crystallographic orientations of crystals, same as in lithiation of *c*-Ge. The first-step lithiation generates a volume expansion of only 55%, indicating the formation of an *a*-LiSn phase. In the second step, further lithiation of the intermediate phase forms a crystalline phase *c*-$Li_{22}Sn_5$, without a visible phase boundary. The total volume expansion is ~239%, close to the theoretical value of 258%.

Li et al. mapped out a different lithiation-induced phase transition pathway for carbon-coated *c*-*β*-Sn [145] (see video v7). Specifically, they observed that lithiation involves a two-step reversible crystalline-crystalline phase transition: *c*-Sn → *c*-Li_2Sn_5 → Li_xSn_y → *c*-$Li_{22}Sn_5$. In the first step, *c*-Sn is transformed into the *c*-Li_2Sn_5 without a visible phase boundary, in contrast to the sharp interface observed by Wang et al. Further lithiation of *c*-Li_2Sn_5 phase forms an intermediate phase Li_xSn_y. This phase, though with a lattice spacing that matches with that of the LiSn phase, could not be unambiguously identified. Further lithiation leads to the formation of the *c*-$Li_{22}Sn_5$ phase. Upon delithiation, the *c*-$Li_{22}Sn_5$ phase is first converted to the *c*-Li_2Sn_5 phase, then to the *c*-Sn phase. The different phase transition pathways may arise from different experimental conditions, i.e., the constraining effect of the coatings, the charging rate, etc.

Lithiation induced pulverization of *c*-Sn is also size-dependent [144]. Nanometer sized *c*-SnNPs (several hundreds of nanometers) remain fairly tough without cracking during lithiation. This tough behavior can be attributed to the isotropic, two-step lithiation and the high ductility of *c*-Sn. For micrometer sized Sn particles, lithiation-induced hoop stress is high enough to drive crack nucleation and propagation, causing fracture [146,147]. Wang et al. observed that during delithiation of a sufficiently large lithiated SnNPs, small SnNPs form and detach from the mother SnNP, a characteristic of delithiation-induced pulverization. During lithiation, small SnNPs tend to agglomerate due to the lithiation induced mass flow and surface welding. Such lithiation-assisted welding has also been observed in SiNWs [148]. Thus, though small SnNPs do not frac-

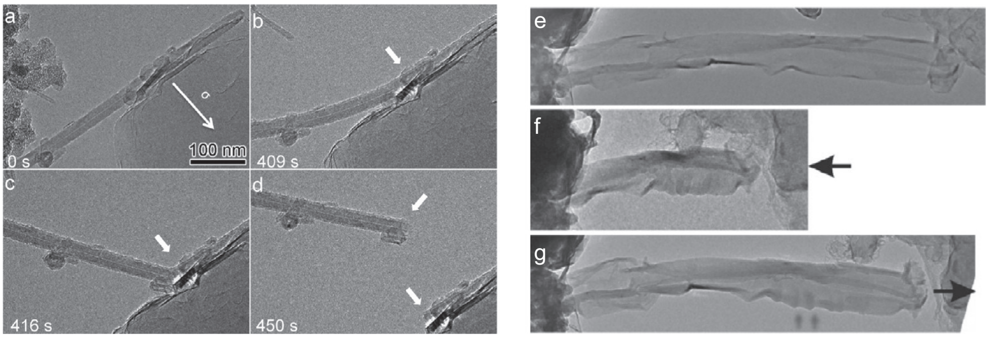

Fig. 10. Comparisons of the mechanical properties of lithiated MWCNTs and GNRs. (a–d) Time-lapse TEM images showing structural evolution and fracture of a lithiated MWCNT under bending [48]. Brittle fracture occurred, manifested by the sharp fracture surface, indicated by the arrows. (e–g) Lithiated GNRs under compression [50]. (e) A lithiated GNR. (f) Upon compression, the GNR was bent and buckled. (g) After the mechanical load is removed the GNR recovers almost entirely its original shape.

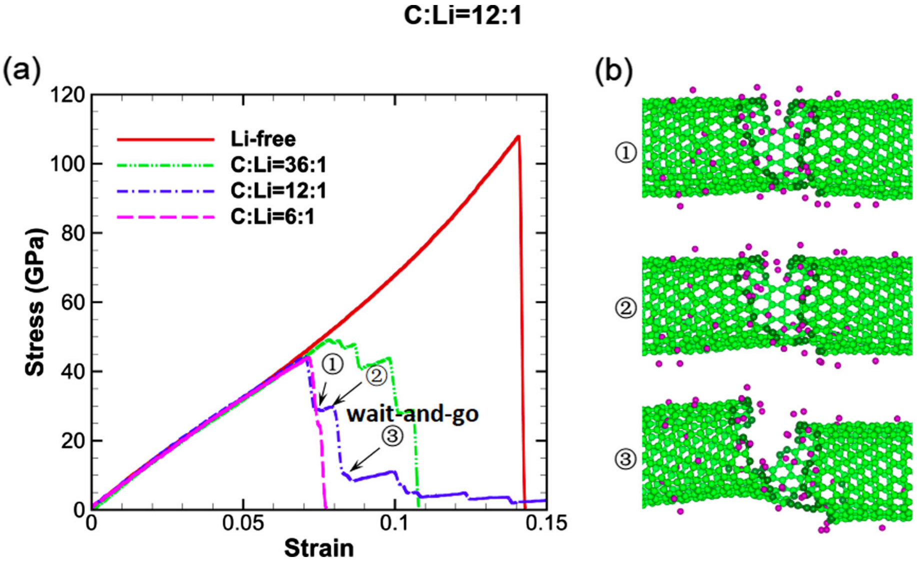

Fig. 11. Li concentration dependent fracture behavior of SWCNTs [159]. (a) Stress-strain curves of SWCNTs with different Li concentrations. For intermediate Li concentrations, the crack propagates in a "wait-and-go" manner. (b) The three representative atomic configurations of the SWNCT (Li: C = 1:12) on the "wait-and-go" fracture path, indicated in (a).

ture during the first lithiation, agglomeration of small NPs leads to the formation large ones, which would pulverize during delithiation or fracture during lithiation in the following cycles [149–152].

3.2.3. Lithiation of carbonaceous materials

Carbonaceous materials of various forms, including amorphous carbon, monolayer and few-layer graphene, graphite (infinitely stacked graphene layers), single-walled and multi-walled carbon nanotubes (SWCNTs/MWCNTs), are known for their excellent mechanical properties and electrical conductivity. Graphitized carbon constitutes the primary component of the anode used in the current LIB technologies. The atomic architecture of the carbonaceous materials dictates the accessible host sites for Li, and hence their specific capacities and power capabilities. The measured capacities are 540–1264 mA h g^{-1} for graphene [153], 450–600 mA h g^{-1} for SWCNTs [154,155], and up to 1000 mA h g^{-1} for MWCNTs [156]; all of which are higher than that of graphite, 372 mA h g^{-1}.

Recent in-situ TEM characterization revealed different chemomechanical failure mechanisms of layered graphene nanoribbons (GNRs) [50] and MWCNTs [48] during electrochemical cycling (see Fig. 10). Li insertion causes interlayer expansion from 0.34 nm to 0.36 nm for both the arc-discharged MWCNTs and GNRs, corresponding to ~6% hoop strain [48] in the MWCNTs and vertical strain in layered GNRs, respectively. Bending of the lithiated MWCNTs using a nanomanipulator revealed that the lithiated MWCNTs are highly embrittled: breakage of the lithiated MWCNTs begins from the nucleation of small sharp cracks from the sidewall of the lithiated MWCNTs [48] (Fig. 10a–d and video v8). The sharp fractured surface suggests a brittle fracture mode, in contrast to the highly bendability of pristine MWCNTs. Similar lithiation-induced embrittlement has also been observed for CVD-prepared MWCNTs, despite that CVD-prepared MWCNTs generally contain more defects that may mediate through-wall Li diffusion and fracture. In distinct contrast, lithiated layered GNRs remain tough, able to recover to their original shapes without fracture upon repeated compression/release cycles by the manipulator [50] (Fig. 10e–g).

The distinct geometries account for the different mechanical responses of lithiated MWCNTs and GNRs. In MWCNTs, due to the radial constraint of the graphene walls, Li intercalation results in significant in-plane stretch of the C—C bonds and radial expansion of the layers. Given that the Young's modulus of graphene is approximately 1TPa, the 6% hoop strain corresponds to 60 GPa hoop stress [157,158]. Considering that the fracture strength of pristine CNTs is ~100 GPa, the geometrical embrittlement effectively accounts for nearly 60% loss in the fracture strength of MWCNTs. For GNRs, free expansion normal to the graphene layers can accommodate Li intercalation induced strain without generating significant in-plane stretch of the C—C bonds and stress. As a result, the graphene layers remain tough upon Li intercalation (see video v9).

Vacancies and atomic holes in graphene and CNTs are generally regarded as defects that degrade the mechanical properties. However, these defects may facilitate Li transport. For pristine graphene layers and open-end MWCNTs, Li intercalation can only occur through the open ends, therefore limiting their charging rate [159–163]. A recent MD simulations have revealed that a sufficiently large vacancy defect may serve as an inlet for Li diffusion, presenting a shortcut for Li penetration into the inner layers [159]. Considering the tradeoff between the mechanical strength and power capability [159], there

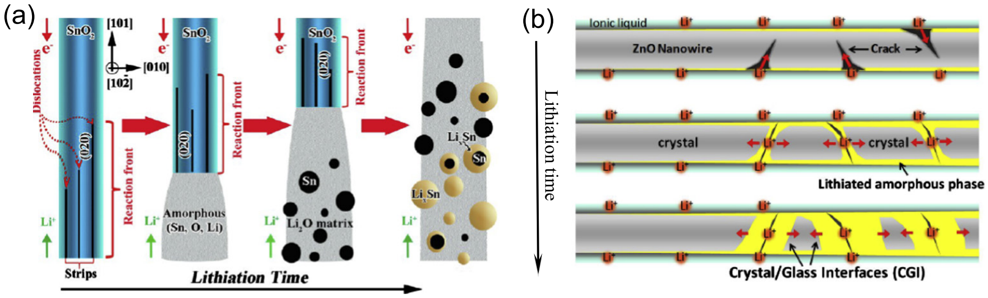

Fig. 12. (a) Schematics of the atomistic lithiation mechanism of the *c*-SnO_2 nanowire, involving long range Li-ion diffusion that generates multiple lithiation strips parallel to the (020) plane (a), followed by the merging of the lithiation strips via solid-state amorphization, nucleation of the Sn particles, and Sn alloying to Li_xSn [164]. (b) Leapfrog surface cracking in *c*-ZnO upon lithiation [165].

exists an optimal vacancy density at which the electrochemical performance is enhanced, while the CNTs still remain mechanically durable.

MD simulations have shown that lithiated CNTs exhibit Li concentration dependent fracture behavior, as shown in Fig. 11 for a SWCNT with hole-like defects [159]. For Li-free (red curve in Fig. 11a) and Li saturated (Li:C = 1:6, purple curve in Fig. 11a) SWCNTs, fracture by uniaxial stretch occurs abruptly, manifesting as a sudden drop of the stress to zero at a fracture strain of 14.06% and 7.15%, respectively. For Li-free SWCNT, brittle fracture is anticipated. For Li-saturated SWCNTs, Li weakens the crack tip spontaneously as crack extends without involving Li diffusion, leading to fast crack propagation. In contrast, crack propagation in the SWCNTs with relatively low Li densities (Li:C = 1:36, green curve; and 1:12, blue curve) involves active Li participation, exhibiting a “wait-and-go” fracture behavior and an increased stretchability, as shown in Fig. 11b. That is, the crack arrests because the applied load is not large enough; further crack extension must wait for Li diffusion into the crack tip, driven by the stress gradient. The “wait-and-go” fracture process significantly increases the stretchability, and correspondingly the fracture toughness.

3.3. Lithiation of oxides

Metal oxides as electrodes for LIBs operate through conversion reactions and generally exhibit much higher energy densities than intercalation materials such as graphite. When exposed to air, metal surface naturally grows a thin oxide layer. Understanding electrochemical performance of the metal oxides is thus important for the design of both oxide and metal electrodes.

Huang et al. have studied electrochemical charging/discharging of single SnO_2 nanowires by constructing a nanobattery consisting of an ionic liquid electrolyte (ILE) and $LiCoO_2$ as the cathode [18]. Upon charging the SnO_2 nanowire undergoes a two-step reaction. First, SnO_2 is reduced to *c*-Sn and amorphous Li_2O: $4Li^+ + SnO_2 + 4e^- = 2Li_2O + Sn$. After this initial phase transformation, reversible reaction occurs in the Sn-ILE-$LiCoO_3$ nanobattery, resulting in the *c*-Li_xSn phase, as discussed previously for lithiation and delithiation of *c*-Sn. Owing to the lithiation induced incompatible strain, the reaction front is highly stressed, which drives nucleation and motion of dislocations, forming a high-density dislocation cloud zone of a chevron-like shape. The formation of the high-density dislocation cloud at the reaction front facilities further Li insertion into the crystal interior on the one hand and the subsequent solid-state amorphization on the other. As lithiation continues, the high-density dislocation zone continuously forms and is absorbed by the moving ACI, reaching a steady-state lithiation process (see video 7).

Lithiation of SnO_2 nanowires generates large volume expansion (~250%). A straight SnO_2 nanowire becomes highly distorted (buckled, coiled, and twisted) after lithiation [18]. The expansion is anisotropic, with much larger axial elongation than the radial expansion (about 2–3 times). Unlike the orientation-dependent reaction rate induced anisotropic swelling in lithiated *c*-Si, the anisotropic expansion in the SnO_2 nanowires has a geometric origin. In particular, the nanowire is axially compliant and thus can accommodate large expansion along the axial direction; whereas the geometrical constraint of the highly stressed ACI confines the expansion along the radial direction, leading to the anisotropic volume expansion. During the lithiation process, the SnO_2 nanowires remains very tough without fracture, despite the fragility of bulk SnO_2.

Using high-angle annular dark field imaging (HAADF) inside an aberration-corrected STEM, Nie et al. further refined the atomic mechanism of lithiation of SnO2 nanowires [164]. They observed that lithiation reaction front propagated by the emission of multiple strips toward the unlithiated crystalline sections, as schematically shown in Fig. 12a. These strips, preferably along the [001] direction and parallel to {200} family planes, were identified as the long-range Li ion diffusion paths inside the SnO_2 lattice. Lattice expands and dislocations appear at the tip of the lithiation strips, which facilitate further Li diffusion toward the SnO_2 lattice. Merging of the lithiation strips is accompanied with solid-state amorphization, nucleation of the Sn particles, and finally alloying Sn particles into Li_xSn.

Similar to the lithiation reaction in the SnO_2 nanowires, electrochemical reaction converts *c*-ZnO nanowires into Li_xZn and Zn nanocrystals that are dispersed in the *a*-Li_2O matrix [165,166]. Different from the nucleation and growth of high-density

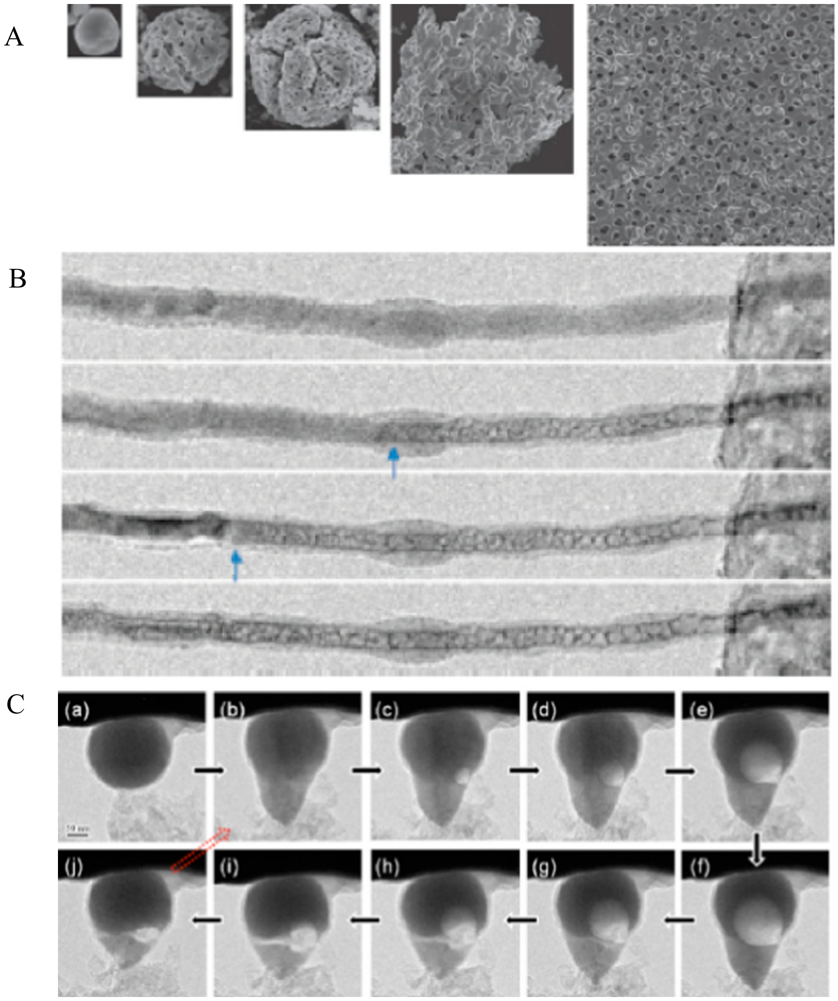

Fig. 13. Formation and evolution of nanoporous structures during delithiation of Li-based systems. (A) SEM images show the size-dependent nanopore formation in Sn [168]. (B) Time-lapse in-situ TEM images of memory nanopore formation and evolution during delithiation of $Li_{3.75}Ge$. The blue arrows indicate the delithiation front [45]. (C) Time-lapse in-situ TEM images of nucleation, growth, and annihilation of a single nanopore in a lithiated GaNPs during delithiation [49].

dislocation zone in lithiating SnO_2 nanowires, lithiation of *c*-ZnO involves discrete hopping of cracks ahead of the reaction front, i.e., leapfrog surface cracking [165] (Fig. 12b and video v10). The surface of the ZnO nanowires is first lithiated, creating large tensile stress near the surface, causing nucleation of surface cracks. Propagation of the surface cracks divides the nanowires into discrete segments. This surface fracture behavior is due to the Li-mediated embrittlement of the ZnO oxide, which is insignificant in SnO_2. The cracked surfaces then function as the fast Li diffusion channels, allowing Li penetration radially into the nanowire and leading to subsequent solid-state amorphization. The lithiated amorphous segments grow separately and eventually meet and adhere to each other, forming an amorphous-amorphous interface. This process repeats until the ZnO nanowire is fully lithiated. This process appears to be size dependent. For ZnO nanowires with large diameters, subdivision occurs after segmental divisions; whereas such subdivision is less frequently seen in thin nanowires.

Su et al. [167] performed in-situ TEM study on the lithiation-delithiation cycling of iron oxides (Fe_2O_3) nanocrystals deposited on graphene. The Fe_2O_3 nanoparticles undergo ~80% volume expansion upon lithiation, but remain intact without fracture. Lithiation transforms the single crystal Fe_2O_3 nanoparticles to multi-crystalline nanoparticles consisting of many Fe nanograins embedded in the *a*-Li_2O matrix. Delithiation in the first cycle forms FeO rather than Fe_2O_3, with some remaining Li_2O, which accounts for the irreversible electrochemical conversion and large capacity fading.

3.4. Delithiation-induced nanopore formation

Phase transition and morphological evolution during delithiation are equally important to those in lithiation since they directly influence capacity retention and cycling performance of the electrodes. A series of recent SEM/TEM experimental studies of Li-based alloys have demonstrated that formation and evolution of porous sponge is a ubiquitous phenomenon during delithiation (see Fig. 13) [45,49,168]. Such a phenomenon has been intensively studied in noble-metal systems such as Cu-Au and Ag-Au upon dealloying [169,170]. Experimental studies have also suggested that formation and evolution of the porous structures depend on a set of materials and structural properties (e.g., bonding types of materials, flow stress, composition, size, and geometry), and electro-chemo-mechanical parameters (e.g., delithiation rate).

Several competing kinetic processes are involved during delithiation: Li dissolution from the alloy, diffusion of vacancies, and surface diffusion of Li. In the case of vacancy-mediated lattice diffusion as the primary delithiation process, extraction of Li will roughen the surface of the alloy. Continuing delithiation would form negative or void dendrite form of porosity [171], producing atomic scale channels. These channels provide pathways for the electrolyte to invade the alloys for continuing dissolution in the case of liquid electrolyte. This process is widely known as percolation dissolution [172], which results in a self-organized solid/pore bicontinuous nanostructures [168,170,173,174]. For solid electrolytes, the channels are fast Li diffusion pathways out of the alloys during delithiation. Interfacial surface smoothening may lead to smaller pores and enlarges the ligaments. Further, similar to Ostwald ripening where nanoparticles agglomerate to minimize surface energy, pores may also merge together to form bigger ones driven by the reduction of surface energy. Finally, Kirkendall effect may also operate in these systems to hollow the nanostructures.

Delithiation-induced porous morphologies are dependent on the structural size. There may exist a critical size below which the nanoporous morphologies structure does not evolve, due to the fast surface diffusion of the active materials that acts to smoothening the incipient evolving nanoporous structures. The threshold particle diameter may also be material-type dependent. Chen and Sieradzki [168] found that in dealloying Li_xSn particles, the ligament size in the delithiated product increases with the size of Sn particles (Fig. 13A). For a 2 μm sized Sn particle, the ligament size is about 100 nm; whereas for Sn particle size less than 300 nm the porous morphologies do not evolve.

It has been pointed out that in noble-metal alloy systems there exists a threshold compositional ratio, known as the parting limit, below which selective dissolution does not occur and above which there is a compositionally dependent critical potential required for dealloying [175]. For alloys with suitable compositional ratio and assuming dissolution is the rate-limiting step, the percolation mechanism operates and predicts a self-organized solid/pore bicontinuous nanostructures. Below the threshold compositional ratio, the active paths for the electrolyte or Li no longer exist, dealloying of Li can only proceed by a process involving the mass transport of Li from the interior of the alloy to the electrolyte. A dealloyed morphology with such a mechanism may consist of negative tree-like structures or "void-dendrites" penetrating into the solid [170].

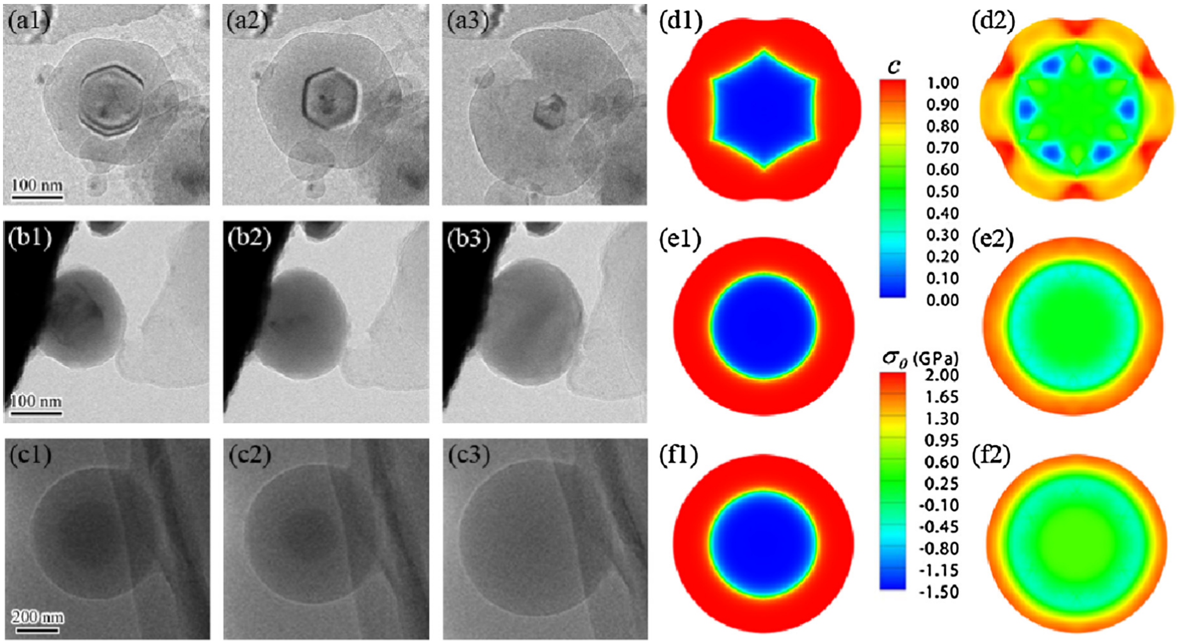

Fig. 14. Lithiation-induced anisotropic swelling and fracture in a *c*-SiNP versus the isotropic swelling without fracture in a *c*-GeNP and an *a*-SiNP. The original sizes of the *c*-SiNP and *c*-GeNP are both about 160 nm, and the *a*-SiNP is about 540 nm. (a1–a3) TEM image sequence showing the anisotropic swelling and subsequent fracture of a lithiated *c*-SiNP [34]. The round *c*-SiNP becomes hexagonal in shape for both the outer surface and inner unlithiated core. (d1–d2) Chemo-mechanical modeling of the core-shell structure and stress generation in the cross section of a lithiated *c*-SiNW, mimicking the stress generation inside the *c*-SiNP [80]. The red color at the outer surface indicates tensile stress, while the blue color indicates compressive stress. (b1–b3) TEM image sequence shows the isotropic swelling and tough behavior of *c*-GeNP [34]. (e1 and e2) Chemo-mechanical modeling of the uniform stress generation in the cross section of a lithiated amorphous *c*-GeNW [80]. (c1–c3) TEM image sequence shows the isotropic swelling and tough behavior of *a*-SiNP [134]. (f1 and f2) Chemo-mechanical modeling of the uniform stress generation in the cross section of a lithiated *a*-SiNW [80].

Liu et al. [45] have observed that during repeated lithiation and delithiation of GeNWs the pore size and spatial distribution hardly change over cycles, exhibiting a memory pore effect (Fig. 13B and video v11). However, such porous structures were absent in same-size GeNPs (about 200 nm in diameter). This indicates that geometry plays a certain role in the pore evolution, though this role remains to be explored. Liang et al. [49] found that upon delithiation of Li-alloyed GaNPs, a single nanovoid formed due to the high diffusivity of Ga at room temperature (Fig. 13C and video v12). The nanovoid disappeared within a time scale of seconds, driven by curvature-dependent chemical potential difference of Ga atoms from the outer to the inner surfaces. TEM imaging by Choi et al. [176] showed that the pore size in both SiNWs and ZnO nanorods increases with increasing number of lithiation/delithiation cycles, while the pore size in AgNWs decreased. Differently, the pore size in SiNWs increases gradually, while that in ZnO nanorods increases in a stepwise manner.

4. Stress-kinetics coupling in electrochemical lithiation

Electrochemical lithiation involves long-range electron and ion transport, charge-transfer reaction where the solvated Lithium ion breaks its solvation shell and simultaneously captures an electron from conductive agent and insert into the electrode, and atomic (or ion + polaron) diffusion into electrode materials. The whole lithiation process features strong coupling between transport kinetics and mechanical stress generation, particularly for high-capacity electrode materials such as Si and Ge. Such kinetics-stress coupling is bidirectional: Li insertion kinetics (e.g., rate and rate anisotropy) mediates stress generation, defect nucleation and degradation of the electrode materials; reciprocally, the generated stress regulates lithiation kinetics [33,40,99,120].

The high mechanical stress not only causes chemomechanical degradation of the high-capacity electrodes, but also influences the voltage profile and the power capability of the batteries [84]. During lithiation, the compressive stress generated in the anode materials increases the chemical potential of Li, corresponding to a lower battery voltage. During delithiation, the anode material undergoes tensile stress that decreases the chemical potential of Li, giving rise to a higher battery voltage. The different stress states during electrochemical lithiation/delithiation cycling thus generate voltage hysteresis. Considering the GPa level mechanical stress generated in the lithiation/delithiation cycles, the voltage hysteresis in the high-capacity anode materials is very strong, leading to low energy efficiency.

4.1. Lithiation kinetics modulates morphological evolution, stress generation, and fracture

Several comparative studies manifest the role of lithiation kinetics on the mechanical stress generation and fracture in electrode materials. In a comparative study, Liang et al. have shown that single *c*-SiNPs upon lithiation undergoes anisotropic swelling (Fig. 14a1–a3, ~300% volume expansion, and video v4) due to the crystallographic orientation dependent anisotropic lithiation rates [43]. The anisotropic swelling results in high stress concentration at the outer surface along well-defined angular sites, and consequently surface fracture (Fig. 14a2–a3, d1–d2), [31,34]), which is dependent on the original size of the SiNPs. In contrast, lithiation of *c*-GeNPs causes isotropic swelling (Fig. 14b1–b3, ~260% volume expansion, and video v6) and uniform hoop stress in the outer surface (Fig. 14e1 and e2). This explains that *c*-GeNPs appear to be much more fracture resistant than the *c*-SiNPs during lithiation [34]. Similar to the lithiation behavior of *c*-GeNPs, *a*-Si structures are very tough upon full lithiation, even for micro-sized pillars (Fig. 14c1–c3) [32,44,177]. Owing to the isotropic swelling, lithiation of *a*-Si structures generates uniform hoop stress in the outer surface (Fig. 14f1 and f2), distinctly different from that in *c*-Si. In addition, the two-step lithiation mechanism [44,134,178] alleviates the stress generated in lithiated *a*-Si structures. In the first-step lithiation in which sharp interface presents, the newly produced excessive volume at the ACI is not as much as in *c*-Si, corresponding to a lower compressive stress at the interface. The stress generated at the outer surface in the second-step lithiation is also relatively low because of the single-phase lithiation. These factors account for the tough behavior of *a*-Si

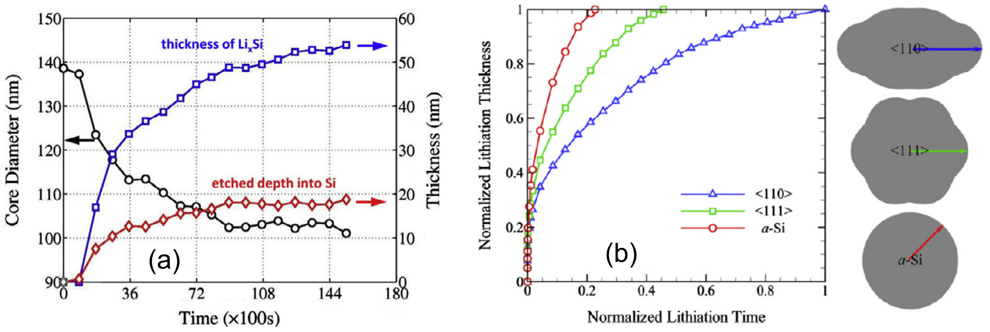

Fig. 15. Lithiation retardation in Si. (a) Plots of etched depth (red), diameter of the unlithiated core (black), and the thickness of the lithiated shell (blue) versus time, demonstrating stress mediated lithiation retardation [40]. (b) The lithiation-retardation effect is stronger with stronger lithiation anisotropy [80]. Lithiation dynamics is measured along ⟨1 1 0⟩ directions for the *c*-SiNWs and an arbitrary direction for the *a*-SiNW.

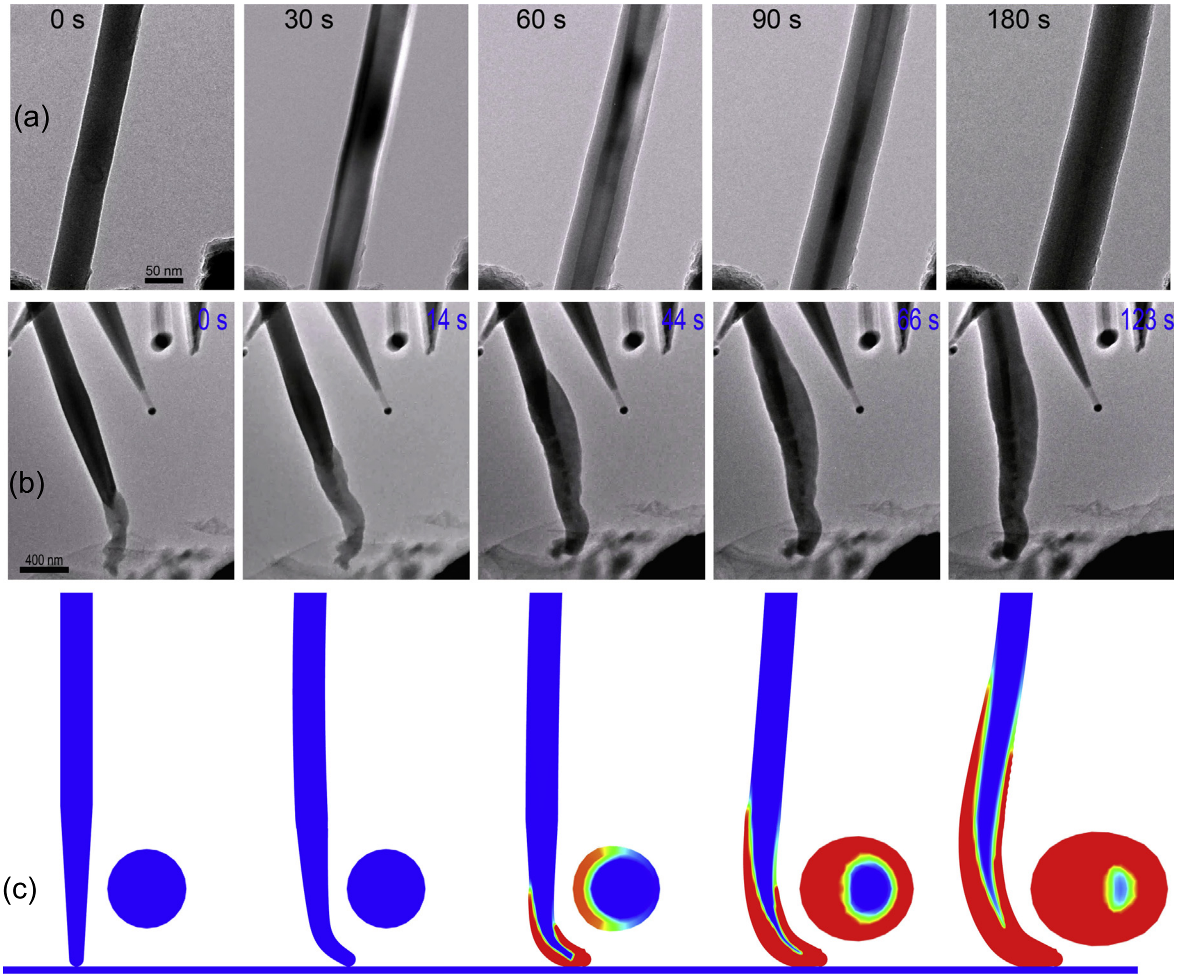

Fig. 16. External bending force breaks lithiation symmetry in *c*-GeNWs [47]. (a) Uniform lithiation along the axial direction of a free-standing *c*-GeNW, manifested by the uniform lithiated thickness along both axial and radial directions. (b) Symmetry breaking of lithiation in a *c*-GeNW with applied bending force. A comparison of the lithiated thickness showed that lithiation proceeds appreciably faster along the tensile side than the compressive side. (c) Chemomechanical modeling of the symmetry breaking in a bent c-GeNW [47]. Symmetry breaking occurs both in the longitudinal and radial directions of the nanowire. Blue: unlithiated region; red: lithiated region; transition color: ACI.

during lithiation. The correlation between lithiation anisotropy and fracture behavior clearly demonstrates that not only insertion capacity but also insertion kinetics influences stress generation in the electrodes.

4.2. Mechanical stress modulates lithiation kinetics

To elucidate the role of mechanical stress on the lithiation kinetics, Liu et al. have shown that in *c*-Si lithiation slows down as lithiation progresses [40], as shown in Fig. 15a. Similar lithiation retardation behavior has been observed by McDowell et al. [33]. Computational simulations have revealed that the lithiated shell and the sharp interface undergo increasingly high hydrostatic compression as lithiation proceeds [40,43,80,102,115], which subsequently slows down both Li diffusion in the lithiated shell and chemical reaction rate at the interface, explaining the lithiation retardation observed in the experiments. For nano-sized structures lithiation retardation is mainly due to the reduced chemical reaction rate since reaction is the rate-limiting event. In the extreme cases, the stress-mediated lithiation retardation effect can completely arrest lithiation.

Lithiation anisotropy influences the distribution and level of stress generated near the ACI, which in turn yields different levels of retardation effect [80]. Fig. 15b plots lithiation rates in three different SiNWs (*a*-SiNW, ⟨1 1 1⟩ *c*-SiNW, and ⟨1 1 0⟩ *c*-SiNW) along specified directions (⟨1 1 0⟩ direction for the *c*-SiNWs and an arbitrary direction for the *a*-SiNW). These simulations show that the strength of the retardation effect correlates with the level of lithiation anisotropy (⟨1 1 0⟩ *c*-SiNW > ⟨1 1 1⟩ *c*-SiNW > *a*-SiNW).

McDowell et al. [33] has pointed out that stress-mediated lithiation kinetics is nearly independent of the SiNP size under lithiation. This conclusion seems to be consistent with the stress analysis by Zhao et al. [117], where the stress at the sharp interface is only a function of the ratio of the radius of the unlithiated core and the original radius of the SiNP. However, one notices that the stress analysis is performed under the assumption of mathematically sharp interface (zero-width interface). In reality, the finite-width (~1 nm) interface is regarded as an intrinsic microstructure, which suggests size effect on stress generation and hence lithiation retardation. It can be conceived that such size effect could be considerably strong when the radius of the unlithiated core is on the same order of the width of the interface.

Similar to the self-generated stress in lithiated Ge and Si, externally applied load may modulate lithiation kinetics. In a recent study Gu et al. have compared the lithiation kinetics of free-standing and bent GeNWs [47]. For free-standing GeNWs, lithiation proceeds isotropically along both the axial and radial directions, displaying a uniform unlithiated crystalline core - lithiated amorphous shell structure (Fig. 16a). Lithiation-induced compressive stress at the ACI retards further lithiation, similar as in *c*-Si. In another set of experiments, the GeNWs are pushed against the Li metal (as the counter electrode in the nanobattery platform for in-situ TEM imaging) while being lithiated. The pushing force effectively bends the GeNWs, generating a curved region with an asymmetric stress profile. The tensile side enhances Li diffusion and reaction, while the compressive suppresses them, resulting asymmetric lithiation at the bent region (see video v13). Fig. 16b shows the bending induced symmetry breaking of lithiation in GeNWs. At the bent region, the cross-sectional morphology was highly asymmetric, with a lithiated shell thickness in the tensile side of 194 nm and in the compressive side of 80 nm, clearly demonstrating bending-induced symmetry breaking of lithiation. Front-tracking simulations further show that the symmetry-breaking of lithiation morphologies occurs along both the longitudinal and radial directions [47] (Fig. 16c and video v14).

The stress-kinetics coupling leads to a novel concept of "mechanically rechargeable" "bend-to-power" LIBs and electrochemically driven mechanical energy harvesters [87], made of layered thin films: two highly flexible layers as the electrodes sandwiching a central layer as the electrolyte. Bending the thin film structure creates a difference in the chemical potential of Li on the tensile and compressive sides, driving the Li flow from the compressive side to the tensile side. That is, bending converts the mechanical energy to the chemical/electrical energy, thereby charging the battery. Discharging occurs either through partially elastic recovering of the thin film structure or by reverse bending to power the external load. The battery can be cyclically charged by repeated bending, featuring a mechanical energy harvester. Following this concept, Kim et al. fabricated a prototype of a mechanical energy harvester (see video v15). The device can generate tens of mV open-circuit voltage, tens of $\mu A/cm^{-2}$ short-circuit current, and sustain thousands of mechanical bending cycles without apparent degradation. The energy harvester is most efficient when harvesting low-frequency motions such as human walking.

5. Mitigation of electro-chemo-mechanical failure

Recent studies have provided novel insights for mitigating the electrochemically induced chemomechanical degradation of the electrodes, ranging from nanostructuring, nanoporosity, surface coating, nanocompositing, self-healing agents, and flexible structures, etc. Each of these design strategies can lead to better capacity retention and longer cycle life of the LIBs, as discussed below.

5.1. Nanostructuring

Early studies considered fracture and pulverization as the primary reasons for the rapid capacity loss and low cycle life of the high-capacity electrode materials. Considerable efforts have accordingly been undertaken to design the materials on the structural level so as to mitigate electrode cracking. In light of the size-dependent fracture behavior, one obvious route is to use nanoscale materials as the anode. Cui's group pioneered the work in nanostructured Si anodes [16]. Owing to the large surface-to-volume ratio, nanostructured materials can facilitate strain relaxation and enhance flaw tolerance, and hence become mechanically tougher than their bulk counterparts. In addition, the shortened Li^+/polaron diffusion paths and increased surface area of the electrodes in contact with electrolyte [15,30,179] give rise to better rate performance. Studies on the various nanostructured materials with different geometric shapes, including nanowires [16,32,42,45,180], nanoparticles [34,181–184], and thin films [12,185–188] have demonstrated that the electrochemical performance of these nanostructured materials greatly exceed their bulk counterparts, clearly showing the advantages of nanoscale materials.

Inspired by the superior cyclability of graphite, other layered two-dimensional (2D) crystals [189], such as transition-metal dichalcogenides (TMDs) [190] and MXenes [191] have attracted much attention for energy storage applications. Due to their flexibility, large surface-to-mass ratio, and unique layered morphology, these 2D layered crystals can accommodate various ions and molecules by interlayer intercalation, making them promising electrodes for LIBs. The intercalation capacity and mobility depend on the interlayer spacing. It was reported that restacked MoS_2 layers give rise to a higher specific capacity (~750 mA h g^{-1}) for Li intercalation than the as-prepared layers since the restacked layers has larger interlayer spacing [192]. MXenes are good electrical conductors. Xie et al. revealed that Li-storage capacities depend on the surface functional groups of MXenes [193]. Oxygen-terminated MXenes exhibit the highest theoretical Li storage because they can adsorb two Li atomic layers on both sides of the crystal layer. Compared to the materials currently used in LIBs and NIBs, MXenes hold great promise in enhancing the overall performance.

Though scaling down the materials to nanometer size can mitigate the fracture of the electrode material itself, volume changes can still cause delamination of the active materials from the current collectors as well as unstable SEI formation, which are exacerbated by the large surface area to volume ratio when the electrode works at voltages outside of the electrochemical stability window of the electrolyte. These issues have remained critical to limiting the cycle life of the battery. In addition, fabrication of these nanostructured materials usually requires chemical vapor deposition or template growth, which is difficult and costly to scale up, thus reducing the viability of these nanostructured materials for commercial applications. Also, even though the reported gravimetric capacity of nanomaterials are generally impressive (e.g. >1000 mA g/h, 3 × that of graphite), they tend to have quite low tap density or pellet density (e.g. 0.5 g/cm^3, which is much less than the 1.6 g/cm^3 of porous graphite), such that the volumetric capacity may be less impressive when compare to graphite. The low tap density problem is fundamentally attributable to the size and shape dispersions of nanoparticles, since well-engineering nanoparticle assembly can have exceptionally high packing density [194,195]. This is why further engineering the nanostructures, for example promoting grain or phase boundaries rather than free surfaces[63], could be fruitful directions of research.

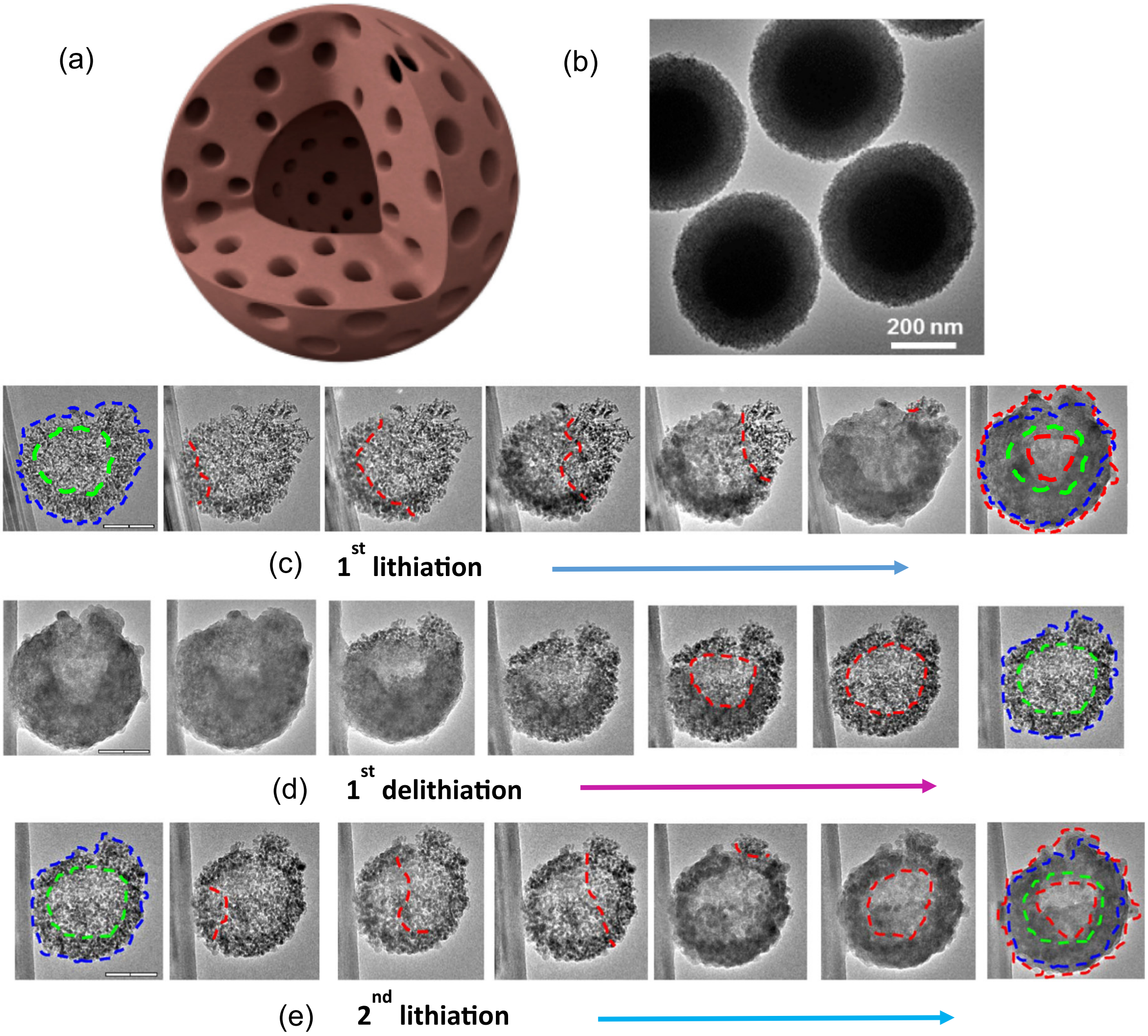

Fig. 17. Inward Li breathing of hierarchically porous SiNPs [53]. (a) Schematics of the hp-SiNP. (b) A high-resolution TEM image of the hp-SiNPs. (c) Time-lapse TEM images of the first lithiation of a hp-SiNP (length bar: 200 nm). (d) Time-lapse TEM images of the delithiation process show that the lithiated hp-SiNP returns nearly to its original size (both inner and outer radii), demonstrating its high reversibility upon electrochemical cycling. (e) Time-lapse TEM images of the second lithiation process show the reversibility of the morphological changes during cycling. Blue and green dashed lines are the outer and inner surface profiles of the hp-SiNP prior to lithiation, and the red dashed lines mark the lithiation and delithiation front.

5.2. Nanoporosity

Nanostructured porous materials [53,196–219] can provide interconnected and fast interfacial transport, shortened diffusion path, and hence enhanced rate performance. The internal pores (may either be open or closed) can accommodate volume changes and alleviate mechanical stress generation during lithiation/delithiation cycles, thereby improving the structural stability and durability. Porous assemblies can be formulated by loosely packing NPs or NWs. However, pores or empty spaces in such NP or NW assemblies are generally unorganized, which causes unevenly distributed stress and strain in the aggregates upon lithiation. Mechanical stress in densely packed regions might still be high enough to cause fracture, leading to rapid capacity fading. Additionally, owing to the non-uniform pore distribution, the fast lithium diffusion path may be blocked by lithiation induced volume expansion, thereby deteriorating the rate performance. For these reasons, porous assemblies and structures with spatially ordered pores are most desired. Cho et al. [199] synthesized mesoporous SiNWs with uniformly and regularly distributed pores. The uniform pore pattern ensures even accessibility of the electrode surface to the electrolyte and uniform volume change and stress generation of the electrode material during cycling. The thin walls of the SiNWs (~6.5 nm) also provide shorter diffusion paths for lithium ions into the NWs, leading to uniform high-rate charging and discharging throughout the materials. The mesoporous SiNWs exhibit much better electrochemical performance, including higher initial charge capacity, higher Coulombic efficiency, and better capacity retention, than randomly packed SiNPs and SiNWs. Using a simple thermal annealing method, Kim et al. [197] fabricated 3D porous Si with well-ordered pore pattern. Electrochemical testing found that the 3D porous Si preserves its original morphology during cycling without pulverization after 100 cycles. This 3D porous Si maintains a charge capacity of greater than 2800 mA h g^{-1} at a rate of 2000 mA h g^{-1}. Many other porous Si (e.g., periodic porous thin film by Cheng et al. [211]) with ordered pore patterns have been fabricated and proven to possess improved electrochemical performance as compared to unorganized Si assemblies.

While these nanoporous assemblies preserve rooms for volume expansion, the building blocks of the assemblies upon lithiation still expand, causing facture, lithiation retardation, and unstable SEI growth. To minimize the volume expansion on the level of individual building blocks, various porous nanostructures have been fabricated and assessed. Park et al. [220] have synthesized SiNTs with an outer diameter of ~200–250 nm and wall thickness of ~40 nm. The tubular morphology provides extra free surface for dislocation absorption, stress relaxation and fast lithium flow channels. Li-ion full cells using the SiNT assemblies as the anode and $LiCoO_2$ as the cathode exhibit a capacity one order of magnitude higher than commercial graphite anode even after 200 cycles. HRTEM images have showed that the tubular morphology of the SiNTs retains without fracture after multiple cycles. Ge et al. [205] synthesized Boron-doped porous SiNWs with the pore size of ~8 nm. The doping increases the electrical conductivity. The pores enable uniform accessibility of the electrolyte of each individual SiNW, improving both the mechanical durability and electrochemical charge-discharge rate. TEM images have showed that the porous morphology (the size and the pattern) retains after cycling. Nanoporous SiNPs fabricated by Ge et al. [213] through ball-milling and inexpensive stain-etching exhibit similarly high reversible capacity, high charging rate and capacity retention, and long cycle life.

These uniformly porous materials still exhibit considerable degree of capacity fading over cycles, primarily due the unstable SEI growth at the Si-electrolyte interface upon repeated outward volume expansion/shrinkage. Even for SiNTs, their outer radius still undergoes large expansion and shrinkage during the cycling, depending on the ratio of the inner and outer radii of the SiNTs. Xiao et al. [53] fabricated hierarchically porous SiNPs (hp-SiNPs), with a hollow core (primary pore) of 300 nm and a porous shell of 75 nm thick. The pore size in the porous shell is only a few nanometers (Fig. 17a and b). In-situ TEM studies revealed that the outward volume change in the hp-SiNPs upon lithiation-delithiation cycles is completely suppressed, in distinct contrast to the solid nonporous and other porous SiNPs and SiNWs [29,34,43,44,177], as illustrated in Fig. 17c and d. During lithiation, owing to much smaller stiffness and flow stress of the unlithiated inner layer than the lithiated shell, the compressive stress generated at the reaction front pushes more inward than outward, resulting negligible outward expansion (Fig. 17c and e, and video v16). During delithiation, the generated tensile stress at the reaction front pulls the inner layer outward (Fig. 17d, and video v17). This deformation mode leads to inward Li breathing of the hp-SiNPs during lithiation/delithiation cycles, with negligible exterior volume expansion, i.e., the apparent size of the hp-SiNPs remains nearly unchanged. This helps stabilize the SEI and maintain material/structural stability. The electrochemical performance exceeds even the commercially available Si-based anodes. Other hierarchical porous structures have been assessed as anode materials [208]. Overall these hp-porous materials showed stable high capacities (e.g., ~1250 mA h g^{-1} for 600 cycles for GeO_x; 1500 mA h g^{-1} for 50 cycles). These hierarchically porous structures maximally preserve the morphologies of the particle aggregates, preventing the changes in the microscopic charge transport pathways and relieving the stress generation in the electrode materials.

5.3. Surface coating

Surface coating represents another powerful approach for improving capacity retention and cyclability of high-capacity electrodes. Surface coatings generally may act as a chemical barrier and mechanical constraining layer that buffers volumetric change during electrochemical cycling, thus helping maintain good electrical contact of the components and preventing cracking and pulverization of high-capacity electrodes. Many coating materials also function as a passivation layer that can suppress unwanted reactions between electrodes and electrolytes such as leaching of elements from inside electrode to outside, or HF attack. Electronically conductive coatings such as carbon, metal, and conductive polymers can enhance the redox reaction kinetics and improve the current collection efficiency. Surface coatings can also prevent electrochemical welding between particles of active materials. All these attributes improve the electrochemical performance of surface-coated electrodes.

Carbonaceous materials have been used as the coating layers for their high mechanical strength and high electrical conductivity [197,221–230]. In-situ TEM characterizations of conformally carbon-coated SiNWs have shown that the presence of the carbon skin coatings speeds up the lithiation rate by nearly one order of magnitude [221]. For complete and uniform coatings, the SiNWs can only be partially lithiated, leaving an unlithiated *c*-Si core in the SiNWs. This phenomenon arises from coating-mediated lithiation retardation. Owing to the confinement effect of the coatings, the volume-expansion induced compressive stress in the coated Si upon lithiation is much higher than that in the bare Si structures, which renders stronger lithiation retardation and may completely arrest further lithiation. Such coating-mediated lithiation arrestment has been observed in carbon-coated SiNPs [223], where the innermost part of the coated SiNPs is electrochemically inaccessible. Upon repeated cycling, the coating may fracture, relieving the compressive stress and allowing the core to be fully lithiated. Li et al. [226] have fabricated *c*-SnO_2 nanowires (50–60 nm in diameter) coated with 10 nm-thick amorphous carbon. During lithiation, the carbon coating deforms conformably with the lithiated SnO_2 core without interfacial delamination. Ring cracks along the hoop direction develop near the lithiation front, where the coating is bent due to the diameter transition between the lithiated and pristine segments. The fracture behavior is found to be coating-thickness dependent. Thinner coatings are more prone to fracture than thicker ones during lithiation since the stress generated in thinner coatings is lower for the same diameter of the crystalline core. Similar thickness-dependent degradation behavior has been observed in *c*-GeNWs-CNFs [227], where high carbon content and uniform carbon coating in *c*-GeNWs-CNFs critically improve the electrochemical performance.

Metals are both mechanically ductile and electrically conductive, and thus popular as coating materials for high-capacity electrode materials for improved structural stability and rate performance [231,232]. Some metals, such as Sn, are particularly attractive because their high capacity contributes to the overall capacity of the anode[232]. Sandu et al. [231] have found that the lithiation morphology and fracture pattern of Ni-coated *c*-Si nanopillars depend on the coating thickness and the nanopillar diameter. Si nanopillars with relatively thin coating still swell in an anisotropic manner, similar to bare Si nanopillars. However, even a thin coating changes the preferred fracture sites. Thick coatings modify anisotropic swelling to be isotropic with one randomly oriented longitudinal crack. Kohandehghan et al. [232] have found that with 3 nm Sn coating the cycling performance of the SiNWs improve significantly. During lithiation, the lithiated shell (Li_xSn) confines radial expansion of the Si core in favor of longitudinal expansion. This swelling mode improves the structural stability and helps stabilize SEI growth.

Surface coatings using metal oxides offer not only high mechanical strength, but also high thermal stability and high Li diffusivity. It has been shown that Si anodes coated with a SiO_x native layer can sustain more than 6000 cycles with little capacity fade. Al_2O_3 surface layers grown on AlNWs can survive 100% volumetric strain with exceptional mechanical robustness. TiO_2 encapsulated sulfur cathodes have demonstrated unprecedented cyclability over 1000 cycles. The technique of functional surface coating using oxides opens up additional pathways for the realization of high-capacity electrodes with sustainable reliability.

Crystalline Si features a native amorphous oxide layer of ~2 nm thick, which is very stiff and electron-insulating. The native oxide layer transforms to Li_2O upon lithiation [233], which is Li ion conducting but electron insulating. For these reasons, Li_2O can function as a solid electrolyte in the half-cell nanobattery for in-situ TEM study. Interestingly, He et al. [233] have observed that the Li_2O phase does not form continuous film but rather discrete and random oriented crystalline islands. The spacing between the crystalline islands forms conductive routes for electrons. He et al. [233] have further observed that the SiNPs were not fully lithiated, but only to an *a*-Li_xSi phase ($x = 2.3$), possibly due to the combined electrical retarding effect of the Li_2O layer and the mechanical confinement effect of the coating layer.

Zhang et al. [234] have synthesized high-quality SiC nanowires coated with 2–10 nm thick native SiO_2 layer. Since SiC is inactive to lithiation, observations have been focused on the electrochemical behavior of the thin SiO_2 layer. Their in-situ TEM studies have confirmed that crystalline Li_2O was formed at the early stage of lithiation. Further reduction reaction produces a mixture of Li-Si-O glass with Li_4SiO_4 and Li_2O crystals in the thin SiO_2 layer. The electrochemical growth of the SiO_2 layer during lithiation and delithiation cycles is highly inhomogeneous. The thin SiO_2 coating grows to a wavy morphology, possibly due to the stress-regulated lithiation reactions. The lithiated phase of convex curvature develops tensile stresses, facilitating lithium transport through the lithiated material and promoting the interfacial reaction at the phase boundary. On the contrary, the lithiated phase of concave curvature is compressively stressed, retarding the electrochemical growth of the SiO_2 layer. Through the experimental characterizations and first-principles modeling, it has been observed that the electronic conduction of SiO_2 is significantly improved upon lithiation. Li diffusivity, however, decreases upon the formation of lithium silicates during lithiation and may impede battery cells from fast cycling. These implicates that an optimum design of the geometry and thickness of SiO_2 passivation layer should consider the concurrent effects of lithiation on the electronic conduction and ionic transport.

Al_2O_3 coating by atomic layer deposition (ALD) can act as an artificial SEI layer that may improve the cycle stability, prevent side reactions, suppress electrode decomposition, and facilitate charge transfer at Si electrode surface. With 5–10 atomic layers of an alumina ALD coating, Li et al. [235] have demonstrated that thin-film Si electrode can deliver a 2600 mA h g^{-1} capacity within 24 s. Ye et al. [236] have compared lithiation kinetics and failure mechanisms of ALD coated (Al_2O_3 and TiO_2) Si micropillars with bare Si micropillars. Their in-situ TEM analysis found that the ALD coatings help stabilize thin SEI layers of less than 15 nm thick. In comparison, SEI thickness for bare Si micropillars is up to ∼0.5–0.8 μm. Lithiation kinetics and consequently the swelling anisotropy upon lithiation of the bare Si nanopillars appear to be regulated by the formed thick SEI layer, but no longer by the phase boundary mobility. Indeed, bare Si micropillars appear to be lithiated more uniformly, and fracture initiates randomly along all the directions. In contrast, coated Si nanopillars swell anisotropically and crack initiates along preferred orientations (circular for ⟨1 1 0⟩ and square for ⟨1 0 0⟩ directions). Coating also enhances structural stability as the fracture occurs at a larger volume expansion in coated micropillars than bare ones consistently. Li et al. [237] have further demonstrated that there exists an optimal thickness of ALD Al_2O_3 coatings at which the cycling performance maximizes for Si/C composite nanofibers.

Other metal oxides have been tested. Zhu et al. [238] have studied the electrochemical performance of SiNPs with ALD zincoxide (ZnO). Lithiation of the coating proceeds via sequential conversion and alloying reactions, forming a LiO_2/Zn layer on the SiNPs. This layer significantly improves electrochemical performance owing to the enhanced mechanical integrity and stabilizes SEI despite of large volume expansion of the Si core. Nguyen et al. [239] have shown that the a Cu_2O layer coated on amorphous Si thin film anode increases surface conductivity and stabilizes the SEI layer formation, leading to improved electrochemical performance. The increased surface conductivity is likely due to the formation of Cu particles on the surface during lithiation.

Conductive polymers are mechanically highly flexible and thus ideal coatings for large-volume-change electrodes. He et al. [233] have showed that alucone coating via molecular layer deposition process cleans up the native oxide layer, and therefore mitigates the detrimental effects of the native oxide. The coating leads to both high electrical and ionic conductivity, giving rise to high-rate performance. In a comparative study, Luo et al. [54] have observed that coating-regulated lithiation kinetics results in different lithiation morphologies. Alucone-coated SiNWs features V-shaped lithiation morphology, compared to H-shape lithiation morphology in Al_2O_3-coated SiNWs. The different lithiation morphologies suggest that the reaction rate in the alucone coating is much faster than in Al_2O_3 coating. The high mechanical flexibility of the alucone coating also enables concordant deformation between the coating and the SiNPs during the lithiation and lithiation cycles. The coating layer further suppresses the potential SiNP agglomeration during the lithiation/delithiation processes. Wu et al. [240] have reported that in-situ polymerized 3D porous conductive hydrogels can form a bi-functional conformal coating: binding to the SiNP surface as a coating layer and at the same time functioning as a 3D continuous electronic conduction pathway. In addition to the outstanding rate performance, the porous hydrogel matrix can accommodate large volume expansion of the SiNPs during lithiation. Even though pulverization of SiNPs might still occur, the polymer matrix can trap the fractured SiNPs in the interconnected narrow pores, thus helps maintain good electrical connectivity among fractured particles. Owing to the combined features, the conductive hydrogel coated SiNPs can be cycled up to 5000 times with less than 10% capacity decay.

Coating on porous structures minimizes the outward volume change and stabilizes the SEI growth by simultaneously exploiting the effects of surface coating and the porosity. In general, porosity reduces outer surface expansion of the active materials during lithiation. Coatings further suppress the outer surface expansion of the porous structures to a minimal level. Cui's group [37] has synthesized SiNTs coated with a SiO_2 layer and found that the inner space allows for expansion of Si without pulverization, while the outer surface remains static during lithiation, allowing stable SEI development. The anode material is of high-performance, with long cycle life of 6000 cycles with 88% capacity retention. In-situ TEM studies by Karki et al. [241] have shown that lithiation causes outward expansions of both the inner and outer walls in uncoated SiNTs. In

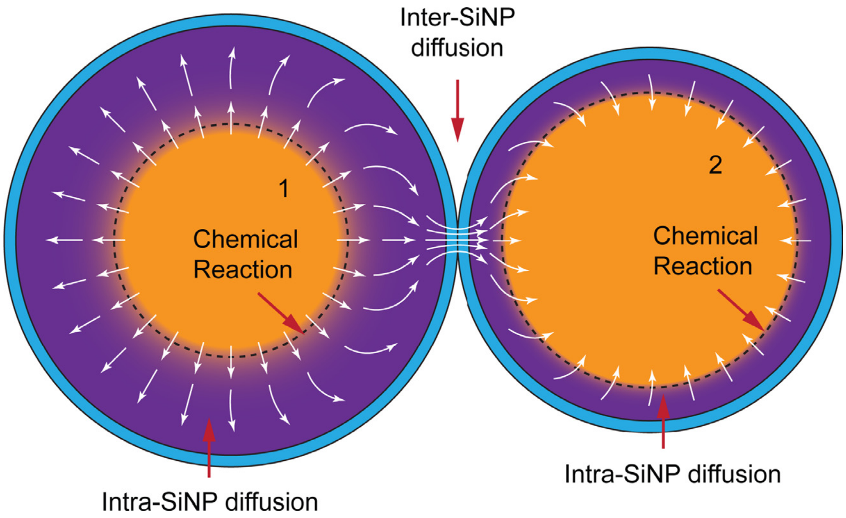

Fig. 18. The chemical potential of Li may be different in coated NPs when the initial NP size, lithiation depth, or the mechanical stress is different, driving inter-NP Li diffusion in coated NPs [55].

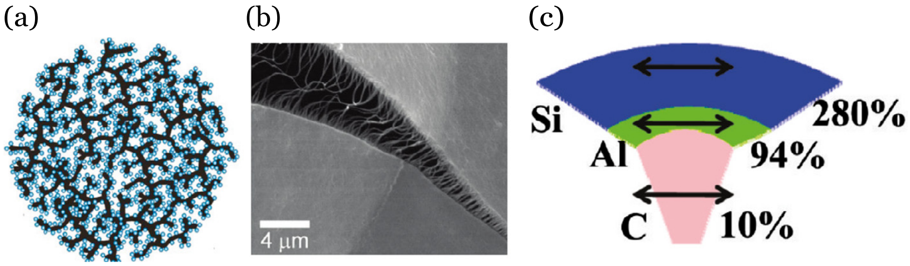

Fig. 19. Examples of composite materials used in LIB electrodes. (a) Schematic of carbon-black dendritic particles coated by SiNPs [256]. (b) SEM image of a broken CNT-Si film supported by a stainless steel mesh [30]. The mesh bridges the fractured film, maintaining mechanical integrity and electrical conductivity. (c) Schematic of Si-Al-C composite demonstrating the principle of strain-graded multilayer nanostructures [261].

contrast, when coated with a Ni layer, the outward expansion of the SiNTs is suppressed during lithiation and the inner free volume largely accommodates the volume expansion. The inward expansion depends on the thickness of the coated Ni layer. At a thickness of 16 nm, the outward expansion of the outer wall is fully suppressed. Many other coated porous materials have been developed [212,215,218,242] and enhanced electrochemical performance was reported as compared to solid Si anodes.

Yolk-shell particle represents a special core-shell structure, which features movable cores, pre-reserved void space between the core and the shell, and the controllability and functionality in both the core and the shell [243,244]. Noticeably, the active yolk expands and shrinks in the internal cavity without forming SEI, while the inert shell facing the electrolyte does not change volume but is covered with SEI. Thus, even if the yolk pulverizes the active contents are still fully confined in the closed shell. Several factors are essential to the improved electrochemical performance of the yolk-shell structures: (i) the shell should be thin enough to enable fast Li + ion and electron transport. The shell generally has a lower theoretical capacity so a thinner shells means higher overall specific capacity of the hybrid. (ii) the shell must be mechanically tough so that it does not fracture upon repeated lithiation/delithiation and volume change of the yolk. Third, the shell should be fully closed to prevent the direct contact between the electrolyte and the yolk – although as we will see, even if this might not be true initially, it can become true during cycling due to the self-healing effect. Fourth, there must be sufficient void space between the yolk and shell, otherwise the volume expansion of the yolk would break the shell and trigger both failure modes. Following the guidance, yolk-shell structures of different kinds have been developed. All achieved very high capacity retention and cycle life [244–249].

In typical battery cells, the anode consists of particle aggregates. During lithiation/delithiation cycles, neighboring SiNPs interact not only mechanically but also kinetically, and these two types of interactions are further coupled. While the mechanical interaction is well accepted (volumetric expansion causes inter-compression of neighboring SiNPs), the kinetic interaction has been less understood. For the uncoated SiNPs, the hydrostatic stress at the outer surfaces of the uncoated bare SiNPs is the same regardless of the particle size and lithiation depth. As a result, the Li chemical potential at the outer surface is the same throughout the lithiation process. This suggests that neighboring bare SiNPs are lithiated independently. In contrast, it has been shown that stress-mediated Li chemical potential at the outer surface of coated SiNPs depends on the initial SiNP size, lithiation thickness, and the mechanical stress. When two coated SiNPs are brought into contact and if any one of the three parameters are not the same, the difference of the Li chemical potentials may drive inter-SiNP Li diffusion (Fig. 18) [55], leading to discharging in one SiNP, and charging in the other. The inter-SiNP Li diffusion modifies Li concentration profile as well as the stress distribution inside the SiNPs, eventually reaching a thermodynamic equilibrium at which the inter-SiNP diffusion stops. This inter-SiNP Li diffusion dynamically occurs at different stages of lithiation, greatly impact the lithiation kinetics.

5.4. Compositing

Composite design is one of the most popular routes in materials synthesis to extend the cyclic life of batteries. In regard to high-capacity electrodes, the general philosophy is to use one material component (e.g., Si) to store Li, and the other (e.g., carbon) to enhance the overall conductivity and reduce volume expansion and improve mechanical stability. There is a large body of literature on the design of composite electrodes by selecting the size, shape, and pattern of the active materials, as well as the geometry and porosity of inactive phases [21,250–252]. Here we highlight a few examples that may represent some common features in the architecture design of composite materials. For instance, Gohier et al. homogeneously deposited 10 nm SiNPs on 5 nm CNTs [253]. They achieved capacities of 3000 mA h g^{-1} at 1.3 C, and found good rate capability (up to 15 C) with little polarization or structural damage. Sun et al. [254] formulated Si-beaded CNT strings with chemically functionalized interface, which plays important roles in confining the Si beads during the lithiation-delithiation cycling. Chen et al. deposited nano-silicon on a 3D virus-structured nickel current collector [255]. This complex structure has large surface area and is highly conductive, resulting in an initial capacity of 2300 mA h g^{-1}, a capacity of >1200 mA h g^{-1} after 173 cycles, and good rate performance. Magasinski et al. used a hierarchical bottom-up method to coat carbon-black dendritic particles

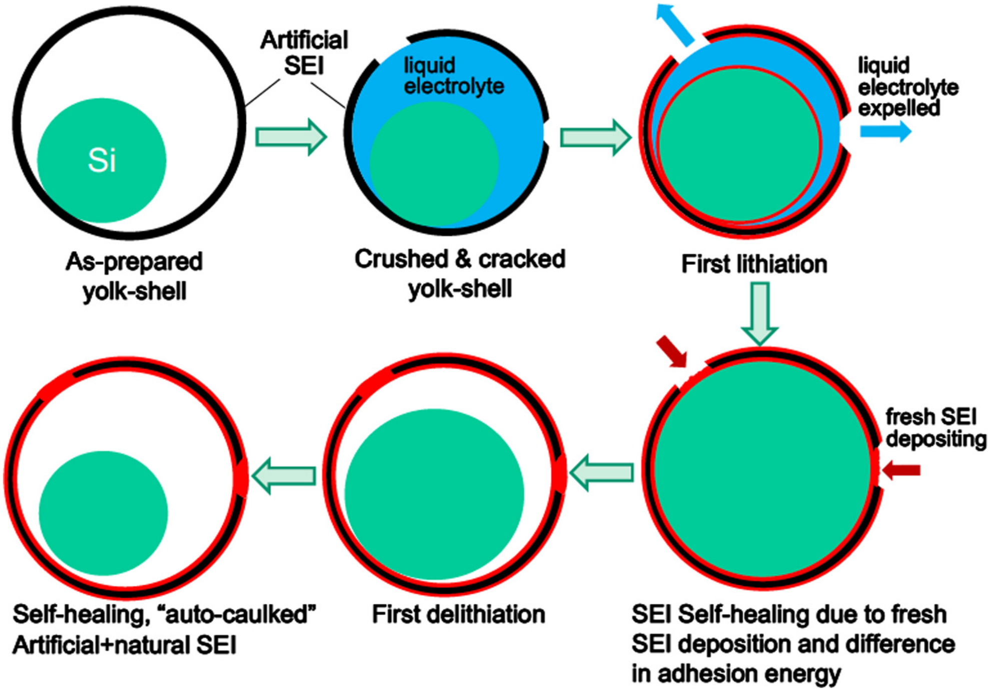

Fig. 20. Artificial SEI assisted self-healing process in yolk-shell anodes. Taken from [65].

with SiNPs, as shown in Fig. 19a [256]. This method is simple, safe, and low-cost, and results in reversible capacities of 1950 mA h g^{-1}. Zhang et al. sputtered a-Si onto Ni nano-cone arrays, resulting in a capacity of 2400 mA h g^{-1} over 100 cycles at a rate of C/2 and good performance at higher rates [257]. Yamada et al. dispersed nanosized silicon crystallites into an amorphous silicon dioxide matrix and then mixed with carbon black and polyvinyldifluorine (PVDF), resulting in 85% capacity retention after 100 cycles [258]. Cui et al. made free-standing composite CNT-Si films on stainless steel meshes up to 4 μm in thickness by CVD deposition [30]. This composite eliminated the need for a metal current collector, and demonstrated high specific charge storage capacity and good cycling performance. The performance was attributed to good mechanical strength and conductivity of the composite, as the CNT-Si film is bridged by the stainless steel mesh, even where fracture occurred in the film, as shown in Fig. 17b. Several groups also reported the carbon-silicon core-shell structure that uses carbon as a mechanical support when the silicon shell is fractured [259,260]. Krishnan et al. fabricated a Si-Al-C architecture to minimize the mismatch strain at the interfaces of the materials, as shown in Fig. 17c [261].

5.5. Self-healing electrodes

The self-healing ability of biological materials in nature significantly enhances their lifetimes. Motivated by the self-healing biology, self-healing electrode materials are highly desired, especially for high-volume-change electrode materials as they fracture or pulverize during lithiation/delithiation cycles. It has been reported that Galium, a low-melting point metal, exhibits self-healing ability as an anode. At a temperature above its melting temperature, Ga exhibits a reversible liquid-to-solid transition during lithiation-delithiation cycles. As such, cracks nucleated during lithiation automatically heal during delithiation, facilitated by the fluidity of the liquid phase. Liang et al. has showed that during delithiation of the Li_xGa phase, a single nanovoid appears [49]. The nanovoid automatically annihilates by the fast vacancy diffusion from the inner to the outer surfaces of the Li_xGa nanoparticles, driven by curvature-dependent chemical potential gradient of vacancies. Such low-melting-point metals can be used as self-healing agents in composite electrode materials.

Self-healing coatings and binders can significantly enhance the cycle life of electrode materials. Wang et al. reported that self-healing conductive polymeric coatings can improve the cycling life of Si microparticles (SiMPs) to more than one order of magnitude higher than bare SiNPs [262], despite SiMPs suffer pulverization upon lithiation. The self-healing ability is due to the several combined properties of the polymeric coating. First, the polymer is highly stretchable, able to sustain 300% strain without failure. This enables the accommodation of large volume expansion of the encapsulated SiMPs upon lithiation. Second, the self-healing polymer features a cross-linked network that permits dynamic association of hydrogen bonds. When cracks and damages occur in the coating, the network can spontaneously heal by dynamic reassociation of the hydrogen bonds at room temperature. With novel 3D spatial distribution of the self-healing polymer, the polymer-coated SiMP anode can achieve a very high area capacity (3–4 mA h cm^{-2}) [263]. Jeong et al. implemented similar self-healing polymeric binders to improve the cycling performance of Si anodes [264].

Jin et al. recently proposed a new self-healing strategy for yolk-shell electrodes [65]. Yolk-shell structure has achieved success in extending the cycle life owing to the pre-reserved excessive volume for accommodating the large volume change of the active materials. However, the shell may break when sufficient amount of volume expansion is transferred to it. In the absence of the self-healing ability, the electrolyte can invade the active materials from the cracked shell, causing unstable SEI growth and continuous consumption of cycleable Li. In the work of Jin et al., the shell is of a thin layer of TiO_2, which also functions as an artificial, self-healing SEI (aSEI) layer, as schematically shown in Fig. 20. The self-healing ability of TiO_2 shell arises from its several unique properties. First, the TiO_2 shell only weakly adheres to Si (yolk) so that the transfer of the dimensional change of the Si yolk to the TiO_2 shell upon lithiation is insignificant. Upon delithiation, the low adhesion strength facilitates the detachment of the shell from the yolk without causing damage of shell. Second, the shell is mechanically strong so that it does not fracture into pieces under the condition when the transfer of lithiation induced dimensional change of the active material to the shell does occur. Most importantly, the shell adheres strongly to the naturally grown SEI formed during the cycles. In the case that the TiO_2 layer does break during lithiation process, the liquid electrolyte would flush into the shell to invade the active material. The lithiation induced volume change in the next cycle would push evacuate the liquid out of the shell. Meanwhile, freshly formed natural SEI (nSEI) adhered to the aSEI automatically caulks the broken layer, thus self-sealing the yolk. Using the Coulombic inefficiency ($CI = 1 - CE$) as an indictor of liquid-tightness on the test electrode, Jin et al. quantified the efficiency of the self-healing aSEI. In the first few cycles, the CI is considerably high, showing the damage of the shell. Within about 20 cycles and 100 cycles, CI drops to 5×10^{-3} and 1×10^{-3}, clearly showing the self-repairing capability of the aSEI.

While nanostructuring like the sliding graphene sheath [265] can extend the cycle life of silicon anodes and improve $CE_{stabilized}$, all nanostructures presently suffer from low initial CE_n (due to larger surface area, the amount of SEI formed is large). Pre-lithiation is an approach to improve the low initial CE, as one uses sacrificial Li-containing compounds to provide the lithium source instead of the heavy and expensive $LiCoO_2$. Also, the nanostructured anode tends to suffer from low tap density, which could be improved by severe mechanical crushing, that may crack some artificial SEI protections, leading to non-hermiticity and electrolyte ingression that however may be healed. Much can be done in this area with the careful analysis technique presented in Eqs. (11)–(27).

5.6. Flexible batteries

Flexible batteries have emerged as a crucial power source for flexible, wearable electronics that generally operate in large deformation [266,267]. Thin film, or paper-based batteries have been pursued, as the thin film structures are able to effectively relax the lithiation induced mechanical stress by converting the volumetric deformation into out-of-plane curvature. Yu et al. developed a thin-film based electrode architecture, consisting of Si thin film deposited onto a soft Poly(dimethylsiloxane) (PDMS) substrate [268]. During charge-discharge cycles, the flat Si thin film freely buckles with little resistance from the PDMS substrates, thereby effectively releasing the stress in the thin film[269]. Such an anode has demonstrated a very low capacity fading rate (0.033% per cycle over 500 cycles), as compared to pure Si anode (4.5% per cycle over 20 cycles). Fu et al. fabricated free-standing, binder-free CNT-Si and CNT-Si-C thin-film structures, where super-aligned CNT sheet acts as current collector on which Si is uniformly deposited [270]. The CNT-Si thin film can be further surface-coated with a thin carbon layer, forming CNT-Si-C thin films. During electrochemical cycling, the CNT-Si thin sheet preserves its morphology, indicating effective strain relaxation. In contrast, the CNT-Si-C thin sheet buckles during the delithiation due to the incompatible compressive strain generated during delithiation. Both the composites showed high specific energy capacity and stable cycle performance. Zhu et al. used wood fibers as substrate for Sn anode for NIBs [271]. The microstructurally hierarchical wood fibers are naturally soft and porous, which are highly deformable and at the same time provide multichannels for fast ion transport. Wood fibers are also inexpensive and environmentally friendly. The wood-fiber based Sn anodes for NIBs have demonstrated highly improved stable SEI growth and cycling performance, as compared to the Cu@Sn anode. Song et al. fabricated origami LIBs [272], with active materials deposited onto CNT-coated papers as the current collectors. Predefined creases are introduced to the origami LIBs so that little strain except at the creases is imparted into the batteries during cycling. The origami design enables multiple deformation modes, and can be used to power deformable electronics.

6. Degradation of Na-ion batteries

Despite the great success of today's LIBs, the dramatic growth in demand for LIBs from electric vehicles and electric grids has significantly driven up the price of LiOH and Li_2CO_3 [273–276]. Sodium carbonate is much more abundant and cheaper than lithium carbonate [277–279]. Owing to the significant cost advantage and the natural abundance of sodium precursors, NIBs hold the potential to compete with LIBs and to reshape the electrochemical energy storage landscape. These factors have prompted increasing efforts on NIB technology development in recent years [273,280,281]. These advantages are however partially offset by the gravimetric and volumetric energy density penalties for NIBs since Na has larger ionic size and is heavier and less electropositive than Li. The larger ionic size also means larger insertion barrier and chemical insertion strain, rendering, respectively, lower rate performance and more severe chemomechanical degradation upon sodiation.

Early NIB studies have led to success in sodium-based high-temperature storage technologies, such as Na-S batteries operating at 300–350 °C. Recent efforts have been turned to room-temperature NIBs. The insertion chemistry in NIBs sometimes is vastly different from that in LIBs. Si, one of the most promising anode materials for LIBs, is inert to sodium insertion at low temperatures [282,283]. Graphite, the most popular anode for LIBs, cannot be directly used in NIBs [284,285] due to the much larger insertion barrier of Na^+ than Li^+. Various hard carbons with controlled surface area, morphology, and nanostructures, including expanded graphite with increased interlayer spacing and porous carbon, have been used as anodes for NIBs [286–291] with capacities generally no more than 500 mAh/g. Metal oxides and metal phosphates, such as $Na_2Ti_3O_7$ [292,293] and $NaTi_2(PO_4)_3$ [294,295] have also been assessed as anodes for NIBs. These anodes are typically of very low capacities (<200 mA h g^{-1}) and cannot meet the requirement for high-energy-density storage as Na-ion anodes.

Several group 14 and 15 elements [271,282,296–301] as well as their compounds [214,302–304] have high theoretical capacities, ranging from 500 to 2600 mA h g^{-1}, making them attractive anodes for NIBs (Fig. 2). For examples, Na-tin alloys showed a reversible capacity of about 500 mA h g^{-1} for more than 20 cycles, despite a huge volumetric expansion of about 420%. Microscopic Sb has a specific capacity of 600 mA h g^{-1} for more than 150 cycles, which even outperforms the same material in LIBs. SnSb alloys can deliver a capacity of 500 mA h g^{-1} at C/5 with an 80% capacity retention after 50 cycles.

Among these elementary materials, phosphorus and phosphorus-based compounds represent a promising class of candidates as anodes for NIBs [305–307], owing to its low cost and extremely high theoretical capacity of ~2600 mA h g^{-1} of phosphorous when sodiated to the Na_3P phase. Among the three main allotropes of phosphorus (white, red, and black), white phosphorus is generally excluded from the use as battery materials for its high reactivity and toxicity [308]. Amorphous red phosphorus has shown irreversible sodium insertion [301], and hence is not good candidate for anode either. With a layered structure, black phosphorus closely resembles graphite, and is better suited as an electrode material. The interlayer spacing of black phosphorus (5.4 Å) is much larger than that of graphite (3.4 Å) [308], suggesting that sodium ions can intercalate into black phosphorus much more easily than into graphite [309]. Recent experimental studies have shown that black phosphorus exhibits a much higher charge (2035 mA h g^{-1}) and discharge (637 mA h g^{-1}) capacities than red phosphorus [301]. It has also been reported that a graphene-phosphorene hybrid yields even higher capacity and more stable cyclability [308].

Similar to intermetallic alloy anodes (e.g., Si and Ge) for LIBs, phosphorus undergoes ~500% volume change during sodiation/desodiation [301] leading to pulverization of the active materials, unstable growth of SEI, and fast capacity fading [310–315]. In terms of its high capacity and large volume change, phosphorus in NIBs can be regarded as the counterpart of Si in LIBs. Sodiation of black phosphorus involves a two-step process in series: in the first step of sodiation (intercalation), sodium ions insert into black phosphorus along the pucker channels and fill out the interlayer space to form a $Na_{0.25}P$ phase; in the second step (alloying), further accumulated sodium breaks P—P bonds and transform the layered structure to amorphous sodium phosphide (Na_3P). More interestingly, it has been shown that black phosphorus shows anisotropic swelling upon sodiation [308]. The apparent anisotropic swelling possibly arises from the twofold intrinsic anisotropy: sodium diffusional directionality in black phosphorous and sodiation induced strain anisotropy. First, inherent to its pucker-layered structure, black phosphorus exhibits a "selective diffusional behavior" during the first step of intercalation [316]: sodium atoms preferably diffuse along the [1 0 0] direction due to the much lower sodium diffusion barriers in the [1 0 0] direction than in other directions. Limited by the low diffusivity in black phosphorous ($Na_{0.25}P$), the reaction front migrates very slowly along the [0 1 0] and [0 0 1] directions. This rate difference allows the Na-rich phase to easily catch up the reaction front, and likely results in a sharp interface along these two directions. Whereas along the [1 0 0] direction, the comparable sodium diffusivity in front of and behind the reaction front renders a diffuse interface. Second, unlike the cubic crystalline structure of *c*-Si for which lithium insertion induces isotropic chemical strain [43,102], the orthotropic layered structure of black phosphorus endows anisotropic chemical strain, with much larger expansion along the [0 0 1] direction than other directions. Chemomechanical modeling revealed that the apparent morphological evolution is critically controlled by the coupled effect of the two intrinsic anisotropies [127]. In particular, the sharp interphases generated along the [0 1 0] and [0 0 1] directions constrain anisotropic development of the insertion strain, giving rise to substantial difference in sodiation induced stress generation and fracture modes when sodiation starts from different crystal facets. This twofold anisotropy governed sodiation behavior is also significantly different from the orientation-dependent rate anisotropy in lithiation of *c*-Si.

7. Conclusions and perspectives

Energy density is one of the most important metrics for electrode materials. Intrinsic to the high-energy-density electrode materials is the large volume changes during electrochemical cycling, causing pulverization of active materials, lithiation retardation, and unstable SEI growth, thereby limiting the cycle life of the batteries. This review provides a survey of the chemomechanical degradation mechanisms for a variety of high-energy-density negative electrode materials for LIBs. A series of design strategies is also discussed toward mitigating the chemomechanical degradation. Throughout the review, we highlight the integrated real-time high-resolution microscopy and multiscale modeling as a powerful method for uncovering the underlying material degradation mechanisms.

A predominant feature in the degradation of high-energy-density electrode materials is the strong coupling between electrochemistry and mechanics, which critically influences the energy density and power capability of the batteries. On the one hand, electrochemical lithiation causes volume expansion and stress generation inside the active materials; on the other, the generated compressive stress retards lithiation. Such kinetics-stress coupling is ubiquitous and its extent varies in different designs. For instance, surface coating strengthens the coupling owing to the mechanical confinement, while nanoporosity weakens it. While the kinetics-stress coupling is generally detrimental to power capabilities of the electrode materials, reports have demonstrated that it can be exploited for mechanical energy harvesting.

To date, most studies for understanding the degradation of large-volume-change electrode materials such as Si have been focused on lithiation. This is partially because that *c*-Si, the most widely studied anode material, pulverizes and fractures during the first lithiation. In contrast, delithiation induced morphological change and its implications to the successive lithiation/delithiation cycles are less explored. We have observed the apparent difference in the lithiation behavior of Si in different cycles: *a*-Si features two-phase interphase in the first lithiation cycle but single-phase in the successive lithiation cycles. The difference may likely stem from the distinct microstructures produced during delithiation. It is widely known that pore formation is a ubiquitous phenomenon during delithiation. It is yet to be explored how the pore structures evolve upon multiple cycling and how these pore structures modify the cycling performance of the electrode materials.

With the help of the nanobattery platform for in-situ TEM characterization, much has been known as to the pulverization and fracture of various electrode materials. In contrast, other degradation modes such as unstable SEI growth in large-volume-change electrode materials are only beginning to be explored. It remains a great challenge to image the dynamic growth of the SEI layer in a realistic full-cell setting with liquid cells using the in-situ nanobattery platform. Given the diverse electrode-electrolyte interfaces, it is imperative to develop the nanobattery platform suitable for characterization of the SEI formation with atomic resolution, its mechanical properties and chemical compositions, thereby advancing the design toward full LIBs.

Electrochemical cycling of rechargeable batteries involves a variety of interfacial and surface processes. For examples, the characteristics of electrode-electrolyte interface regulate the electrochemical rate and SEI formation; the sharpness of the reaction front, i.e., the lithiated/unlithiated interface regulates the stress generation in the electrodes: nanoscale sharp interface causes stress concentration at the outer surface, while diffusive interface at the interior of the interface, giving rise to different crack initiation sites and consequently different failure modes. Nearly all the mitigation strategies to date more or less involve tailoring the surface or interfaces to enhance the overall performance of the electrode materials. An atomistic understanding of the interface and surface processes would be helpful to the material selection and design for controlling and mitigation of the degradation and enhancing the overall performance of the electrode materials.

The in-situ nanobattery platform has provided atomic scale degradation mechanisms of a variety of electrode materials on a single-particle level. To facilitate the full battery design, it is necessary to scale the research results up to the nanostructure assembly level, the electrode level, and the whole battery level wherein energy density is not the only performance matrix. Indeed, little is done even for a pair of nanoparticles under electrochemical cycling. Compatible electrolytes and positive electrodes are to be identified in order to, for instance, create a stable SEI layer, and to maximize and minimize the positive and negative electrode potentials so as to maximize the voltage window of the batteries.

Si as the leading promising anode material has been extensively explored and advanced to commercial usage. However, though the gravimetric capacity of the Si-majority anodes is very impressive (~1000 mAh/g even after 1500 cycles in half cells), their Coulombic efficiency is still low when compared with graphite in commercial LIBs. Future research in advanced material synthesis and processing techniques, combined with the mitigation protocols, is critically needed to boost the volumetric capacity of Si-majority anodes for widespread commercialization.

For wide-scale implementation, it is necessary to extend battery technology to large-scale, inexpensive, efficient energy storage in order to integrate intermittent renewable energies, such as wind, solar, and wave into the electrical grid. While LIB technology is quite mature, the rapidly increasing demand for Li will eventually drive up the prices and its costs become an issue. For this reason, cost-effective Na-ion based electrochemical energy storage is an alternative to Li-ion based systems. While NIBs share many similar characteristics to LIBs, new chemistry needs to be identified and exploited in order for NIBs to be competitive to LIBs.

Acknowledgements

S.Z. acknowledges the support by the National Science Foundation (NSF) through the projects CMMI-0900692, DMR-1610430, and ECCS-1610331. K.Z. acknowledges the support by NSF through the projects CBET-1603866, CMMI-1741100, CMMI-1726392, and the support by the Office of Naval Research (ONR) through the NEPTUNE program. T.Z. acknowledges support by the NSF Grant CMMI-1100205 and DMR-1410936. J.L. acknowledges the financial support by NSF ECCS-1610806.

Appendix A. Supplementary material

Supplementary data associated with this article can be found, in the online version, at http://dx.doi.org/10.1016/j.pmatsci.2017.04.014.

References

[1] Tarascon JM, Armand M. Issues and challenges facing rechargeable lithium batteries. Nature 2001;414:359–67.
[2] Whittingham MS. Materials challenges facing electrical energy storage. MRS Bull 2008;33:411–9.
[3] Goodenough JB. Rechargeable batteries: challenges old and new. J Solid State Electrochem 2012;16:2019–29.
[4] Goodenough JB, Kim Y. Challenges for rechargeable Li batteries. Chem Mater 2010;22:587–603.
[5] Tarascon JM. Key challenges in future Li-battery research. Philos Trans R Soc A-Math Phys Eng Sci 2010;368:3227–41.
[6] Armand M, Tarascon JM. Building better batteries. Nature 2008;451:652–7.
[7] Chiang Y-M. Building a better battery. Science 2010;330:1485–6.
[8] Goodenough JB, Park K-S. The Li-ion rechargeable battery: a perspective. J Am Chem Soc 2013;135:1167–76.
[9] Service RF. Getting there. Science 2011;332:1494–6.
[10] Nazri G-A, Pistoia G. Lithium batteries: science and technology. Springer Science & Business Media; 2008.
[11] Huggins R. Advanced batteries: materials science aspects. Springer; 2008.
[12] Beaulieu LY, Eberman KW, Turner RL, Krause LJ, Dahn JR. Colossal reversible volume changes in lithium alloys. Electrochem Solid State Lett 2001;4:A137–40.
[13] Limthongkul P, Jang Y-I, Dudney NJ, Chiang Y-M. Electrochemically-driven solid-state amorphization in lithium-silicon alloys and implications for lithium storage. Acta Mater 2003;51:1103–13.
[14] Graetz J, Ahn CC, Yazami R, Fultz B. Nanocrystalline and thin film germanium electrodes with high lithium capacity and high rate capabilities. J Electrochem Soc 2004;151:A698–702.
[15] Chan CK, Patel RN, O'Connell MJ, Korgel BA, Cui Y. Solution-grown silicon nanowires for lithium-ion battery anodes. ACS Nano 2010;4:1443–50.
[16] Chan CK, Peng HL, Liu G, McIlwrath K, Zhang XF, Huggins RA, et al. High-performance lithium battery anodes using silicon nanowires. Nat Nanotechnol 2008;3:31–5.
[17] Chan CK, Zhang XF, Cui Y. High capacity Li ion battery anodes using Ge nanowires. Nano Lett 2008;8:307–9.
[18] Huang JY, Zhong L, Wang CM, Sullivan JP, Xu W, Zhang LQ, et al. In Situ observation of the electrochemical lithiation of a single SnO_2 nanowire electrode. Science 2010;330:1515–20.
[19] Kamali AR, Fray DJ. Review on carbon and silicon based materials as anode materials for lithium ion batteries. J New Mater Electrochem Syst 2010;13:147–60.
[20] Marom R, Amalraj SF, Leifer N, Jacob D, Aurbach D. A review of advanced and practical lithium battery materials. J Mater Chem 2011;21:9938–54.
[21] Zhang WJ. A review of the electrochemical performance of alloy anodes for lithium-ion batteries. J Power Sources 2011;196:13–24.
[22] Neumann G, Würsig A. Lithium storage in silicon. Phys Status Solidi (RRL) – Rapid Res Lett 2010;4:A21–3.
[23] Reddy MV, Rao GVS, Chowdari BVR. Metal oxides and oxysalts as anode materials for Li ion batteries. Chem Rev 2013;113:5364–457.
[24] Wang F, Robert R, Chernova NA, Pereira N, Omenya F, Badway F, et al. Conversion reaction mechanisms in lithium ion batteries: study of the binary metal fluoride electrodes. J Am Chem Soc 2011;133:18828–36.
[25] Yuan CZ, Wu HB, Xie Y, Lou XW. Mixed transition-metal oxides: design, synthesis, and energy-related applications. Angew Chem-Int Ed 2014;53:1488–504.
[26] Cabana J, Monconduit L, Larcher D, Palacin MR. Beyond intercalation-based Li-ion batteries: the state of the art and challenges of electrode materials reacting through conversion reactions. Adv Mater 2010;22:E170–92.
[27] Berg EJ, Villevieille C, Streich D, Trabesinger S, Novak P. Rechargeable batteries: grasping for the limits of chemistry. J Electrochem Soc 2015;162:A2468–75.
[28] Goldman JL, Long BR, Gewirth AA, Nuzzo RG. Strain anisotropies and self-limiting capacities in single-crystalline 3D silicon microstructures: models for high energy density lithium-ion battery anodes. Adv Func Mater 2011;21:2412–22.
[29] Lee SW, McDowell MT, Choi JW, Cui Y. Anomalous shape changes of silicon nanopillars by electrochemical lithiation. Nano Lett 2011;11:3034–9.
[30] Cui LF, Hu LB, Choi JW, Cui Y. Light-weight free-standing carbon nanotube-silicon films for anodes of lithium ion batteries. ACS Nano 2010;4:3671–8.
[31] Liu XH, Zhong L, Huang S, Mao SX, Zhu T, Huang JY. Size-dependent fracture of silicon nanoparticles during lithiation. ACS Nano 2012;6:1522–31.
[32] Lee SW, McDowell MT, Berla LA, Nix WD, Cui Y. Fracture of crystalline silicon nanopillars during electrochemical lithium insertion. Proc Natl Acad Sci USA 2012;109:4080–5.
[33] McDowell MT, Ryu I, Lee SW, Wang C, Nix WD, Cui Y. Studying the kinetics of crystalline silicon nanoparticle lithiation with in situ transmission electron microscopy. Adv Mater 2012;24:6034–41.
[34] Liang W, Yang H, Fan F, Liu Y, Liu XH, Huang JY, et al. Tough germanium nanoparticles under electrochemical cycling. ACS Nano 2013;7:3427–33.
[35] Ulvestad A, Singer A, Clark JN, Cho HM, Kim JW, Harder R, et al. Topological defect dynamics in operando battery nanoparticles. Science 2015;348:1344–7.
[36] Seungjin L, Yang J, Lu W. Debonding at the interface between active particles and PVDF binder in Li-ion batteries. Extreme Mech Lett 2015;6:37–44.
[37] Wu H, Chan G, Choi JW, Ryu I, Yao Y, McDowell MT, et al. Stable cycling of double-walled silicon nanotube battery anodes through solid-electrolyte interphase control. Nat Nanotechnol 2012;7:309–14.
[38] Gireaud L, Grugeon S, Laruelle S, Yrieix B, Tarascon JM. Lithium metal stripping/plating mechanisms studies: a metallurgical approach. Electrochem Commun 2006;8:1639–49.
[39] Liu S, Imanishi N, Zhang T, Hirano A, Takeda Y, Yamamoto O, et al. Lithium dendrite formation in Li/poly(ethylene oxide)-lithium bis(trifluoromethanesulfonyl)imide and N-methyl-N-propylpiperidinium bis(trifluoromethanesulfonyl)imide/Li cells. J Electrochem Soc 2010;157:A1092–8.
[40] Liu XH, Fan F, Yang H, Zhang S, Huang JY, Zhu T. Self-limiting lithiation in silicon nanowires. ACS Nano 2012;7:1495–503.
[41] Liu XH, Wang JW, Huang S, Fan F, Huang X, Liu Y, et al. In situ atomic-scale imaging of electrochemical lithiation in silicon. Nat Nano 2012;7:749–56.
[42] Liu XH, Zhang LQ, Zhong L, Liu Y, Zheng H, Wang JW, et al. Ultrafast electrochemical lithiation of individual Si nanowire anodes. Nano Lett 2011;11:2251–8.
[43] Liu XH, Zheng H, Zhong L, Huang S, Karki K, Zhang LQ, et al. Anisotropic swelling and fracture of silicon nanowires during lithiation. Nano Lett 2011;11:3312–8.
[44] McDowell MT, Lee SW, Harris JT, Korgel BA, Wang C, Nix WD, et al. In situ TEM of two-phase lithiation of amorphous silicon nanospheres. Nano Lett 2013;13:758–64.
[45] Liu XH, Huang S, Picraux ST, Li J, Zhu T, Huang JY. Reversible nanopore formation in Ge nanowires during lithiation-delithiation cycling: an in situ transmission electron microscopy study. Nano Lett 2011;11:3991–7.
[46] Liu Y, Liu XH, Nguyen B-M, Yoo J, Sullivan JP, Picraux ST, et al. Tailoring lithiation behavior by interface and bandgap engineering at the nanoscale. Nano Lett 2013;13:4876–83.
[47] Gu M, Yang H, Perea DE, Zhang J-G, Zhang S, Wang C-M. Bending-induced symmetry breaking of lithiation in germanium nanowires. Nano Lett 2014;14:4622–7.
[48] Liu Y, Zheng H, Liu XH, Huang S, Zhu T, Wang JW, et al. Lithiation-induced embrittlement of multiwalled carbon nanotubes. ACS Nano 2011;5:7245–53.
[49] Liang W, Hong L, Yang H, Fan F, Liu Y, Li H, et al. Nanovoid formation and annihilation in gallium nanodroplets under lithiation-delithiation cycling. Nano Lett 2013;13:5212–7.
[50] Liu XH, Wang JW, Liu Y, Zheng H, Kushima A, Huang S, et al. In situ transmission electron microscopy of electrochemical lithiation, delithiation and deformation of individual graphene nanoribbons. Carbon 2012;50:3836–44.

[51] Niu J, Kushima A, Qian X, Qi L, Xiang K, Chiang Y-M, et al. In situ observation of random solid solution zone in $LiFePO_4$ electrode. Nano Lett 2014;14:4005–10.
[52] Zhu Y, Wang JW, Liu Y, Liu X, Kushima A, Liu Y, et al. In situ atomic-scale imaging of phase boundary migration in FePO4 microparticles during electrochemical lithiation. Adv Mater 2013;25:5461–6.
[53] Xiao Q, Gu M, Yang H, Li B, Zhang C, Liu Y, et al. Inward lithium-ion breathing of hierarchically porous silicon anodes. Nat Commun 2015;6:8844.
[54] Luo LL, Yang H, Yan PF, Travis JJ, Lee Y, Liu N, et al. Surface-coating regulated lithiation kinetics and degradation in silicon nanowires for lithium ion battery. ACS Nano 2015;9:5559–66.
[55] Luo LL, Zhang P, Yang H, Liu B, Zhang JG, Cui Y, et al. Surface-coating constraint induced self-discharging of silicon nanoparticles as anodes for lithium ion batteries. Nano Lett 2015;15:7016–22.
[56] Zhu T, Li J. Ultra-strength materials. Prog Mater Sci 2010;55:710–57.
[57] Kushima A, So KP, Su C, Bai P, Kuriyama N, Maebashi T, et al. Liquid cell transmission electron microscopy observation of lithium metal growth and dissolution: root growth, dead lithium and lithium flotsams. Nano Energy 2017;32:271–9.
[58] Zhang L, Zhang Z-C, Amine K. In: Belharouak I, editor. Lithium Ion batteries - new developments. InTech; 2012.
[59] Lim H-D, Lee B, Zheng Y, Hong J, Kim J, Gwon H, et al. Rational design of redox mediators for advanced Li–O_2 batteries. Nat Energy 2016;1:16066.
[60] Ning XH, Phadke S, Chung B, Yin HY, Burke P, Sadoway DR. Self-healing Li-Bi liquid metal battery for grid-scale energy storage. J Power Sources 2015;275:370–6.
[61] Poux T, Novak P, Trabesingerz S. Pitfalls in Li-S rate-capability evaluation. J Electrochem Soc 2016;163:A1139–45.
[62] Zhu Z, Kushima A, Yin Z, Qi L, Amine K, Lu J, et al. Anion-redox nanolithia cathodes for Li-ion batteries. Nat Energy 2016;1:16111.
[63] Wang S, Yang Y, Quan W, Hong Y, Zhang Z, Tang Z, et al. Ti3+-free three-phase $Li_4Ti_5O_{12}/TiO_2$ for high-rate lithium ion batteries: capacity and conductivity enhancement by phase boundaries. Nano Energy 2017;32:294–301.
[64] Xu G, Yan Q-b, Kushima A, Zhang X, Pan J, Li J. Conductive graphene oxide-polyacrylic acid (GOPAA) binder for lithium-sulfur battery. Nano Energy 2017;31:568–74.
[65] Jin Y, Li S, Kushima A, Zheng X, Sun Y, Xie J, et al. Self-healing SEI enables full-cell cycling of silicon-majority anode with coulombic efficiency exceeding 99.9%. Energy. Environ Sci 2017;10:580–92.
[66] Au M, McWhorter S, Ajo H, Adams T, Zhao YP, Gibbs J. Free standing aluminum nanostructures as anodes for Li-ion rechargeable batteries. J Power Sources 2010;195:3333–7.
[67] Kushima A, Huang JY, Li J. Quantitative fracture strength and plasticity measurements of lithiated silicon nanowires by in situ TEM tensile experiments. ACS Nano 2012;6:9425–32.
[68] Boles ST, Thompson CV, Kraft O, Mönig R. In situ tensile and creep testing of lithiated silicon nanowires. Appl Phys Lett 2013;103:263906.
[69] Hertzberg B, Benson J, Yushin G. Ex-situ depth-sensing indentation measurements of electrochemically produced Si–Li alloy films. Electrochem Commun 2011;13:818–21.
[70] Berla LA, Lee SW, Cui Y, Nix WD. Mechanical behavior of electrochemically lithiated silicon. J Power Sources 2015;273:41–51.
[71] de Vasconcelos LS, Xu R, Li J, Zhao K. Grid indentation analysis of mechanical properties of composite electrodes in Li-ion batteries. Extreme Mech Lett 2016;9:495–502.
[72] Chon MJ, Sethuraman VA, McCormick A, Srinivasan V, Guduru PR. Real-time measurement of stress and damage evolution during initial lithiation of crystalline silicon. Phys Rev Lett 2011;107:045503.
[73] Zhao K, Tritsaris GA, Pharr M, Wang WL, Okeke O, Suo Z, et al. Reactive flow in silicon electrodes assisted by the insertion of lithium. Nano Lett 2012;12:4397–403.
[74] Pharr M, Suo Z, Vlassak JJ. Measurements of the fracture energy of lithiated silicon electrodes of Li-ion batteries. Nano Lett 2013;13:5570–7.
[75] Wang X, Fan F, Wang J, Wang H, Tao S, Yang A, et al. High damage tolerance of electrochemically lithiated silicon. Nat Commun 2015;6:8417.
[76] Zeng Z, Liu N, Zeng Q, Lee SW, Mao WL, Cui Y. In situ measurement of lithiation-induced stress in silicon nanoparticles using micro-Raman spectroscopy. Nano Energy 2016;22:105–10.
[77] Ratchford J, Crawford B, Wolfenstine J, Allen J, Lundgren C. Young's modulus of polycrystalline Li 12 Si 7 using nanoindentation testing. J Power Sources 2012;211:1–3.
[78] Amanieu H-Y, Aramfard M, Rosato D, Batista L, Rabe U, Lupascu DC. Mechanical properties of commercial $LixMn_2O_4$ cathode under different States of Charge. Acta Mater 2015;89:153–62.
[79] Brassart L, Suo Z. Reactive flow in solids. J Mech Phys Solids 2013;61:61–77.
[80] Yang H, Liang W, Guo X, Wang C, Zhang S. Strong kinetics-stress coupling in lithiated Si and Ge electrodes. Extreme Mech Lett 2015;2:1–6.
[81] Pyun S-I, Go J-Y, Jang T-S. An investigation of intercalation-induced stresses generated during lithium transport through $Li_{1-\delta}CoO_2$ film electrode using a laser beam deflection method. Electrochim Acta 2004;49:4477–86.
[82] Kim Y-H, Pyun S-I, Go J-Y. An investigation of intercalation-induced stresses generated during lithium transport through sol–gel derived $Li_xMn_2O_4$ film electrode using a laser beam deflection method. Electrochim Acta 2005;51:441–9.
[83] Sethuraman VA, Chon MJ, Shimshak M, Srinivasan V, Guduru PR. In situ measurements of stress evolution in silicon thin films during electrochemical lithiation and delithiation. J Power Sources 2010;195:5062–6.
[84] Sethuraman VA, Srinivasan V, Bower AF, Guduru PR. In situ measurements of stress-potential coupling in lithiated silicon. J Electrochem Soc 2010;157:A1253–61.
[85] Choi YS, Pharr M, Oh KH, Vlassak JJ. A simple technique for measuring the fracture energy of lithiated thin-film silicon electrodes at various lithium concentrations. J Power Sources 2015;294:159–66.
[86] Pharr M, Choi YS, Lee D, Oh KH, Vlassak JJ. Measurements of stress and fracture in germanium electrodes of lithium-ion batteries during electrochemical lithiation and delithiation. J Power Sources 2016;304:164–9.
[87] Kim S, Choi SJ, Zhao K, Yang H, Gobbi G, Zhang S, et al. Electrochemically driven mechanical energy harvesting. Nat Commun 2016;7:10146.
[88] Kubota Y, Escano MCS, Nakanishi H, Kasai H. Crystal and electronic structure of $Li_{15}Si_4$. J Appl Phys 2007;102:053704.
[89] Kubota Y, Escano MCS, Nakanishi H, Kasai H. Electronic structure of LiSi. J Alloy Compd 2008;458:151–7.
[90] Chevrier VL, Dahn JR. First principles model of amorphous silicon lithiation. J Electrochem Soc 2009;156:A454–8.
[91] Chevrier VL, Dahn JR. First principles studies of disordered lithiated silicon. J Electrochem Soc 2010;157:A392–8.
[92] Shenoy VB, Johari P, Qi Y. Elastic softening of amorphous and crystalline Li-Si phases with increasing Li concentration: a first-principles study. J Power Sources 2010;195:6825–30.
[93] Zhang QF, Zhang WX, Wan WH, Cui Y, Wang EG. Lithium insertion in silicon nanowires: an ab initio study. Nano Lett 2010;10:3243–9.
[94] Wan WH, Zhang QF, Cui Y, Wang EG. First principles study of lithium insertion in bulk silicon. J Phys-Condes Matter 2010;22:415501.
[95] Zhang Q, Cui Y, Wang E. Anisotropic lithium insertion behavior in silicon nanowires: binding energy, diffusion barrier, and strain effect. J Phys Chem C 2011;115:9376–81.
[96] Chevrier VL, Zwanziger JW, Dahn JR. First principles studies of silicon as a negative electrode material for lithium-ion batteries. Can J Phys 2009;87:625–32.
[97] Kim H, Kweon KE, Chou C-Y, Ekerdt JG, Hwang GS. On the nature and behavior of Li atoms in Si: a first principles study. J Phys Chem C 2010;114:17942–6.
[98] Zhao K, Wang WL, Gregoire J, Pharr M, Suo Z, Vlassak JJ, et al. Lithium-assisted plastic deformation of silicon electrodes in lithium-ion batteries: a first-principles theoretical study. Nano Lett 2011;11:2962–7.
[99] Yang H, Huang X, Liang W, van Duin ACT, Raju M, Zhang S. Self-weakening in lithiated graphene electrodes. Chem Phys Lett 2013;563:58–62.

[100] Fan F, Huang S, Yang H, Raju M, Datta D, Shenoy V, et al. Mechanical properties of amorphous LixSi alloys: a reactive force field study. Modell Simul Mater Sci Eng 2013;21:074002.
[101] Ostadhossein A, Cubuk ED, Tritsaris GA, Kaxiras E, Zhang SL, van Duin ACT. Stress effects on the initial lithiation of crystalline silicon nanowires: reactive molecular dynamics simulations using ReaxFF. Phys Chem Chem Phys 2015;17:3832–40.
[102] Yang H, Huang S, Huang X, Fan F, Liang W, Liu XH, et al. Orientation-dependent interfacial mobility governs the anisotropic swelling in lithiated silicon nanowires. Nano Lett 2012;12:1953–8.
[103] Bhandakkar TK, Gao HJ. Cohesive modeling of crack nucleation under diffusion induced stresses in a thin strip: implications on the critical size for flaw tolerant battery electrodes. Int J Solids Struct 2010;47:1424–34.
[104] Christensen J, Newman J. Stress generation and fracture in lithium insertion materials. J Solid State Electrochem 2006;10:293–319.
[105] Zhang XC, Shyy W, Sastry AM. Numerical simulation of intercalation-induced stress in Li-ion battery electrode particles. J Electrochem Soc 2007;154: A910–6.
[106] Deshpande R, Cheng YT, Verbrugge MW. Modeling diffusion-induced stress in nanowire electrode structures. J Power Sources 2010;195:5081–8.
[107] Woodford WH, Chiang YM, Carter WC. "Electrochemical Shock" of intercalation electrodes: a fracture mechanics analysis. J Electrochem Soc 2010;157:A1052–9.
[108] Chandrasekaran R, Magasinski A, Yushin G, Fuller TF. Analysis of lithium insertion/deinsertion in a silicon electrode particle at room temperature. J Electrochem Soc 2010;157:A1139–51.
[109] Zhao KJ, Pharr M, Vlassak JJ, Suo ZG. Inelastic hosts as electrodes for high-capacity lithium-ion batteries. J Appl Phys 2011;109:016110.
[110] Gao YF, Zhou M. Strong stress-enhanced diffusion in amorphous lithium alloy nanowire electrodes. J Appl Phys 2011;109:014310.
[111] Bower AF, Chason E, Guduru PR, Sheldon BW. A continuum model of deformation, transport and irreversible changes in atomic structure in amorphous lithium-silicon electrodes. Acta Mater 2015;98:229–41.
[112] Bucci G, Nadimpalli SPV, Sethuraman VA, Bower AF, Guduru PR. Measurement and modeling of the mechanical and electrochemical response of amorphous Si thin film electrodes during cyclic lithiation. J Mech Phys Solids 2014;62:276–94.
[113] Nadimpalli SPV, Sethuraman VA, Dalavi S, Lucht B, Chon MJ, Shenoy VB, et al. Quantifying capacity loss due to solid-electrolyte-interphase layer formation on silicon negative electrodes in lithium-ion batteries. J Power Sources 2012;215:145–51.
[114] Chen L, Fan F, Hong L, Chen J, Ji YZ, Zhang SL, et al. A phase-field model coupled with large elasto-plastic deformation: application to lithiated silicon electrodes. J Electrochem Soc 2014;161:F3164–72.
[115] Yang H, Fan F, Liang W, Guo X, Zhu T, Zhang S. A chemo-mechanical model of lithiation in silicon. J Mech Phys Solids 2014;70:349–61.
[116] Zhao K, Pharr M, Cai S, Vlassak JJ, Suo Z. Large plastic deformation in high-capacity lithium-ion batteries caused by charge and discharge. J Am Ceram Soc 2011;94:s226–35.
[117] Zhao K, Pharr M, Wan Q, Wang WL, Kaxiras E, Vlassak JJ, et al. Concurrent reaction and plasticity during initial lithiation of crystalline silicon in lithium-ion batteries. J Electrochem Soc 2012;159:A238–43.
[118] An YH, Wood BC, Ye JC, Chiang YM, Wang YM, Tang M, et al. Mitigating mechanical failure of crystalline silicon electrodes for lithium batteries by morphological design. Phys Chem Chem Phys 2015;17:17718–28.
[119] Zhang SL, Zhu T, Belytschko T. Atomistic and multiscale analyses of brittle fracture in crystal lattices. Phys Rev B 2007;76:094114.
[120] Grantab R, Shenoy VB. Pressure-gradient dependent diffusion and crack propagation in lithiated silicon nanowires. J Electrochem Soc 2012;159: A584–91.
[121] Sheldon BW, Soni SK, Xiao XC, Qi Y. Stress contributions to solution thermodynamics in Li-Si alloys. Electrochem Solid State Lett 2012;15:A9–A11.
[122] Bower A. Applied mechanics of solids. CRC Press; 2010.
[123] Bower AF, Guduru PR. A simple finite element model of diffusion, finite deformation, plasticity and fracture in lithium ion insertion electrode materials. Modell Simul Mater Sci Eng 2012;20:045004.
[124] Gao YF, Zhou M. Strong dependency of lithium diffusion on mechanical constraints in high-capacity Li-ion battery electrodes. Acta Mech Sin 2012;28:1068–77.
[125] Gao YF, Zhou M. Coupled mechano-diffusional driving forces for fracture in electrode materials. J Power Sources 2013;230:176–93.
[126] Huang S, Fan F, Li J, Zhang S, Zhu T. Stress generation during lithiation of high-capacity electrode particles in lithium ion batteries. Acta Mater 2013;61:4354–64.
[127] Chen T, Zhao P, Guo X, Zhang S. Two-fold anisotropy governs morphological evolution and stress generation in sodiated black phosphorus for sodium ion batteries. Nano Lett 2017;17:2299–306.
[128] Cui ZW, Gao F, Qu JM. A finite deformation stress-dependent chemical potential and its applications to lithium ion batteries. J Mech Phys Solids 2012;60:1280–95.
[129] Khosrownejad SM, Curtin WA. Model for charge/discharge-rate-dependent plastic flow in amorphous battery materials. J Mech Phys Solids 2016;94:167–80.
[130] Jia Z, Liu WK. Rate-dependent stress evolution in nanostructured Si anodes upon lithiation. Appl Phys Lett 2016;109:163903.
[131] Pharr M, Suo ZG, Vlassak JJ. Variation of stress with charging rate due to strain-rate sensitivity of silicon electrodes of Li-ion batteries. J Power Sources 2014;270:569–75.
[132] Wen CJ, Huggins RA. Chemical diffusion in intermediate phases in the lithium-silicon system. J Solid State Chem 1981;37:271–8.
[133] Boukamp BA, Lesh GC, Huggins RA. All-solid lithium electrodes with mixed-conductor matrix. J Electrochem Soc 1981;128:725–9.
[134] Wang JW, He Y, Fan F, Liu XH, Xia S, Liu Y, et al. Two-phase electrochemical lithiation in amorphous silicon. Nano Lett 2013;13:709–15.
[135] Chan MKY, Wolverton C, Greeley JP. First principles simulations of the electrochemical lithiation and delithiation of faceted crystalline silicon. J Am Chem Soc 2012;134:14362–74.
[136] Chan MKY, Long BR, Gewirth AA, Greeley JP. The first-cycle electrochemical lithiation of crystalline ge: dopant and orientation dependence and comparison with Si. J Phys Chem Lett 2011;2:3092–5.
[137] Baggetto L, Notten PHL. Lithium-ion (de)insertion reaction of germanium thin-film electrodes: an electrochemical and in situ XRD study. J Electrochem Soc 2009;156:A169–75.
[138] Larcher D, Beattie S, Morcrette M, Edstrom K, Jumas J-C, Tarascon J-M. Recent findings and prospects in the field of pure metals as negative electrodes for Li-ion batteries. J Mater Chem 2007;17:3759–72.
[139] Kamata Y. High-k/Ge MOSFETs for future nanoelectronics. Mater Today 2008;11:30–8.
[140] Fuller CS, Severiens JC. Mobility of impurity ions in germanium and silicon. Phys Rev 1954;96:21–4.
[141] Limthongkul P. Electrochemically-driven solid-state amorphization in lithium–metal anodes. J Power Sources 2003;119–121:604–9.
[142] Kamali AR, Fray DJ. Tin-based materials as advanced anode materials for lithium ion batteries: a review. Adv Mater Sci 2011;27:14–24.
[143] Xu Y, Zhu Y, Liu Y, Wang C. Electrochemical performance of porous carbon/tin composite anodes for sodium-ion and lithium-ion batteries. Adv Energy Mater 2013;3:128–33.
[144] Wang JW, Fan FF, Liu Y, Jungjohann KL, Lee SW, Mao SX, et al. Structural evolution and pulverization of tin nanoparticles during lithiation-delithiation cycling. J Electrochem Soc 2014;161:F3019–24.
[145] Li QQ, Wang P, Feng Q, Mao MM, Liu JB, Mao SX, et al. In situ TEM on the reversibility of nanosized Sn anodes during the electrochemical reaction. Chem Mater 2014;26:4102–8.
[146] Chao S-C, Song Y-F, Wang C-C, Sheu H-S, Wu H-C, Wu N-L. Study on microstructural deformation of working Sn and SnSb anode particles for Li-Ion batteries by in situ transmission X-ray microscopy. J Phys Chem C 2011;115:22040–7.
[147] Chao S-C, Yen Y-C, Song Y-F, Chen Y-M, Wu H-C, Wu N-L. A study on the interior microstructures of working Sn particle electrode of Li-ion batteries by in situ X-ray transmission microscopy. Electrochem Commun 2010;12:234–7.

[148] Karki K, Epstein E, Cho J-H, Jia Z, Li T, Picraux ST, et al. Lithium-assisted electrochemical welding in silicon nanowire battery electrodes. Nano Lett 2012;12:1392–7.
[149] Jung YS, Lee KT, Ryu JH, Im D, Oh SM. Sn-carbon core-shell powder for anode in lithium secondary batteries. J Electrochem Soc 2005;152:A1452–7.
[150] Li H, Wang Q, Shi L, Chen L, Huang X. Nanosized SnSb alloy pinning on hard non-graphitic carbon spherules as anode materials for a Li ion battery. Chem Mater 2001;14:103–8.
[151] Courtney IA, McKinnon W, Dahn J. On the aggregation of tin in SnO composite glasses caused by the reversible reaction with lithium. J Electrochem Soc 1999;146:59–68.
[152] Kim C, Noh M, Choi M, Cho J, Park B. Critical size of a nano SnO_2 electrode for Li-secondary battery. Chem Mater 2005;17:3297–301.
[153] Brownson DAC, Kampouris DK, Banks CE. An overview of graphene in energy production and storage applications. J Power Sources 2011;196:4873–85.
[154] Gao B, Kleinhammes A, Tang XP, Bower C, Fleming L, Wu Y, et al. Electrochemical intercalation of single-walled carbon nanotubes with lithium. Chem Phys Lett 1999;307:153–7.
[155] Landi BJ, Ganter MJ, Cress CD, DiLeo RA, Raffaelle RP. Carbon nanotubes for lithium ion batteries. Energy Environ Sci 2009;2:638–54.
[156] Lahiri I, Oh SW, Hwang JY, Cho S, Sun YK, Banerjee R, et al. High capacity and excellent stability of lithium ion battery anode using interface-controlled binder-free multiwall carbon nanotubes grown on copper. ACS Nano 2010;4:3440–6.
[157] Mielke SL, Troya D, Zhang S, Li JL, Xiao SP, Car R, et al. The role of vacancy defects and holes in the fracture of carbon nanotubes. Chem Phys Lett 2004;390:413–20.
[158] Zhang SL, Mielke SL, Khare R, Troya D, Ruoff RS, Schatz GC, et al. Mechanics of defects in carbon nanotubes: atomistic and multiscale simulations. Phys Rev B 2005;71:115403.
[159] Huang X, Yang H, Liang WT, Raju M, Terrones M, Crespi VH, et al. Lithiation induced corrosive fracture in defective carbon nanotubes. Appl Phys Lett 2013;103:153901.
[160] Eom J, Kim D, Kwon H. Effects of ball-milling on lithium insertion into multi-walled carbon nanotubes synthesized by thermal chemical vapour deposition. J Power Sources 2006;157:507–14.
[161] Masarapu C, Subramanian V, Zhu H, Wei B. Long-cycle electrochemical behavior of multiwall carbon nanotubes synthesized on stainless steel in Li ion batteries. Adv Func Mater 2009;19:1008–14.
[162] Chen S, Yeoh W, Liu Q, Wang G. Chemical-free synthesis of graphene–carbon nanotube hybrid materials for reversible lithium storage in lithium-ion batteries. Carbon 2012;50:4557–65.
[163] Sun J, Liu H, Chen X, Evans DG, Yang W, Duan X. Carbon nanorings and their enhanced lithium storage properties. Adv Mater 2013;25:1125–30.
[164] Nie A, Gan L-Y, Cheng Y, Asayesh-Ardakani H, Li Q, Dong C, et al. Atomic-scale observation of lithiation reaction front in nanoscale SnO_2 materials. ACS Nano 2013;7:6203–11.
[165] Kushima A, Liu XH, Zhu G, Wang ZL, Huang JY, Li J. Leapfrog cracking and nanoamorphization of ZnO nanowires during in situ electrochemical lithiation. Nano Lett 2011;11:4535–41.
[166] Zhang Y, Wang Z, Li Y, Zhao K. Lithiation of ZnO nanowires studied by in-situ transmission electron microscopy and theoretical analysis. Mech Mater 2015;91:313–22.
[167] Su QM, Xie D, Zhang J, Du GH, Xu BS. In situ transmission electron microscopy observation of the conversion mechanism of Fe_2O_3/graphene anode during lithiation-delithiation processes. ACS Nano 2013;7:9115–21.
[168] Chen Q, Sieradzki K. Spontaneous evolution of bicontinuous nanostructures in dealloyed Li-based systems. Nat Mater 2013;12:1102–6.
[169] Newman RC, Corcoran SG, Erlebacher J, Aziz MJ, Sieradzki K. Alloy corrosion. MRS Bull 1999;24:24–8.
[170] Chen Q, Sieradzki K. Mechanisms and morphology evolution in dealloying. J Electrochem Soc 2013;160:C226–31.
[171] Pickerin Hw, Wagner C. Electrolytic dissolution of binary alloys containing a noble metal. J Electrochem Soc 1967;114:698–706.
[172] Sieradzki K, Corderman RR, Shukla K, Newman RC. Computer-simulations of corrosion - selective dissolution of binary-alloys. Philos Mag Phys Cond Matter Struct Defects Mech Prop 1989;59:713–46.
[173] Erlebacher J, Aziz MJ, Karma A, Dimitrov N, Sieradzki K. Evolution of nanoporosity in dealloying. Nature 2001;410:450–3.
[174] Rugolo J, Erlebacher J, Sieradzki K. Length scales in alloy dissolution and measurement of absolute interfacial free energy. Nat Mater 2006;5:946–9.
[175] Sieradzki K, Dimitrov N, Movrin D, McCall C, Vasiljevic N, Erlebacher J. The dealloying critical potential. J Electrochem Soc 2002;149:B370–7.
[176] Choi JW, McDonough J, Jeong S, Yoo JS, Chan CK, Cui Y. Stepwise nanopore evolution in one-dimensional nanostructures. Nano Lett 2010;10:1409–13.
[177] Berla LA, Lee SW, Ryu I, Cui Y, Nix WD. Robustness of amorphous silicon during the initial lithiation/delithiation cycle. J Power Sources 2014;258:253–9.
[178] Jia Z, Li T. Intrinsic stress mitigation via elastic softening during two-step electrochemical lithiation of amorphous silicon. J Mech Phys Solids 2016;91:278–90.
[179] Szczech JR, Jin S. Nanostructured silicon for high capacity lithium battery anodes. Energy Environ Sci 2011;4:56–72.
[180] Peng KQ, Jie JS, Zhang WJ, Lee ST. Silicon nanowires for rechargeable lithium-ion battery anodes. Appl Phys Lett 2008;93:033105.
[181] Choi HS, Lee JG, Lee HY, Kim SW, Park CR. Effects of surrounding confinements of Si nanoparticles on Si-based anode performance for lithium ion batteries. Electrochim Acta 2010;56:790–6.
[182] Ma H, Cheng FY, Chen J, Zhao JZ, Li CS, Tao ZL, et al. Nest-like silicon nanospheres for high-capacity lithium storage. Adv Mater 2007;19:4067–70.
[183] Yao Y, McDowell MT, Ryu I, Wu H, Liu N, Hu L, et al. Interconnected silicon hollow nanospheres for lithium-ion battery anodes with long cycle life. Nano Lett 2011;11:2949–54.
[184] Wu H, Zheng G, Liu N, Carney TJ, Yang Y, Cui Y. Engineering empty space between Si nanoparticles for lithium-ion battery anodes. Nano Lett 2012;12:904–9.
[185] Maranchi JP, Hepp AF, Kumta PN. High capacity, reversible silicon thin-film anodes for lithium-ion batteries. Electrochem Solid-State Lett 2003;6: A198–201.
[186] Maranchi JP, Hepp AF, Evans AG, Nuhfer NT, Kumta PN. Interfacial properties of the a-Si/Cu: active-inactive thin-film anode system for lithium-ion batteries. J Electrochem Soc 2006;153:A1246–53.
[187] Nadimpalli SPV, Sethuraman VA, Bucci G, Srinivasan V, Bower AF, Guduru PR. On plastic deformation and fracture in Si films during electrochemical lithiation/delithiation cycling. J Electrochem Soc 2013;160:A1885–93.
[188] Wan JY, Kaplan AF, Zheng J, Han XG, Chen YC, Weadock NJ, et al. Two dimensional silicon nanowalls for lithium ion batteries. J Mater Chem A 2014;2:6051–7.
[189] Bonaccorso F, Colombo L, Yu GH, Stoller M, Tozzini V, Ferrari AC, et al. Graphene, related two-dimensional crystals, and hybrid systems for energy conversion and storage. Science 2015;347:1246501.
[190] Britnell L, Ribeiro RM, Eckmann A, Jalil R, Belle BD, Mishchenko A, et al. Strong light-matter interactions in heterostructures of atomically thin films. Science 2013;340:1311–4.
[191] Naguib M, Come J, Dyatkin B, Presser V, Taberna PL, Simon P, et al. MXene: a promising transition metal carbide anode for lithium-ion batteries. Electrochem Commun 2012;16:61–4.
[192] Du GD, Guo ZP, Wang SQ, Zeng R, Chen ZX, Liu HK. Superior stability and high capacity of restacked molybdenum disulfide as anode material for lithium ion batteries. Chem Commun 2010;46:1106–8.
[193] Xie Y, Dall'Agnese Y, Naguib M, Gogotsi Y, Barsoum MW, Zhuang HLL, et al. Prediction and characterization of MXene nanosheet anodes for non-lithium-ion batteries. ACS Nano 2014;8:9606–15.
[194] Shevchenko EV, Talapin DV, Kotov NA, O'Brien S, Murray CB. Structural diversity in binary nanoparticle superlattices. Nature 2006;439:55–9.

[195] Ye XC, Chen J, Engel M, Millan JA, Li WB, Qi L, et al. Competition of shape and interaction patchiness for self-assembling nanoplates. Nat Chem 2013;5:466–73.
[196] Shin HC, Corno JA, Gole JL, Liu ML. Porous silicon negative electrodes for rechargeable lithium batteries. J Power Sources 2005;139:314–20.
[197] Kim H, Cho J. Superior lithium electroactive mesoporous Si@carbon core–shell nanowires for lithium battery anode material. Nano Lett 2008;8:3688–91.
[198] Paek S-M, Yoo E, Honma I. Enhanced cyclic performance and lithium storage capacity of SnO(2)/graphene nanoporous electrodes with three-dimensionally delaminated flexible structure. Nano Lett 2009;9:72–5.
[199] Cho J. Porous Si anode materials for lithium rechargeable batteries. J Mater Chem 2010;20:4009–14.
[200] Guo JC, Sun A, Wang CS. A porous silicon-carbon anode with high overall capacity on carbon fiber current collector. Electrochem Commun 2010;12:981–4.
[201] Yang LC, Gao QS, Li L, Tang Y, Wu YP. Mesoporous germanium as anode material of high capacity and good cycling prepared by a mechanochemical reaction. Electrochem Commun 2010;12:418–21.
[202] Astrova EV, Fedulova GV, Smirnova IA, Remenyuk AD, Kulova TL, Skundin AM. Porous silicon based negative electrodes for lithium ion batteries. Tech Phys Lett 2011;37:731–4.
[203] Qu YQ, Zhou HL, Duan XF. Porous silicon nanowires. Nanoscale 2011;3:4060–8.
[204] Wang X-L, Han W-Q, Chen H, Bai J, Tyson TA, Yu X-Q, et al. Amorphous hierarchical porous GeOx as high-capacity anodes for Li ion batteries with very long cycling life. J Am Chem Soc 2011;133:20692–5.
[205] Ge M, Rong J, Fang X, Zhou C. Porous doped silicon nanowires for lithium ion battery anode with long cycle life. Nano Lett 2012;12:2318–23.
[206] Song T, Jeon Y, Samal M, Han H, Park H, Ha J, et al. A Ge inverse opal with porous walls as an anode for lithium ion batteries. Energy Environ Sci 2012;5:9028–33.
[207] Thakur M, Isaacson M, Sinsabaugh SL, Wong MS, Biswal SL. Gold-coated porous silicon films as anodes for lithium ion batteries. J Power Sources 2012;205:426–32.
[208] Zhao Y, Liu XZ, Li HQ, Zhai TY, Zhou HS. Hierarchical micro/nano porous silicon Li-ion battery anodes. Chem Commun 2012;48:5079–81.
[209] Ge M, Fang X, Rong J, Zhou C. Review of porous silicon preparation and its application for lithium-ion battery anodes. Nanotechnology 2013;24:422001.
[210] Thakur M, Pernites R, Sinsabaugh SL, Wong MS, Biswal SL. Porous silicon as anode material for lithium-ion batteries. In: Li H, Wu J, Wang ZM, editors. Silicon-based nanomaterials. p. 1–23.
[211] Cheng H, Xiao R, Bian HD, Li Z, Zhan YW, Tsang CK, et al. Periodic porous silicon thin films with interconnected channels as durable anode materials for lithium ion batteries. Mater Chem Phys 2014;144:25–30.
[212] Du FH, Li B, Fu W, Xiong YJ, Wang KX, Chen JS. Surface binding of polypyrrole on porous silicon hollow nanospheres for Li-ion battery anodes with high structure stability. Adv Mater 2014;26:6145–50.
[213] Ge MY, Lu YH, Ercius P, Rong JP, Fang X, Mecklenburg M, et al. Large-scale fabrication, 3D tomography, and lithium-ion battery application of porous Silicon. Nano Lett 2014;14:261–8.
[214] Ji L, Gu M, Shao Y, Li X, Engelhard MH, Arey BW, et al. Controlling SEI formation on SnSb-porous carbon nanofibers for improved Na ion storage. Adv Mater 2014;26:2901–8.
[215] Shen LY, Wang ZX, Chen LQ. Carbon-coated hierarchically porous silicon as anode material for lithium ion batteries. RSC Adv 2014;4:15314–8.
[216] Bie YT, Yu JL, Yang J, Lu W, Nuli YN, Wang JL. Porous microspherical silicon composite anode material for lithium ion battery. Electrochim Acta 2015;178:65–73.
[217] Han X, Chen HX, Liu JJ, Liu HH, Wang P, Huang K, et al. A peanut shell inspired scalable synthesis of three-dimensional carbon coated porous silicon particles as an anode for lithium-ion batteries. Electrochim Acta 2015;156:11–9.
[218] Kim YM, Ahn J, Yu SH, Chung DY, Lee KJ, Lee JK, et al. Titanium silicide coated porous silicon nanospheres as anode materials for lithium ion batteries. Electrochim Acta 2015;151:256–62.
[219] Wang W, Favors Z, Ionescu R, Ye R, Bay HH, Ozkan M, et al. Monodisperse porous silicon spheres as anode materials for lithium ion batteries. Sci Rep 2015;5:8781.
[220] Park MH, Kim MG, Joo J, Kim K, Kim J, Ahn S, et al. Silicon nanotube battery anodes. Nano Lett 2009;9:3844–7.
[221] Bogart TD, Oka D, Lu XT, Gu M, Wang CM, Korgel BA. Lithium ion battery peformance of silicon nanowires with carbon skin. ACS Nano 2014;8:915–22.
[222] Chatterjee S, Carter R, Oakes L, Erwin WR, Bardhan R, Pint CL. Electrochemical and corrosion stability of nanostructured silicon by graphene coatings: toward high power porous silicon supercapacitors. J Phys Chem C 2014;118:10893–902.
[223] Chen YL, Hu Y, Shao JZ, Shen Z, Chen RZ, Zhang XW, et al. Pyrolytic carbon-coated silicon/carbon nanofiber composite anodes for high-performance lithium-ion batteries. J Power Sources 2015;298:130–7.
[224] Fu K, Xue LG, Yildiz O, Li SL, Lee H, Li Y, et al. Effect of CVD carbon coatings on Si@CNF composite as anode for lithium-ion batteries. Nano Energy 2013;2:976–86.
[225] Kong JH, Yee WA, Wei YF, Yang LP, Ang JM, Phua SL, et al. Silicon nanoparticles encapsulated in hollow graphitized carbon nanofibers for lithium ion battery anodes. Nanoscale 2013;5:2967–73.
[226] Li QQ, Li WQ, Feng Q, Wang P, Mao MM, Liu JB, et al. Thickness-dependent fracture of amorphous carbon coating on SnO_2 nanowire electrodes. Carbon 2014;80:793–8.
[227] Li WH, Li MS, Yang ZZ, Xu J, Zhong XW, Wang JQ, et al. Carbon-coated germanium nanowires on carbon nanofibers as self-supported electrodes for flexible lithium-ion batteries. Small 2015;11:2762–7.
[228] Li ZF, Zhang HY, Liu Q, Liu YD, Stanciu L, Xie J. Novel pyrolyzed polyaniline-grafted silicon nanoparticles encapsulated in graphene sheets as Li-ion battery anodes. ACS Appl Mater Interfaces 2014;6:5996–6002.
[229] Zhang F, Yang X, Xie YQ, Yi NB, Huang Y, Chen YS. Pyrolytic carbon-coated Si nanoparticles on elastic graphene framework as anode materials for high-performance lithium-ion batteries. Carbon 2015;82:161–7.
[230] Zhao GY, Zhang L, Meng YF, Zhang NQ, Sun KN. High storage performance of core-shell Si@C nanoparticles as lithium ion battery anode material. Mater Lett 2013;96:170–3.
[231] Sandu G, Brassart L, Gohy JF, Pardoen T, Melinte S, Vlad A. Surface coating mediated swelling and fracture of silicon nanowires during lithiation. ACS Nano 2014;8:9427–36.
[232] Kohandehghan A, Cui K, Kupsta M, Memarzadeh E, Kalisvaart P, Mitlin D. Nanometer-scale Sn coatings improve the performance of silicon nanowire LIB anodes. J Mater Chem A 2014;2:11261–79.
[233] He Y, Piper DM, Gu M, Travis JJ, George SM, Lee SH, et al. In situ transmission electron microscopy probing of native oxide and artificial layers on silicon nanoparticles for lithium ion batteries. ACS Nano 2014;8:11816–23.
[234] Zhang YF, Li YJ, Wang ZY, Zhao KJ. Lithiation of SiO_2 in Li-ion batteries: in situ transmission electron microscopy experiments and theoretical studies. Nano Lett 2014;14. 7181–7170.
[235] Li JC, Xiao XC, Cheng YT, Verbrugge MW. Atomic layered coating enabling ultrafast surface kinetics at silicon electrodes in lithium ion batteries. J Phys Chem Lett 2013;4:3387–91.
[236] Ye JC, An YH, Heo TW, Biener MM, Nikolic RJ, Tang M, et al. Enhanced lithiation and fracture behavior of silicon mesoscale pillars via atomic layer coatings and geometry design. J Power Sources 2014;248:447–56.
[237] Li Y, Sun YJ, Xu GJ, Lu Y, Zhang S, Xue LG, et al. Tuning electrochemical performance of Si-based anodes for lithium-ion batteries by employing atomic layer deposition alumina coating. J Mater Chem A 2014;2:11417–25.

[238] Zhu B, Liu N, McDowell M, Jin Y, Cui Y, Zhu J. Interfacial stabilizing effect of ZnO on Si anodes for lithium ion battery. Nano Energy 2015;13:620–5.

[239] Nguyen SH, Lim JC, Lee JK. Improving the performance of silicon anode in lithium-ion batteries by Cu_2O coating layer. J Appl Electrochem 2014;44:353–60.

[240] Wu H, Yu GH, Pan LJ, Liu NA, McDowell MT, Bao ZA, et al. Stable Li-ion battery anodes by in-situ polymerization of conducting hydrogel to conformally coat silicon nanoparticles. Nat Commun 2013;4:1943.

[241] Karki K, Zhu YJ, Liu YH, Sun CF, Hu LB, Wang YH, et al. Hoop-strong nanotubes for battery electrodes. ACS Nano 2013;7:8295–302.

[242] Lotfabad EM, Kalisvaart P, Kohandehghan A, Cui K, Kupsta M, Farbod B, et al. Si nanotubes ALD coated with TiO_2, TiN or Al_2O_3 as high performance lithium ion battery anodes. J Mater Chem A 2014;2:2504–16.

[243] Liu J, Qiao SZ, Chen JS, Lou XW, Xing XR, Lu GQ. Yolk/shell nanoparticles: new platforms for nanoreactors, drug delivery and lithium-ion batteries. Chem Commun 2011;47:12578–91.

[244] Liu N, Wu H, McDowell MT, Yao Y, Wang CM, Cui Y. A yolk-shell design for stabilized and scalable Li-ion battery alloy anodes. Nano Lett 2012;12:3315–21.

[245] Choi SH, Kang YC. Yolk-shell, hollow, and single-crystalline $ZnCo_2O_4$ powders: preparation using a simple one-pot process and application in lithium-ion batteries. Chemsuschem 2013;6:2111–6.

[246] Seh ZW, Li WY, Cha JJ, Zheng GY, Yang Y, McDowell MT, et al. FSulphur-TiO_2 yolk-shell nanoarchitecture with internal void space for long-cycle lithium-sulphur batteries. Nat Commun 2013;4:1331.

[247] Choi SH, Kang YC. Synthesis for yolk-shell-structured metal sulfide powders with excellent electrochemical performances for lithium-ion batteries. Small 2014;10:474–8.

[248] Wang JX, Li W, Wang F, Xia YY, Asiri AM, Zhao DY. Controllable synthesis of SnO_2@C yolk-shell nanospheres as a high-performance anode material for lithium ion batteries. Nanoscale 2014;6:3217–22.

[249] Yang LY, Li HZ, Liu J, Sun ZQ, Tang SS, Lei M. Dual yolk-shell structure of carbon and silica-coated silicon for high-performance lithium-ion batteries. Sci Rep 2015;5:10908.

[250] Kasavajjula U, Wang C, Appleby AJ. Nano-and bulk-silicon-based insertion anodes for lithium-ion secondary cells. J Power Sources 2007;163:1003–39.

[251] Saint J, Morcrette M, Larcher D, Laffont L, Beattie S, Pérès JP, et al. Towards a fundamental understanding of the improved electrochemical performance of silicon–carbon composites. Adv Func Mater 2007;17:1765–74.

[252] Choi N-S, Yao Y, Cui Y, Cho J. One dimensional Si/Sn-based nanowires and nanotubes for lithium-ion energy storage materials. J Mater Chem 2011;21:9825–40.

[253] Gohier A, Laïk B, Kim KH, Maurice JL, Pereira-Ramos JP, Cojocaru CS, et al. High-rate capability silicon decorated vertically aligned carbon nanotubes for Li-ion batteries. Adv Mater 2012;24:2592–7.

[254] Sun C-F, Karki K, Jia Z, Liao H, Zhang Y, Li T, et al. A beaded-string silicon anode. ACS Nano 2013;7:2717–24.

[255] Chen X, Gerasopoulos K, Guo J, Brown A, Wang C, Ghodssi R, et al. A patterned 3D silicon anode fabricated by electrodeposition on a virus-structured current collector. Adv Func Mater 2011;21:380–7.

[256] Magasinski A, Dixon P, Hertzberg B, Kvit A, Ayala J, Yushin G. High-performance lithium-ion anodes using a hierarchical bottom-up approach. Nat Mater 2010;9:353–8.

[257] Zhang S, Du Z, Lin R, Jiang T, Liu G, Wu X, et al. Nickel nanocone-array supported silicon anode for high-performance lithium-ion batteries. Adv Mater 2010;22:5378–82.

[258] Yamada M, Ueda A, Matsumoto K, Ohzuku T. Silicon-based negative electrode for high-capacity lithium-ion batteries:"SiO"-carbon composite. J Electrochem Soc 2011;158:A417–21.

[259] Wang JW, Liu XH, Zhao K, Palmer A, Patten E, Burton D, et al. Sandwich-lithiation and longitudinal crack in amorphous silicon coated on carbon nanofibers. ACS Nano 2012;6:9158–67.

[260] Cui L-F, Yang Y, Hsu C-M, Cui Y. Carbon− silicon core− shell nanowires as high capacity electrode for lithium ion batteries. Nano Lett 2009;9:3370–4.

[261] Krishnan R, Lu T-M, Koratkar N. Functionally strain-graded nanoscoops for high power Li-ion battery anodes. Nano Lett 2010;11:377–84.

[262] Wang C, Wu H, Chen Z, McDowell MT, Cui Y, Bao ZA. Self-healing chemistry enables the stable operation of silicon microparticle anodes for high-energy lithium-ion batteries. Nat Chem 2013;5:1042–8.

[263] Chen Z, Wang C, Lopez J, Lu ZD, Cui Y, Bao ZA. High-areal-capacity silicon electrodes with low-cost silicon particles based on spatial control of self-healing binder. Adv Energy Mater 2015;5:1401826.

[264] Jeong YK, Kwon TW, Lee I, Kim TS, Coskun A, Choi JW. Hyperbranched beta-cyclodextrin polymer as an effective multidimensional binder for silicon anodes in lithium rechargeable batteries. Nano Lett 2014;14:864–70.

[265] Son IH, Hwan Park J, Kwon S, Park S, Rümmeli MH, Bachmatiuk A, et al. Silicon carbide-free graphene growth on silicon for lithium-ion battery with high volumetric energy density. Nat Commun 2015;6:7393.

[266] Nyholm L, Nystrom G, Mihranyan A, Stromme M. Toward flexible polymer and paper-based energy storage devices. Adv Mater 2011;23:3751–69.

[267] Shi JJ, Guo X, Chen RJ, Wu F. Recent progress in flexible battery. Prog Chem 2016;28:577–88.

[268] Yu CJ, Li X, Ma T, Rong JP, Zhang RJ, Shaffer J, et al. Silicon thin films as anodes for high-performance lithium-ion batteries with effective stress relaxation. Adv Energy Mater 2012;2:68–73.

[269] Jia Z, Li T. Failure mechanics of a wrinkling thin film anode on a substrate under cyclic charging and discharging. Extreme Mech Lett 2016;8:273–82.

[270] Fu K, Yildiz O, Bhanushali H, Wang YX, Stano K, Xue LG, et al. Aligned carbon nanotube-silicon sheets: a novel nano-architecture for flexible lithium ion battery electrodes. Adv Mater 2013;25:5109–14.

[271] Zhu HL, Jia Z, Chen YC, Weadock N, Wan JY, Vaaland O, et al. Tin anode for sodium-ion batteries using natural wood fiber as a mechanical buffer and electrolyte reservoir. Nano Lett 2013;13:3093–100.

[272] Song ZM, Ma T, Tang R, Cheng Q, Wang X, Krishnaraju D, et al. Origami lithium-ion batteries. Nat Commun 2014;5:3140.

[273] Slater MD, Kim D, Lee E, Johnson CS. Sodium-ion batteries. Adv Func Mater 2013;23:947–58.

[274] Hagen M, Dörfler S, Fanz P, Berger T, Speck R, Tübke J, et al. Development and costs calculation of lithium–sulfur cells with high sulfur load and binder free electrodes. J Power Sources 2013;224:260–8.

[275] Wadia C, Albertus P, Srinivasan V. Resource constraints on the battery energy storage potential for grid and transportation applications. J Power Sources 2011;196:1593–8.

[276] Pan H, Hu Y-S, Chen L. Room-temperature stationary sodium-ion batteries for large-scale electric energy storage. Energy Environ Sci 2013;6:2338–60.

[277] CRC handbook of chemistry and physics, 95th ed. CRC Press; 2014.

[278] Dolley TP. SODA ASH; 2014.

[279] Evans RK. An abundance of lithium; 2008.

[280] Ellis BL, Nazar LF. Sodium and sodium-ion energy storage batteries. Curr Opin Solid State Mater Sci 2012;16:168–77.

[281] Palomares V, Serras P, Villaluenga I, Hueso KB, Carretero-Gonzalez J, Rojo T. Na-ion batteries, recent advances and present challenges to become low cost energy storage systems. Energy Environ Sci 2012;5:5884–901.

[282] Ellis LD, Wilkes BN, Hatchard TD, Obrovac MN. In situ XRD study of silicon, lead and bismuth negative electrodes in nonaqueous sodium cells. J Electrochem Soc 2014;161:A416–21.

[283] Komaba S, Matsuura Y, Ishikawa T, Yabuuchi N, Murata W, Kuze S. Redox reaction of Sn-polyacrylate electrodes in aprotic Na cell. Electrochem Commun 2012;21:65–8.

[284] Chen J-j, Zhang Q, Shi Y-n, Qin L-l, Cao Y, Zheng M-s, et al. A hierarchical architecture S/MWCNT nanomicrosphere with large pores for lithium sulfur batteries. Phys Chem Chem Phys 2012;14:5376–82.

[285] Ge P, Fouletier M. Electrochemical intercalation of sodium in graphite. Solid State Ionics. 1988;28–30(Part 2):1172–5.

[286] Luo W, Schardt J, Bommier C, Wang B, Razink J, Simonsen J, et al. Carbon nanofibers derived from cellulose nanofibers as a long-life anode material for rechargeable sodium-ion batteries. J Mater Chem A 2013;1:10662–6.

[287] Zhao J, Zhao L, Chihara K, Okada S, J-i Yamaki, Matsumoto S, et al. Electrochemical and thermal properties of hard carbon-type anodes for Na-ion batteries. J Power Sources 2013;244:752–7.

[288] Ponrouch A, Goñi AR, Palacín MR. High capacity hard carbon anodes for sodium ion batteries in additive free electrolyte. Electrochem Commun 2013;27:85–8.

[289] Wang Z, Qie L, Yuan L, Zhang W, Hu X, Huang Y. Functionalized N-doped interconnected carbon nanofibers as an anode material for sodium-ion storage with excellent performance. Carbon 2013;55:328–34.

[290] Wen Y, He K, Zhu Y, Han F, Xu Y, Matsuda I, et al. Expanded graphite as superior anode for sodium-ion batteries. Nat Commun 2014;5:4033.

[291] Palomares V, Casas-Cabanas M, Castillo-Martínez E, Han MH, Rojo T. Update on Na-based battery materials. A growing research path. Energy Environ Sci 2013;6:2312–37.

[292] Senguttuvan P, Rousse G, Seznec V, Tarascon J-M, Palacín MR. $Na_2Ti_3O_7$: lowest voltage ever reported oxide insertion electrode for sodium ion batteries. Chem Mater 2011;23:4109–11.

[293] Rudola A, Saravanan K, Mason CW, Balaya P. $Na_2Ti_3O_7$: an intercalation based anode for sodium-ion battery applications. J Mater Chem A 2013;1:2653–62.

[294] Park SI, Gocheva I, Okada S, Yamaki J-i. Electrochemical properties of $NaTi_2(PO_4)_3$ anode for rechargeable aqueous sodium-ion batteries. J Electrochem Soc 2011;158:A1067–70.

[295] Wu W, Mohamed A, Whitacre JF. Microwave synthesized $NaTi_2(PO_4)_3$ as an aqueous sodium-ion negative electrode. J Electrochem Soc 2013;160: A497–504.

[296] Wang W, Yu C, Lin Z, Hou J, Zhu H, Jiao S. Microspheric $Na_2Ti_3O_7$ consisting of tiny nanotubes: an anode material for sodium-ion batteries with ultrafast charge-discharge rates. Nanoscale 2013;5:594–9.

[297] Liu Y, Xu Y, Zhu Y, Culver JN, Lundgren CA, Xu K, et al. Tin-coated viral nanoforests as sodium-ion battery anodes. ACS Nano 2013;7:3627–34.

[298] Datta MK, Epur R, Saha P, Kadakia K, Park SK, Kumta PN. Tin and graphite based nanocomposites: potential anode for sodium ion batteries. J Power Sources 2013;225:316–22.

[299] Yabuuchi N, Matsuura Y, Ishikawa T, Kuze S, Son J-Y, Cui Y-T, et al. Phosphorus electrodes in sodium cells: small volume expansion by sodiation and the surface-stabilization mechanism in aprotic solvent. ChemElectroChem 2014;1:580–9.

[300] Kim Y, Park Y, Choi A, Choi N-S, Kim J, Lee J, et al. An amorphous red phosphorus/carbon composite as a promising anode material for sodium ion batteries. Adv Mater 2013;25:3045–9.

[301] Qian J, Wu X, Cao Y, Ai X, Yang H. High capacity and rate capability of amorphous phosphorus for sodium ion batteries. Angew Chem Int Ed Engl 2013;52:4633–6.

[302] Xiao L, Cao Y, Xiao J, Wang W, Kovarik L, Nie Z, et al. High capacity, reversible alloying reactions in SnSb/C nanocomposites for Na-ion battery applications. Chem Commun 2012;48:3321–3.

[303] Kim Y, Kim Y, Choi A, Woo S, Mok D, Choi N-S, et al. Tin phosphide as a promising anode material for Na-ion batteries. Adv Mater 2014;26:4139–44.

[304] Qian J, Xiong Y, Cao Y, Ai X, Yang H. Synergistic Na-storage reactions in Sn4P3 as a high-capacity, cycle-stable anode of Na-ion batteries. Nano Lett 2014;14:1865–9.

[305] Kim SW, Seo DH, Ma XH, Ceder G, Kang K. Electrode materials for rechargeable sodium-ion batteries: potential alternatives to current lithium-ion batteries. Adv Energy Mater 2012;2:710–21.

[306] Marino C, Debenedetti A, Fraisse B, Favier F, Monconduit L. Activated-phosphorus as new electrode material for Li-ion batteries. Electrochem Commun 2011;13:346–9.

[307] Stevens DA, Dahn JR. High capacity anode materials for rechargeable sodium-ion batteries. J Electrochem Soc 2000;147:1271–3.

[308] Sun J, Lee HW, Pasta M, Yuan HT, Zheng GY, Sun YM, et al. A phosphorene-graphene hybrid material as a high-capacity anode for sodium-ion batteries. Nat Nanotechnol 2015;10:980–5.

[309] Hembrarn KPSS, Jung H, Yeo BC, Pai SJ, Kim S, Lee KR, et al. Unraveling the atomistic sodiation mechanism of black phosphorus for sodium ion batteries by first-principles calculations. J Phys Chem C 2015;119:15041–6.

[310] Kim H, Seo M, Park MH, Cho J. A critical size of silicon nano-anodes for lithium rechargeable batteries. Angew Chem Int Ed 2010;49:2146–9.

[311] Gauthier M, Mazouzi D, Reyter D, Lestriez B, Moreau P, Guyomard D, et al. A low-cost and high performance ball-milled Si-based negative electrode for high-energy Li-ion batteries. Energy Environ Sci 2013;6:2145.

[312] Qian J, Chen Y, Wu L, Cao Y, Ai X, Yang H. High capacity Na-storage and superior cyclability of nanocomposite Sb/C anode for Na-ion batteries. Chem Commun (Camb) 2012;48:7070–2.

[313] Jung SC, Choi JW, Han Y-K. Anisotropic volume expansion of crystalline silicon during electrochemical lithium insertion: an atomic level rationale. Nano Lett 2012;12:5342–7.

[314] Gu M, Li Y, Li X, Hu S, Zhang X, Xu W, et al. In situ TEM study of lithiation behavior of silicon nanoparticles attached to and embedded in a carbon matrix. ACS Nano 2012;6:8439–47.

[315] Wang B, Li X, Zhang X, Luo B, Zhang Y, Zhi L. Contact-engineered and void-involved silicon/carbon nanohybrids as lithium-ion-battery anodes. Adv Mater 2013;25:3560–5.

[316] Nie AM, Cheng YC, Ning SC, Foroozan T, Yasaei P, Li W, et al. Selective ionic transport pathways in phosphorene. Nano Lett 2016;16:2240–7.